KIT SCIENTIFIC REPORTS 7722

Annual Report 2015

Institute for Pulsed Power and Microwave Technology
Institut für Hochleistungsimpuls- und Mikrowellentechnik

John Jelonnek (ed.)

KIT Scientific Publishing

John Jelonnek (ed.)

Annual Report 2015

Institute for Pulsed Power and Microwave Technology
Institut für Hochleistungsimpuls- und Mikrowellentechnik

Karlsruhe Institute of Technology
KIT SCIENTIFIC REPORTS 7722

Annual Report 2015

Institute for Pulsed Power and Microwave Technology
Institut für Hochleistungsimpuls- und Mikrowellentechnik

edited by
John Jelonnek

KIT Scientific Publishing

Report-Nr. KIT-SR 7722

Part of this work was supported by ITER Organization under the service contract No. ITER/CT/12/4300000720. The views and opinions expressed herein reflect only the author's views. The ITER Organization is not liable for any use that may be made of the information contained therein.

Part of this work, supported by the European Communities under the contract of association between KIT, was carried out within the framework of the European Fusion Development Agreement. Part of this work is supported under Task WP13-IPH-A07-P1-01/KIT/PS, Task WP13-IPH-A11-P1-01/KIT/PS and Task WP13-PEX-P01+02+03b/KIT/PS.

Part of this work has been carried out within the framework of the EUROfusion Consortium and has received funding from the Euratom research and training programme 2014-2018 under grant agreement No 633053. The views and opinions expressed herein do not necessarily reflect those of the European Commission. Parts of the simulations presented in this work have been carried out using the HELIOS supercomputer at IFERC-CSC.

Part of this work is supported by Fusion for Energy (F4E) under Grants F4E-GRT-553, OPE-458 and within the European GYrotron Consortium (EGYC). EGYC is a collaboration among CRPP, Switzerland; KIT, Germany; HELLAS, Greece; IFP-CNR, Italy. The views expressed in this publication do not necessarily reflect the views of the European Commission.

Impressum

KIT Scientific Publishing

Karlsruher Institut für Technologie (KIT)
KIT Scientific Publishing
Straße am Forum 2
D-76131 Karlsruhe

KIT Scientific Publishing is a registered trademark of Karlsruhe Institute of Technology. Reprint using the book cover is not allowed.

www.ksp.kit.edu

This document – excluding the cover, pictures and graphs – is licensed under the Creative Commons Attribution-Share Alike 3.0 DE License (CC BY-SA 3.0 DE): http://creativecommons.org/licenses/by-sa/3.0/de/

The cover page is licensed under the Creative Commons Attribution-No Derivatives 3.0 DE License (CC BY-ND 3.0 DE): http://creativecommons.org/licenses/by-nd/3.0/de/

Print on Demand 2017

ISSN 1869-9669
DOI: 10.5445/KSP/1000060174

Institute for Pulsed Power and Microwave Technology

Institut für Hochleistungsimpuls- und Mikrowellentechnik (IHM)

Director: Prof. Dr.-Ing. John Jelonnek

The Institute for Pulsed Power and Microwave Technology (Institut für Hochleistungsimpuls- und Mikrowellentechnik (IHM)) is doing research in the areas of pulsed power and high power microwave technologies. Both, research and development of high power sources as well as related applications are in the focus. Applications for pulsed power technologies are ranging from material processing to bioelectrics. High power microwave technologies are focusing on RF sources (gyrotrons) for electron cyclotron resonance heating of magnetically confined plasmas and on applications for material processing at microwave frequencies.

The IHM is doing research, development, academic education, and, in collaboration with the KIT Division IMA and industrial partners, the technology transfer. The IHM is focusing on the long term research goals of the German Helmholtz Association (HGF). During POF3, the ongoing program oriented research period of HGF (2015 – 2020), research projects are running within following four HGF programs: “Energy Efficiency, Materials and Resources (EMR)”; “Nuclear Fusion (FUSION)”, “Nuclear Waste Management, Safety and Radiation Research (NUSAFE)” and “Renewable Energies (EE)”.

During 2015, R&D work has been done in the following areas: fundamental theoretical and experimental research on the generation of intense electron beams, strong electromagnetic fields and their interaction with biomass, materials and plasmas; application of those methods in the areas of energy production through controlled thermonuclear fusion in magnetically confined plasmas, in material processing and in energy technology.

Mentioned research areas require additionally the profound knowledge on modern electron beam optics, high power micro- and millimeter waves, sub-THz technologies, vacuum electronics, material technologies, high voltage technologies and high voltage measurement techniques.

Department for Pulsed Power Technologies:

(Head: Prof. Dr.-Ing. Georg Müller)

In environmental- and bio-technology the research and development is devoted to pulsed power technology with repetition rates up to 20 Hz, power in the Giga-Watt range and electric field strengths of 105-107 V/m. The research is concerned with short pulse (µs) - and with ultra-short pulse (ns) treatment of biological cells (electroporation). The focus is related to large-scale applications, treatment of large volumes, to the realization of a high component life time and to the overall process integration. Main directions of the work are the electroporation of biological cells for extraction of cell contents (KEA process), the dewatering and drying of green biomass, the treatment of micro algae for further energetic use and sustainable reduction of bacteria in contaminated effluents. Another key research topic is related to the surface modification and corrosion protection of metals and alloys using high-energy, large-area pulsed electron beams (GESA process). The research is focused on electron beam physics, the interaction of electron beams with material surfaces and the corresponding investigations on material specific characterization. The goal is to develop a corrosion barrier for improved compatibility of structural materials in contact with liquid metal coolants (Na, Sn, Pb or PbBi). (Programs: EE, NUSAFE).

The 2015 focus was laid on application-oriented R&D for high mass-flow PEF-treatment of microalgae. It could be shown, that PEF treatment with long pulses (≥50 µs) can result in precipitation of biomass on cross linear treatment chambers' anodes. Biomass precipitation is considerably lower if pulses of 10 µs and shorter are applied. ROS-signaling was identified to play an important role in nanosecond PEF-induced stress responses in plant cells. Patch-clamp measurements provided new insights in membrane permeabilization mechanisms. A memory effect could be observed by membrane conductance measurements during the application of pulse trains. The permeabilization of the cell membranes by application of pulsed electric fields (PEF) to biological tissue can be used as an alternative way for food preparation instead of thermal treatment. For this application a semiconductor-based pulse generator is currently being developed. The pulse generator consists of modules comprising IGBT switches, pulse capacitors,and control circuitry.

Within the joint IASS-KIT project on oxygen free methane reforming material concepts for the use of liquid tin at high temperatures were developed. Long-term corrosion tests were performed with different materials. The most promising material for the high temperature parts in tin is graphite and for temperatures up to 550° C Molybdenum (Mo) can be considered. Based on the results of the material tests a proposal for a possible reactor design was made. The gas inlet part requires lower temperatures to avoid an early cracking of methane, which can result in a blocking of the gas inlet; parts made of Mo can be employed. For the hot part an inner tube of graphite is proposed. To protect the graphite tube from an oxidizing atmosphere at high temperature an outer tube of an e. g. alumina forming alloy like FeCrAl will be considered.

The most promising liquid metal to be employed as heat transfer media in CSP tower receivers is liquid Natrium (Na). Compared to experiments performed with Pb alloys and Sn in the past, sodium requires significant improved safety measures that assure to avoid any contact of Na at high temperatures with water and air. Therefore, a new Na-Corrosion lab containing a COSTA-SOL for corrosion tests in stagnant Na at temperatures up to 880°C and a high temperature thermal cycling loop SOLTEC-TCT (700°C + 880°C) was established.

In the field of transmutation of long-living high-level radioactive waste from existing nuclear power reactors the institute's contribution is the development of a suitable corrosion protection especially for parts under

high loads like fuel claddings or pump materials in contact with liquid Pb or PbBi. Pulsed large area electron beams (GESA) are used to modify the surface of steels such that they fulfil the requirements of their surrounding environment. Conditioning the liquid metals with regard to its oxygen concentration and the transport of oxygen are further tasks. All tasks are embedded in European and international projects like e.g. MATTER, SEARCH, ESNIIplus and MaTISSE.

Department for High Power Microwave Technologies:

(Head: Dr. Gerd Gantenbein)

The Department for High Power Microwavea Technologies is focusing on the research and development of high power RF sources (gyrotrons) and related components for electron cyclotron resonance heating and current drive (ECRH&CD) of magnetically confined nuclear fusion plasmas. Additionally, it is doint research and development in the field of and on the application of microwaves to chemical processes, materials and composites.

- Collaboration within the W7-X project PMW for planning, construction and testing of the 10 MW CW, 140 GHz electron cyclotron resonance heating (ECRH) system for the stellarator W7-X at IPP Greifswald. In particular, the 1 MW CW, 140 GHz gyrotrons have been developed in cooperation with EPFL-CRPP Lausanne and Thales Electron Devices (TED), Vélizy, France. In 2015, the last gyrotron of the initial installation has been delivered to KIT for FAT test. The final SAT and FAT tests are expected at IPP Greifswald for 2016. Start of operation and first plasma in the Wendelstein 7-X fusion research device at IPP Greifswald has been at December 10, 2015.
- Within the European GYrotron Consortium (EGYC) and in collaboration with its industrial partner Thales Electron Devices (TED), Vélizy, France, EGYC is developing gyrotrons for the International Thermonuclear Experimental Reactor (ITER). According to a change in the delivery strategy for ITER, Europe will provide a total of 6 MW CW RF power at 170 GHz for the 24 MW CW ECRH system. Fusion for Energy (F4E) is coordinating the project. Institutional partners are CNR, Italy, EPFL-CRPP, Switzerland and HELLAS, Greece. In 2015, the testing of the 1 MW 170 GHz short-pulse gyrotron has been completed. This gyrotron has fulfilled all required key performance parameters. Additionally, the first CW prototype has been delivered to KIT during 4^{th} quarter of 2015. Tests are expected for 2016.
- KIT is pushing forward the development of multi-MW (2 MW) coaxial-cavity gyrotrons in frame of EUROfusion and as prerequisite for future DEMO gyrotrons. In 2015, the tube has been upgraded, extensive design work has been performed, aiming at long pulse operation of the existing coaxial gyrotron by introducing advanced cooling systems to the components.
- In frame of EUROfusion, KIT has continued its investigations on advanced gyrotrons for future DEMO. Target is the design of an 240 GHz gyrotron with frequency step-tunability and the possibility for operation at 170 GHz and 204 GHz additionally. In 2015 the design of coaxial cavity gyrotron and, alternatively, a conventional cavity gyrotron has been progressed. Studies on multi-staged depressed collectors which have the potential of significantly increasing the gyrotron efficiency have been continued.
- In the frame of studies of advanced technologies for future high-power gyrotrons a methodology has been progressed to determine the emitter emission homogeneity from the measurement of the current voltage characteristics of a magnetron injection gun. Within this work the influence of trapped electrons and low frequency oscillations on the operation of a gyrotron has been studied.

- KIT is in collaboration with EPFL-CRPP, Lausanne, to design a new (126 GHz / 84 GHz) dual-frequency 1 MW gyrotron based on design of ITER for TCV tokamak. In 2015, interaction calculations for the design of the cavity have beeen performed and simulations and design of a triode MIG have been completed.
- The erection of the new gyrotron test facility, FULGOR, with up to 10 MW electrical power has been progressed. The final design of the high voltage power supply has been agreed with the manufacturer and substantial progress has been achieved in the planning of several auxiliary systems for plant operation.
- An in-situ measurement setup for dielectric and calorimetric characterization of materials close to 2.45 GHz has been developed based on a dual-mode cavity. This system offers the possibility to optimize microwave heating in materials processing.
- In 2015 investigation of limits and accuracy of the cavity perturbation method for dielectric measurements have been performed and applied for different low loss and very high loss materials.
- Progress has been made in design studies for microwave filters which could decrease the microwave leakage and improve the overall efficiency of the Hephaistos oven.
- Within the FLAME project the application of microwave heating for curing carbon fiber reinforced composites has been investigated with industrial and institutional partners.
- Multiphysics simulations of the process of microwave assisted bonding of synthetic leather to a plastic substrate were performed in the frame of the ZIM project “Development of selective microwave assisted gluing of textile leather to plastic base plates”
- Within the H2020-SPIRE-2015 program the project SYMBIOPTIMA started in September 2015. The aim of this project is to improve European process industry efficiency by developing a cross-sectorial energy & resource management platform for intra- and inter-cluster streams in a symbiotic industrial cluster.
- In the context of biomass conversion to fuel, theoretical and practical feasibility studies were performed in 2015 for the application of microwave technology in this field.

Table of Contents

1. HGF Program: FUSION

1.1 Microwave Heating System for W7-X (PMW)

1.1.1 Introduction

Electron cyclotron resonance heating (ECRH) and current drive (ECCD) are the standard methods for localized heating and current drive in future fusion experiments the only CW heating methods available locate. Thus, ECRH will be the basic day-one heating system for the stellarator W7-X which started operation end of 2015 at IPP Greifswald. It is expected that the ECRH system for W7-X will be finalized in 2016. In its first stage W7-X will be equipped with a 10 MW ECRH system operating at 140 GHz in continuous wave (CW).

The complete ECRH system is coordinated by the project "Projekt Mikrowellenheizung für W7-X (PMW)". PMW has been established by KIT together with IPP and several EU partners in 1998. The responsibility of PMW covers the design, development, construction, installation and system tests of all components required for stationary plasma heating on site at IPP Greifswald. PMW coordinates the contribution from Institute of Interfacial Process Engineering and Plasma Technology (IGVP) of the University of Stuttgart too. IGVP is responsible for the microwave transmission system and part of the power supply (HV-system). IPP Greifswald is responsible for the in-vessel components and for the in-house auxiliary systems. PMW benefits from the collaboration with Swiss Plasma Center (SPC, former Centre de Recherche de Physique des Plasmas, CRPP) Lausanne, Commissariat à l´Energie Atomique (CEA), Cadarache and Thales Electron Devices (TED), Vélizy. A contract between CRPP Lausanne, FZK Karlsruhe and TED, Vélizy, had been settled to develop and build the series gyrotrons. First step in this collaboration was the development of a prototype gyrotron with an output power of 1 MW CW at 140 GHz.

Seven series gyrotrons have been ordered from the industrial partner Thales Electron Devices (TED), Vélizy. First operation and long pulse conditioning of these gyrotrons is being performed at the teststand at KIT. Pulses up to 180 s duration at full power are possible (factory acceptance test, FAT) whereas 30 minutes shots at full power are possible at IPP (necessary for site acceptance test, SAT). Including the pre-prototype tube, the prototype tube and the 140 GHz CPI tube, in total 10 gyrotrons will be available for W7-X in the final state. To operate these gyrotrons, in addition to the Oxford Instruments and Accel magnets, eight superconducting magnet systems have been manufactured at Cryomagnetics Inc., Oak Ridge, USA.

Most of the components of the transmission system, HV-systems and in-vessel-components have been ordered, manufactured, delivered, tested and are ready for operation at IPP Greifswald. A part of the existing ECRH system has been already used to test new concepts and components for ECRH. A significant delay arose in the project due to unexpected difficulties in the production of the series gyrotrons.

1.1.2 Series Gyrotrons for W7-X

In 2005, the first TED series gyrotron SN1 had been tested successfully at FZK and IPP (920 kW/1800 s). It met all specifications during the acceptance test, no specific limitations were observed. In order to keep the warranty SN1 has been sealed, one prototype gyrotron has been routinely used for experiments.

The series gyrotrons following SN1 did show a more or less different behavior with respect to parasitic oscillations excited in the beam tunnel region. These oscillations resulted in an excessive heating of the beam tunnel components, in particular of the absorbing ceramic rings. The gyrotrons re-opened after operation showed significant damages due to overheating at the ceramic rings and the brazing of the rings. A possible solution was proposed and successfully tested by KIT. As the main difference to the usual beam tunnel this design features corrugations in the copper rings which handicap the excitation of parasitic modes.

The thermal loading of the collector depends on the interaction efficiency between the electromagnetic field and the electron beam. And, of course, it depends on the pulse length. For high power operation at continuous wave (CW) the thermal loading is close to what is feasible in terms of cooling and lifetime of the collector. For the series tubes a patented sweeping procedure has been introduced which combines a vertical and radial displacement of the electron beam at the collector. This results in an almost constant power deposition at the inner wall along the axis and removes the particularly dangerous temperature peaks at the lower and upper reversal points of the electron beam.

Additional to the innovative collector sweeping, modifications have been realized and already tested in order to reduce the absorption of the internal stray radiation by covering stainless steel components with copper.

A possible corrosion in the water cooling circuit of the diamond window at the brazing structure is prevented by replacing the water by inert Silicon oil.

In 2015 the Site Acceptance Tests of the TED series gyrotron SN7i could be finished successfully. Stable operation of the tube at RF power of app. 900 kW has been shown and quasi steady state operation (1620 s) at full power has been demonstrated. The results obtained at KIT during Factory Acceptance Test (FAT) have been confirmed. Since early 2015 there are 7 Gyrotrons operable on site at IPP Greifswald.

The repair of the TED series gyrotron SN5i has been progressed in 2015. The manufacturer delivered the tube in October to KIT for FAT. The short pulse tests have been started immediately, the tube showed RF output power up to 900 kW, the measurement of the output beam showed a well centered beam at the window and fundamental Gauss content of 97 %. Unfortunately, conditioning of the tube and full power operation up to 180 s could not be finished at the KIT teststand due to a schedule conflict with other contractual obligations. In agreement with the involved parties it was decided to restart these tests in early 2016 at IPP Greifswald and to merge FAT and SAT.

A big milestone for the stellarator and the ECRH system has been achieved end of 2015. The first plasma at W7-X has been created in December 10th 2015 with electron cyclotron resonance heating (ECRH). It was the dignified completion of the project PMW, which had build-up the ECRH system at the IPP-Greifswald during the last 15 years. In the first experimental campaign in 2015 the ECRH system operated absolutely reliably from the first shot on and guarantied plasma start-up and heating of already more than 500 discharges without any failure, which clearly demonstrates the high quality of all contributions to the project PMW.

1.1.3 Transmission Line System for W7-X

The transmission of the gyrotron power to the plasma is performed via an optical system, which consists of single-beam and multi-beam waveguide (MBWG) elements, in total more than 150 reflectors. For each

gyrotron, a beam conditioning assembly of four mirrors is used to match the gyrotron output to a Gaussian beam with the correct beam parameters, and to set the appropriate polarization needed for optimum absorption in the plasma. A fifth mirror directs the beam to the beam combining optics, which is situated at the input plane of a multi-beam wave guide. This MBWG is designed to transmit up to seven beams (five 140 GHz beams, one 70 GHz beam, and one channel connected to the N-port remote-steering launchers via switches) from the gyrotron area (entrance plane) to the stellarator hall (exit plane). To transmit the power of all gyrotrons, two symmetrically arranged MBWGs are used. At the output planes of the MBWGs, two mirror arrays separate the beams again and distribute them via two other mirrors and CVD-diamond vacuum barrier windows to individually movable antennas (launchers) in the torus.

In 2015, the commissioning of the ECRH system is further advanced. The beam paths of the gyrotrons were aligned up to the vacuum windows at the torus. For the final adjustment of the MBWG mirrors, only two beams were necessary, demonstrating the nearly perfect imaging properties of the MBWG section. The overall power loss from the gyrotrons up to the torus windows is about 6 % including diffraction, beam truncation, misalignment, absorption of the mirrors and the atmosphere, in good agreement with the expected theoretical power loss. The loss of the MBWG itself was proven by reflecting the high power ECRH beam with the aid of a retroreflector at the end of the MBWG section. Therefore, the beam passes twice the MBWG to measure its remaining power in the same calorimeter as the input beam.

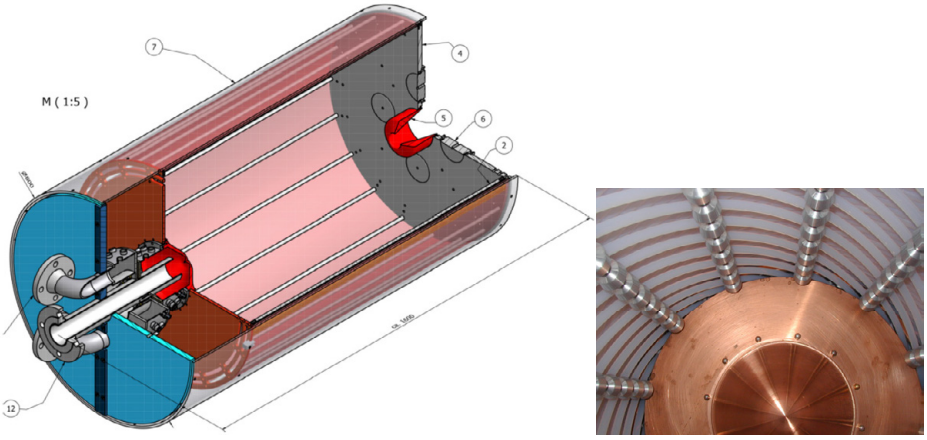

Fig. 1.1.1
Design drawing of the 2-MW absorber load (left) and Photograph of the inner surface of the prototype 1-MW load (right) showing (part of the) distribution reflector and the arrangement of the Teflon hoses.

The dummy loads presently available at W7-X employ chamber walls with low absorption and a high number of internal reflections to dump the power. Therefore, the field strenght in the loads is relatively high, which leads to a significant probability of arcing. For high reliability, loads based on an alternative concept – high absorption and only few internal reflections – are developed and built. These loads use a meshwork of water-filled Teflon hoses as absorber, where a highly turbulent flow suppresses the boiling of the water in the tubes. They feature a beam concentrator (modified Winston cone) at the beam input, and an optimized conical reflector to distribute the input beam power evenly on the walls of the load chamber (see Fig. 1.1.1 left as example). As prototype, a 1-MW, long-pulse load was designed and built; here, 24 Teflon hoses form the absorbing meshwork (Fig. 1.1.1 right). The load has been tested up to 880 kW and 3 min; no arcing was detected. It will be further used in the ECRH-3 system on ASDEX Upgrade. For W7-X, the design and construction of a 2 MW, CW load with 36 Teflon hoses connected in parallel (Fig. 1.1.1 left) was started.

Ongoing is beam characterisation and the subsequent design and manufacturing of the surfaces of the matching mirrors for newly delivered gyrotrons; in autumn 2015, the beam of the Thales tube SN5i was characterized. The design of the matching mirrors with the integrated 2-frequency power monitors is underway.

1.1.4 In-Vessel Components for W7-X

The ECRH antenna system in W7-X consists of four front steering launcher with up to three individually steerable beam lines in each launcher. The ERCH beam lines have been aligned up to the plasma vessel with the gyrotron beams. Even inside the plasma vessel the beam positions and directions were proved with absorbing targets and infrared pictures for different positions of the front steering mirrors. Thus the ECRH injection could be precisely controlled during first plasma operation. Each launcher is also equipped with an immersion tube with sapphire window and a video camera at its front. This video system is used to observe the graphite tiles at heat shield at the plasma vessel wall opposite to the launcher. In order to screen out the plasma radiation, the video cameras are equipped with a filter which cuts off the visible light below 900 nm. This near infrared observation was absolutely calibrated with a black body radiation source and allows to measure tile temperatures between 400° and 1100° c. In the heat shield tiles 128 waveguide antennas are incorporated. They give information of the beam absorption, polarization and position. In addition five ECRH stray radiation detectors, so called sniffer probes, have been installed in W7-X. They provide information about the integral absorption of all launched ECRH beams. Each ECRH module is equipped with one sniffer detector. These detectors could already be tested and calibrated in the empty plasma chamber and with short ECRH-pulses before plasma operation. The quality of the signal is shown in the Fig. Sniffer. Here the successful plasma generation (decay of stray radiation) can be seen. They are excellent indicators of high ECRH absorption and thus of the existence of a high temperature plasma. Therefore these signals are also used in the W7-X interlock system to prohibit ECRH operation without an absorbing plasma.

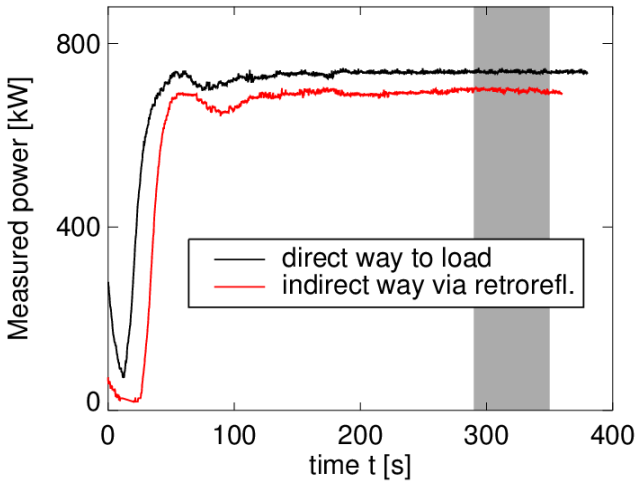

Fig. 1.1.2
MBWG: Comparison of the microwave power measured in the long pulse calorimetric load for the direct way to the load and the transmission with the MBWG line with 18 reflections more. The measurement was taken the end of 350 s of gyrotron operation to insure that the system has achieved stationary conditions. The difference is only 5.6 % +- 0.6.

The beam paths for EC heating scenarios with incomplete absorption (O2, X3) had been defined by IPP. Now, corrections of the beam paths due to refraction in the plasma are being calculated using TRAVIS. On this basis, the design of the holographic in-vessel reflectors, which direct the shine-through power back into the plasma via a controlled second path to improve the heating efficiency is ongoing, and the manufacturing of the reflector tiles has started.

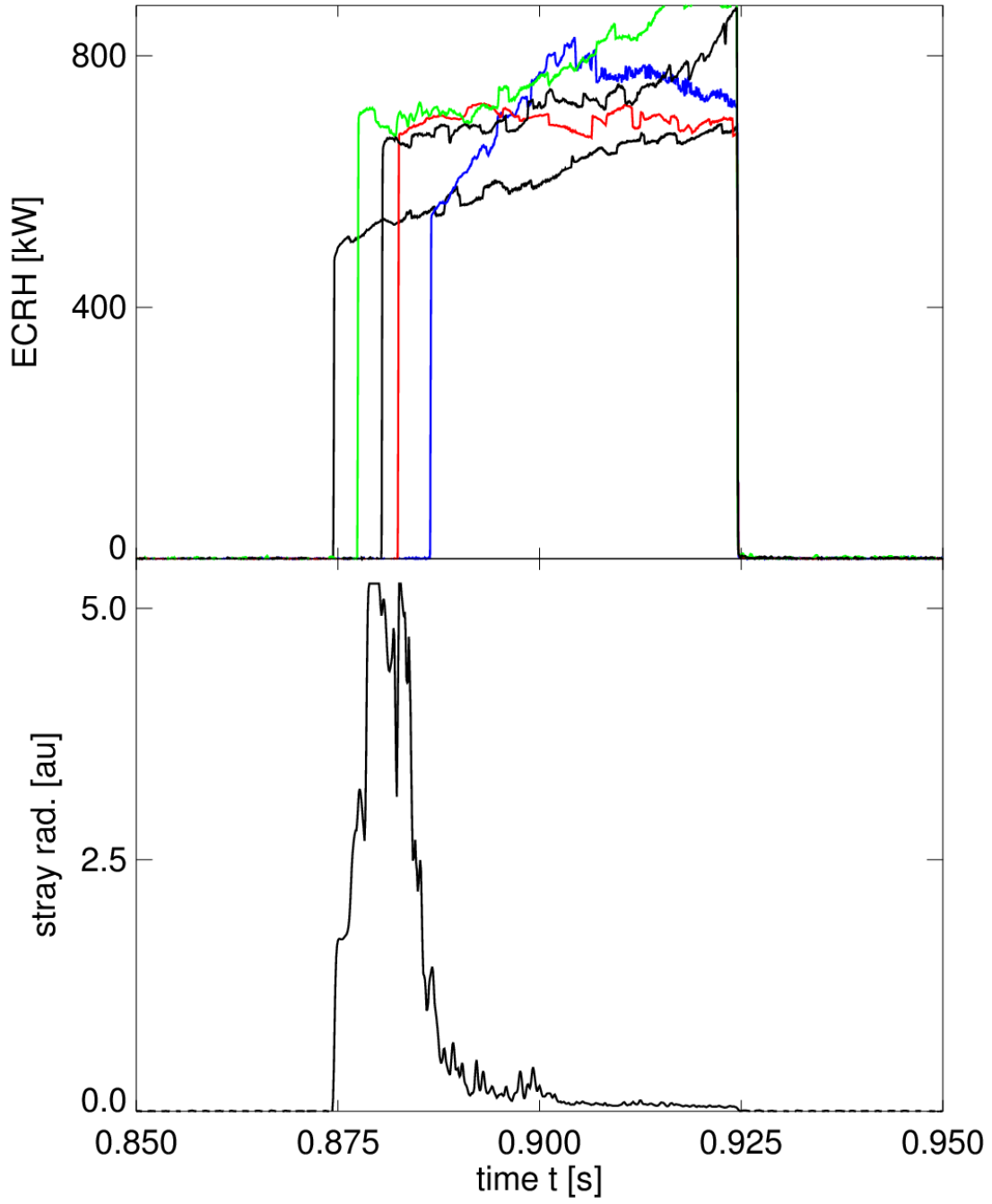

Fig. 1.1.3
Sniffer: Power signals of 5 gyrotrons (top) and one sniffer signal (bottom), measure of not absorbed ECRH-stray radiation, during a typical plasma start-up of the 3rd experimental day of W7-X . The exponential decay of the sniffer signal represents the plasma build-up with electron densities and temperatures which provide almost complete ECRH absorption in the later phase.

1.2 170 GHz, 1 MW CW Gyrotron Development for ITER

1.2.1 Introduction

The European 1 MW, 170 GHz, Continuous Wave gyrotron with cylindrical cavity for ITER has been designed within EGYC (European GYrotron Consortium) under the coordination of F4E. In the frame of the EU program for the development of the 1 MW gyrotron for ITER, a short-pulse (SP) version (Fig. 1.2.1) of the CW gyrotron has been designed and manufactured at KIT in collaboration with the industrial partner Thales Electron Devices (TED).

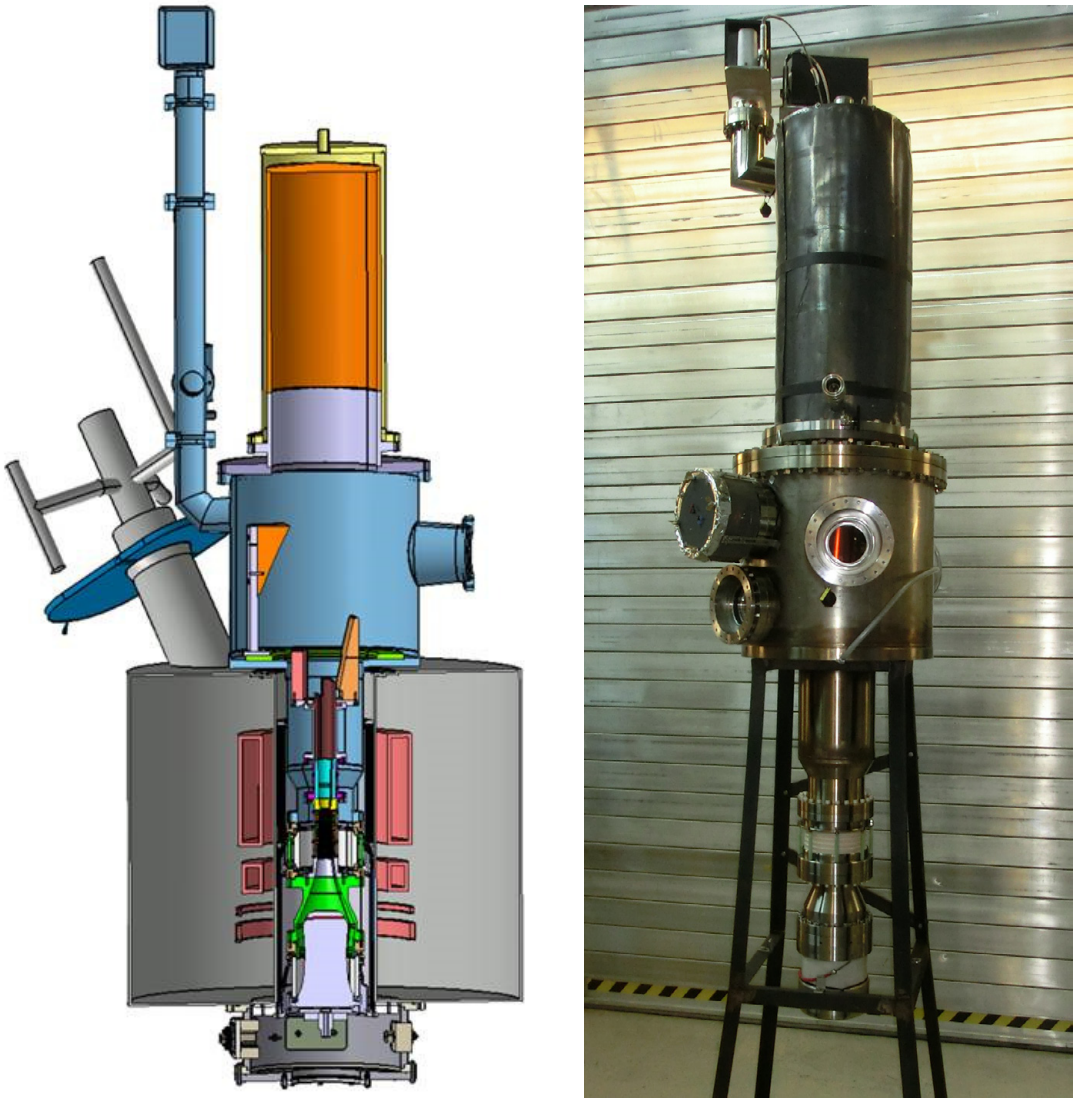

Fig. 1.2.1
EU 1 MW short-pulse gyrotron prototype for ITER.

Operating cavity mode	$TE_{32,9}$
Frequency (cold cavity), f	170 ± 0.3 GHz
RF output power, P_{out}	1 MW
Beam current, I_B	40 A
Cathode voltage, U_C	86 kV
Velocity ratio (pitch factor), α	~1.3
Cavity magnetic field, B_{cav}	6.78 T
Output efficiency with SDC	> 50 %

Table 1.2.1
Design parameters for the gyrotron.

The technological design of the tube is similar to the design of the 1 MW, 140 GHz, CW, Wendelstein W7-X gyrotron, developed and successfully tested at KIT. Firstly, the manufacturing of two gyrotron prototypes are planned (1) a modular short-pulse gyrotron intended to validate the design of the strategic gyrotron subcomponents in pulse length of a few millisecond (<10 ms) and (2) a CW industrial prototype to reach the ITER requirements in terms of output power, efficiency, pulse length and RF beam quality (delivery is scheduled to the last quarter of 2015). The initial RF tests of both prototypes will be performed with the existing Oxford Instrument (OI) super-conducting magnet (SCM) at KIT. Due to high voltage power supply limitations the pulse length is limited to 3 min. The design specifications including the nominal operating parameters are summarized in Table 1.2.1.

The fabrication of the components of the SP prototype has been completed in August 2014 and preliminary experiments were performed with the adapted electron gun of the coaxial-cavity gyrotron, available at KIT. Although this electron gun was not optimized for operation with the new 1 MW gyrotron prototype, very promising results have been obtained, allowing the validation of some critical gyrotron components in advance. The tube has delivered an RF power above 1 MW with a reasonable value of the output efficiency around of 30 % (equivalent interaction efficiency ~35 %) at correct mode and frequency, in operation without depressed collector. In the calculation of the interaction efficiency, a total of 10% losses, due to stray radiation and to voltage depression in the cavity in a non-neutralized case, have been taken into account. In addition, the efficiency of the mode converter has been verified – the fundamental Gaussian mode content of the RF output beam was estimated to be at least 96 %.

1.2.2 Experimental Results with the 170 GHz, 1 MW short pulse prototype tube (F4E-GRT-553)

The experiments with the nominal electron gun have started in November 2014. After conditioning and optimization of the operating parameters a stable gyrotron operation has been achieved. Apart from the nominal high-voltage (~86 kV) operating parameters (HVOP, mentioned in Table 1.2.1) an operation of the gyrotron has been investigated also at a lower voltage operating point (LVOP, ~78 kV). At both operating

points an RF output power above 1 MW with output efficiency of around 30 % (interaction efficiency ~35 %) has been demonstrated (Fig. 1.2.2), being in a very good agreement with calculations. The gyrotron was operated at pulse lengths up to 10 ms. The nominal mode has been excited at the frequency 170.1 GHz which is in agreement with the ITER specification. Furthermore, in order to prove the capability of the tested gyrotron in terms of achievable RF output power, the beam current has been increased up to around 63 A. At that operating point, at ~74 kV (LVOP) an RF output power around 1.5 MW at an output efficiency around ~30 % (interaction efficiency ~35 %) has been obtained. In addition, the performance of the quasi-optical (q.o.) mode converter, based on a mirror-line launcher and three mirrors with nearly quadratic surface contour function, has been validated. Precise beam profile measurements with an IR camera system and careful analysis of the RF output beam pattern showed a very good Gaussian mode content of about ~98 %. The total level of internal stray radiation is in the range of ~3 % of the RF output power. An example of the measured (using IR camera) RF beam profile close to the window position is presented in Fig. 1.2.3.

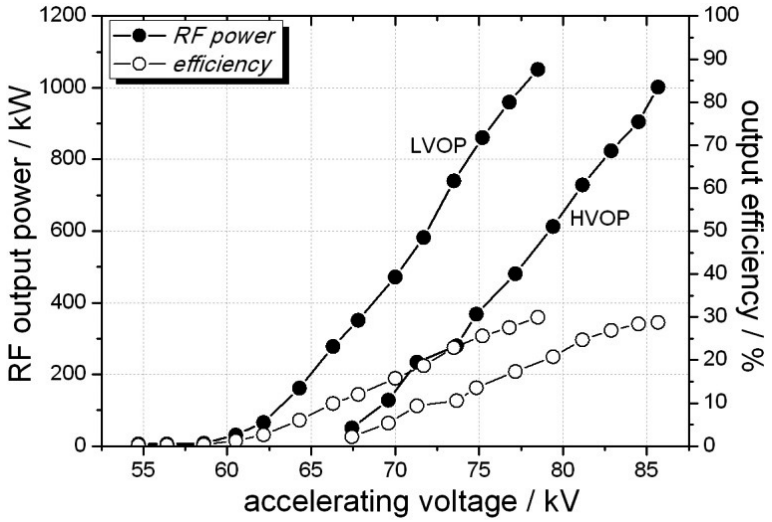

Fig. 1.2.2
RF output power and output efficiency as a function of accelerating voltage measured at both: low-voltage (LVOP: ~78 kV and Ib~45 A) and high-voltage (HVOP: ~86 kV and Ib~40 A) operating points without depressed collector.

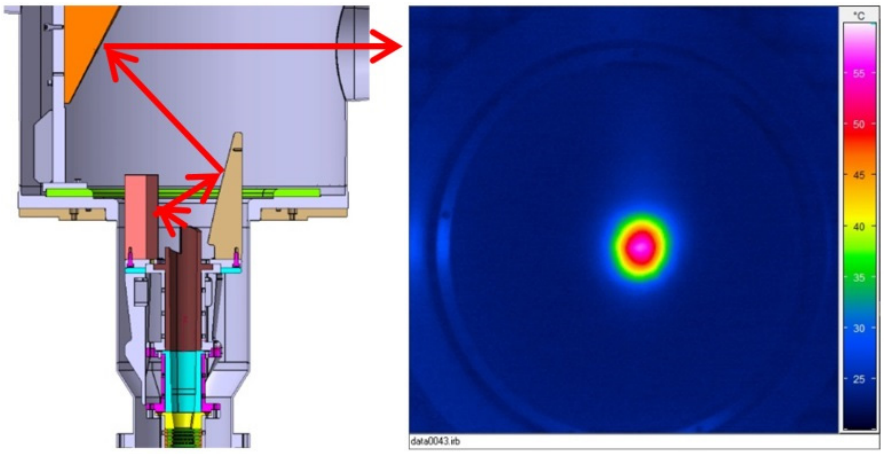

Fig. 1.2.3
Arrangement of the q.o. mode converter (left) and RF beam profile close to the gyrotron output window measured using the IR camera (right).

Furthermore, first experiments with the single-stage depressed collector (SDC) have been performed. Fig. 1.2.4 presents the achieved RF power and efficiency in dependence of the depression voltage. The output power and the overall efficiency are decreasing at a depression voltage slightly above 26 kV (nominal value: 35 kV). This observed decrease of output power and efficiency was expected theoretically and is related to the drop of the electrons kinetic energy and in consequence to the reflection of electrons in the region of the mirror box. A drop of the electron kinetic energy is caused in the microwave box region due to a voltage depression of the spent beam space-charge. The voltage depression in that region results in a reduction of the applicable maximum depression voltage before reflection of electrons begins. That effect is mainly due to the geometrical arrangement of the short pulse gyrotron inside the mirror box which is quite different from the CW prototype, in which an additional cooling system (at depression voltage) in the mirror box region is installed. It has been numerically shown that the additional metallic structures in that critical region will reduce the voltage depression and thus should improve the overall efficiency in CW prototype. In order to validate the numerical results using the short-pulse prototype some simple metallic pipes (put on depressed potential) are going to be installed in the mirror box region in order to emulate the cooling system of CW prototype. The structure has been already designed and installed in the gyrotron. In addition the SP gyrotron prototype has been equipped with the isolated collector. By placing of the gyrotron body on the deaccelerating voltage, the depression gap which leads to the electron reflections in the collector region would be minimized. The experimental tests with the modified gyrotron setup are planned in 2016.

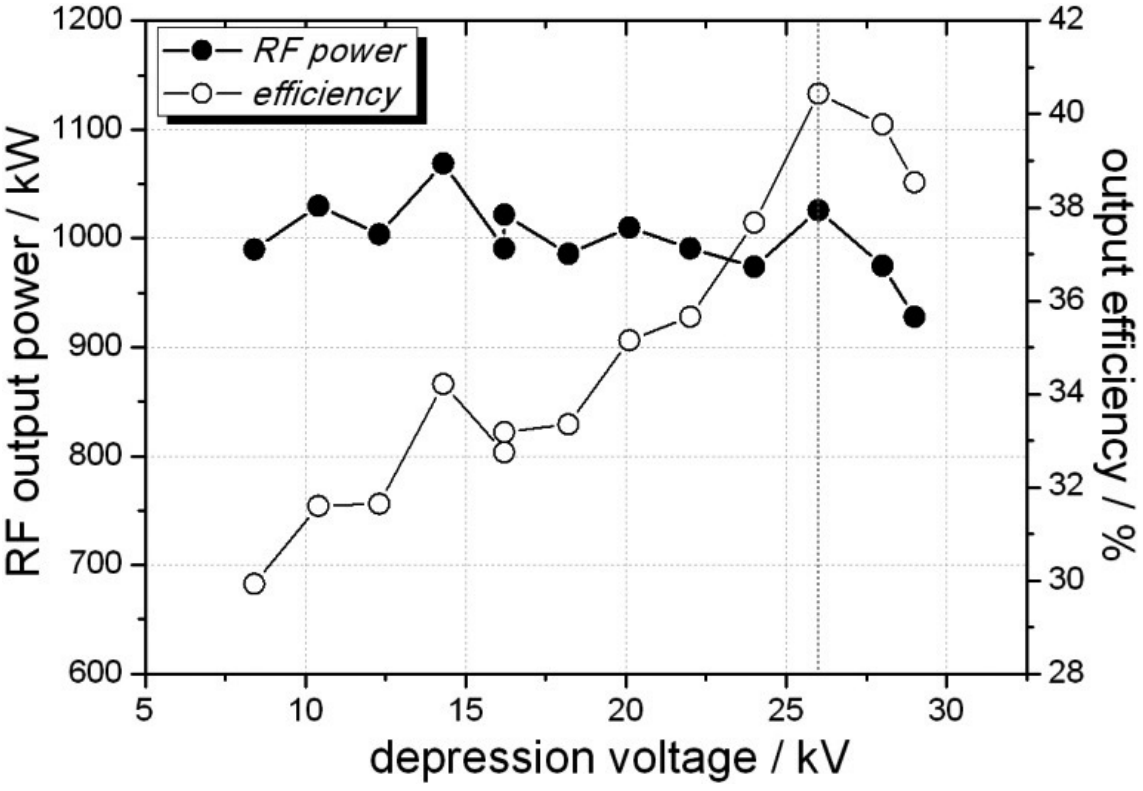

Fig. 1.2.4
RF output power and output efficiency as a function of depression voltage obtained at high-voltage (HVOP: ~86 kV and Ib~43 A) with a single-stage depressed collector (SDC).

1.2.3 Validation of the 1 MW, 170 GHz industrial CW prototype gyrotron for ITER (F4E-GRT-553)

The manufacturing of a first industrial continuous-wave (CW) prototype gyrotron, based on the design of the SP gyrotron, has been completed in November 2015. The tube has been delivered to KIT and recently installed into the superconducting gyrotron magnet. The start of the tests is scheduled for February 2016. At first, in order to optimize the gyrotron operating point in terms of stability and efficiency of the RF power generation, the tube will be operated in the short-pulse regime. Furthermore, detailed investigations of the mode converter efficiency, by measuring of the fundamental Gaussian mode content and stray radiation level, will be performed as well. The next phase will consist in pulse length extension and optimisation of the associated operating point. The first experimental results are end of February.

1.2.4 Beam-wave interaction modelling (F4E GRT-553)

The performed work focused on two areas: (i) theoretical studies and EURIDICE upgrades towards improved interaction modeling, and (ii) highly realistic multi-mode interaction simulations for the 170 GHz, 1 MW EU gyrotron for ITER. Within the first area, the concept of introducing varying reference frequencies in the interaction model has been consolidated, an alternative simplified model for simulating dynamic after-cavity interaction (based on two, rather than one, carrier frequencies for the operating mode) has been tested, and, finally, an upgrade of the implementation of the calculation of electron velocity and energy spreads in EURIDICE resulted in an increase of speed, exceeding a factor of 2 in several cases. In the area of simulations of the ITER gyrotron, highly realistic simulations of experimental operating points of the short-pulse modular prototype have been continued, and a dedicated study on the effect of the thermal deformation of the interaction cavity on gyrotron performance has been undertaken. The thermal deformation is expected to be important during long-pulse operation of the industrial CW prototype. For this study, EURIDICE was upgraded to address the influence of the axial distribution of temperature on the wall conductivity, and an iterative process, taking also into account results by thermomechanical simulation codes existing in TED and F4E, was launched. As can be seen in Fig. 1.2.5 (a), the iterative process for the nominal operating point converges in a bell-shaped deformation of the cavity. This would result in ~380 MHz drop in frequency, as well as in ~13 % reduction in power as a consequence of the decrease in the quality factor Q_{dif} of the operating $TE_{32,9}$ mode. This is apparent in the multi-mode, start-up simulations of Fig. 1.2.5 (b), where the cavity deformation is considered after t = 4000 ns. Alternative operating points to mitigate this effect have been identified and are currently under validation.

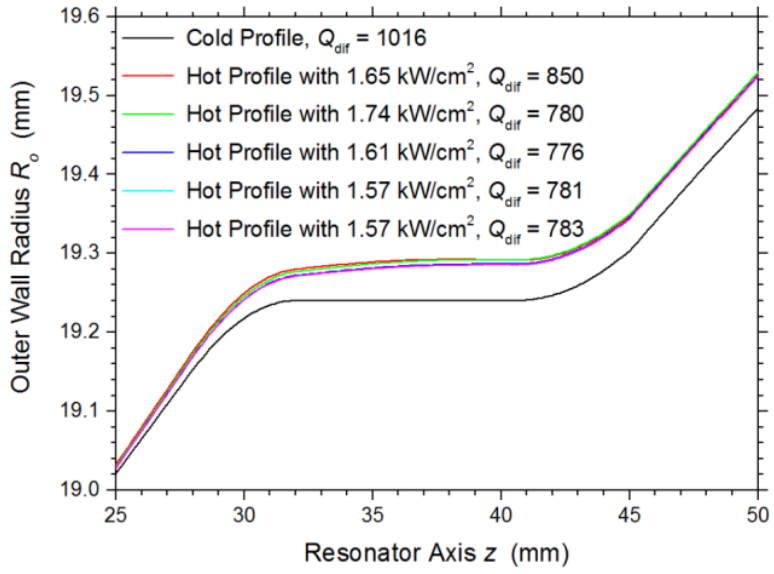

(a)

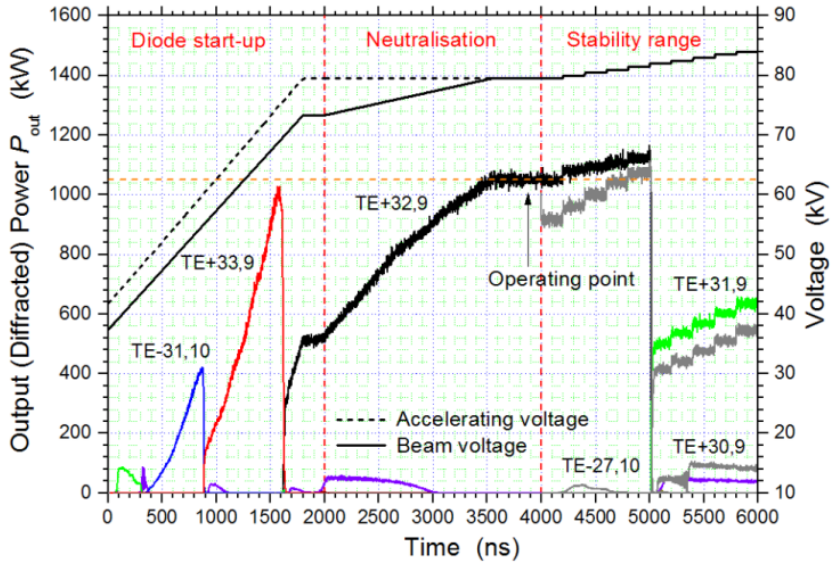

(b)

Fig. 1.2.5
(a) Iterative process considering the ohmic wall loading (kW/cm^2), as calculated by EURIDICE, and the thermally deformed cavity profile, as calculated by thermomechanical codes. (b) Multi-mode interaction simulations at the nominal operating point (79.5 kV, 40 A). After start-up and beam neutralization (t > 4000 ns), the cavity deformation is considered (grey curves). The result can be compared to the case where the cavity would remain non-deformed (black/green curves).

1.2.5 Quasi-optical mode converter and Matching Optical Unit for EU ITER gyrotron (F4E-GRT-553)

A quasi-optical mode converter developed for the EU ITER gyrotron consists of a mirror-line launcher and three quasi-quadratic mirrors. In the short pulse tube, the mirrors are well aligned. However, due to the influence of cooling system in the CW tube, it is found that there are some misalignments in the 1st and 2nd mirrors. In order to compensate the misalignments, the 3rd should be rotated to correct the propagation direction and the position of the RF beam. The field distribution in the corrected mirror system has been

analyzed, and the simulation result shows that the deviation of the beam center is about 4.5 mm from the center of output window. The impact of tolerances of the quasi-optical system has also been investigated, where the possible uncertainty in the fabrication of the launcher and the misalignments of all three mirrors have been taken into account.

The sensitivity of the Matching Optical Unit (MOU) designed for the EU ITER gyrotron has been investigated. Two beam-shaping steerable mirrors are used in the MOU. The conversion efficiency of the RE beam to the HE_{11} mode is calculated to be 96.83 % without any misalignment. The effects of misalignment of the output beam from the gyrotron have been analyzed, based on data available from W7-X series production. For all ten possible misalignments, the conversion efficiencies could be still higher than 95 % by moving and rotating the steerable mirrors in the MOU. The field distribution of wave beam is shown in Fig. 1.2.6, where the conversion efficiency is decreased to 95 % due to the misalignment.

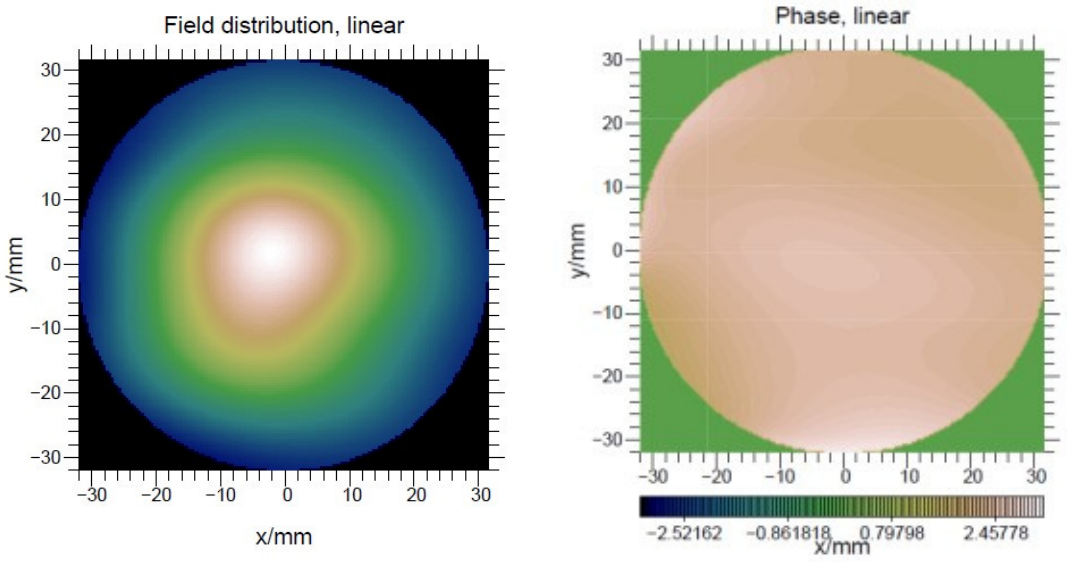

Fig. 1.2.6
Field distribution at the output of MOU.

A computer code for the vector analysis of fields in launchers is under development at KIT. A subroutine for the generation of curved triangle meshes, required for calculations with higher order basis functions, has been developed. The generated meshes can match launcher walls with perturbations and cuts. Furthermore the basic calculations to solve the electric-field integral equation have been carried out and implemented.

A hybrid-type launcher operating in the $TE_{32,9}$ mode at 170 GHz has been designed. However, calculation results show that the peak Ohmic loading on the launcher wall is as high as 765 W/cm^2, and according to the technical requirement a peak ohmic wall loading of ~500 W/cm^2 is allowed. The method for the synthesis of hybrid-type launchers has been improved. In terms of the improved method, the peak Ohmic loading on the wall of launcher operating in the $TE_{32,9}$ mode at 170 GHz has been depressed to 510 W/cm^2, and the Gaussian mode content is 99.12 % at the launcher aperture (see Fig. 1.2.7).

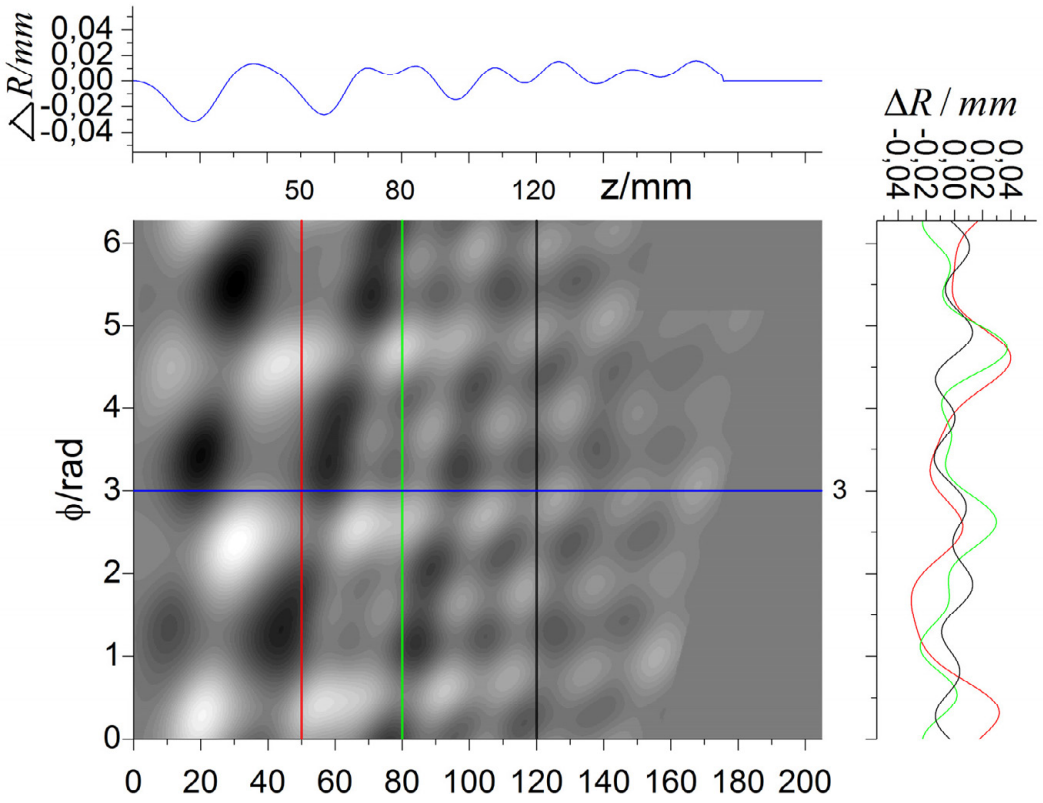

(a)

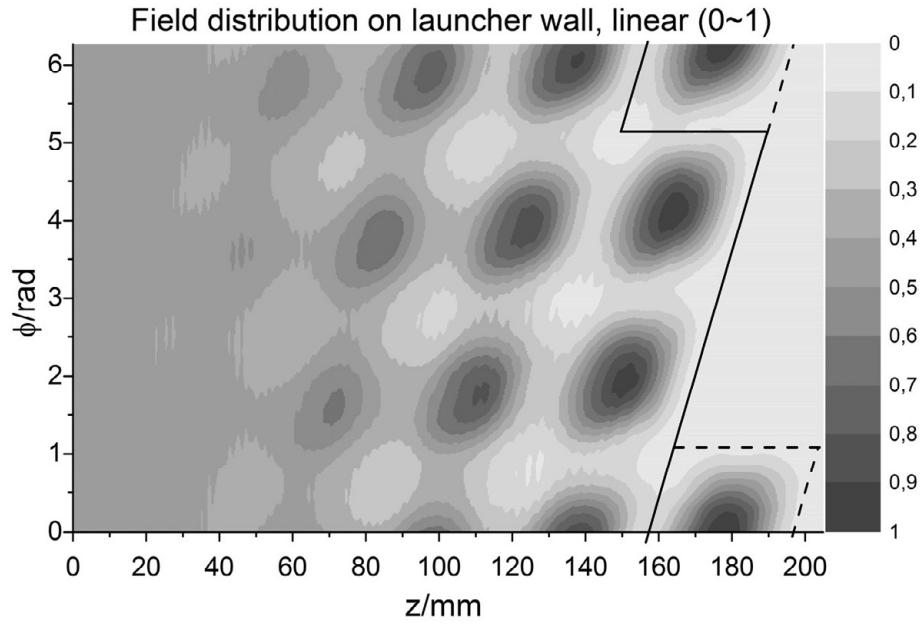

(b)

Fig. 1.2.7
Improved hybrid-type launcher operating in the $TE_{32,9}$ mode @ 170GHz, wall profile (a) and field distribution on launcher wall (b).

1.3 170 GHz, 2 MW coaxial cavity Gyrotron Development for ITER

1.3.1 Introduction

The development of a modular short-pulse pre-prototype as a basis for a 2 MW, 170 GHz, CW coaxial-cavity gyrotron is in progress. The current modular pre-prototype configuration allows the generation of >2 MW RF output power in short-pulses with a reasonable electronic efficiency of approximately 30 % without depressed collector operation. In the experiments an RF output power of 2 MW with an efficiency of 28 % (without SDC) has been successfully achieved at pulse lengths in the order of 1-1.5 ms at the beam current of 75 A. Furthermore, the gyrotron was operated with single stage depressed collector (SDC). In that configuration the output of 1.9 MW with the overall efficiency of the close to ~48 % has been demonstrated. The next goal of the development of the coaxial cavity gyrotron at KIT is preparation of the gyrotron setup for operation at longer pulses. In the frame of these activities, and as a very first step, a new cavity made of Glidcop has been constructed, which allows increasing the pulse length up to 40 ms without active cooling. The new cavity has been fabricated, installed in the existing modular gyrotron setup and finally successfully verified experimentally at the short pulse operation (~1 ms) first. In addition the design and development of a new gyrotron experimental setup suitable for the tube operation with longer pulse length has been started. In order to increase the gyrotron pulse length all subcomponents such as cavity, launcher, beam tunnel, mirrors and the collector have to be equipped by active cooling system. The preliminary achievements will be presented below.

1.3.2 Gyrotron cavity – Improved mechanical design and experimental verification

Thermomechanical issues: The theoretical design of the cavity of the 2 MW coaxial gyrotron has been completely validated in the last years during the regular experiments with the gyrotron prototype where a stable operation with the correct $TE_{34,19}$ mode up to 2 MW with reasonable gyrotron efficiency has been demonstrated [4]. After that, the main goal was to find a way to increase the pulse length of the gyrotron operation avoiding any modifications on the current gyrotron setup that would be necessary for an implementation of active cooling systems. The cavity is one of the most critical components which strongly limits the pulse length of the gyrotron operation. During the RF power generation inside the gyrotron the power loading at the cavity wall can easily reach the physical limits due to thermomechanical issues. Assuming the ideal conditions of the RF power generation inside the cavity, these physical limitations are governed mainly by the material properties of the cavity and the efficiency of implemented active cooling. Unfortunately, in the case of the existing modular short-pulse gyrotron prototype, due to the mechanical and constructional restrictions, no active cooling of the cavity can be implemented into the existing gyrotron setup. Therefore, at first, an improvement of the thermomechanical properties of the cavity using a more durable material (Glidcop instead of copper) was proposed. Glidcop refers to the family of copper based matrix composite alloys mixed primarily with aluminium oxide ceramic particles. The Glidcop material is characterized by higher thermomechanical properties than usually used oxygen-free copper, keeping the electrical and thermal conductivity close to the copper. The results of thermomechanical calculations showed that the Glidcop cavity is able to operate up to 40 ms (at nominal 2 MW of RF generated power inside the cavity) without implementation of an active cooling. The new improved version of the cavity has been manufactured (the final CAD design is shown in Fig. 1.3.1). In order to keep the mechanical stress values of the structure a low as possible, the cavity wall thickness and outer wall profile was slightly optimised during the thermomechanical analysis. The original inner profile of the cavity which

has already been validated experimentally is identical to the previous “copper-cavity” design and was not changed.

Modifications on the measurement probe: At the entrance of the cavity, an isolated capacitive probe is installed which is used for the verification of the position of the gyrotron in the magnet and estimation of the existing misalignment between the magnetic axis of the magnet and mechanical axis of the resonator.

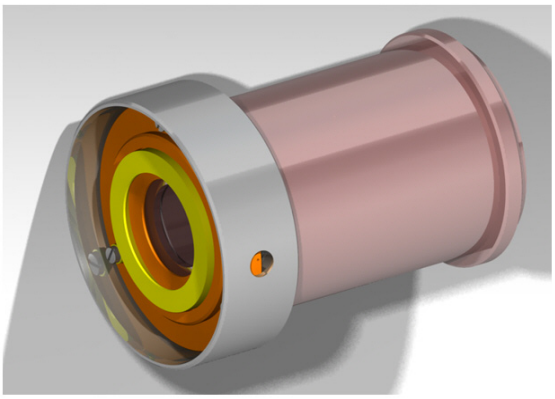

Fig. 1.3.1
CAD model of the gyrotron cavity made of Glidcop

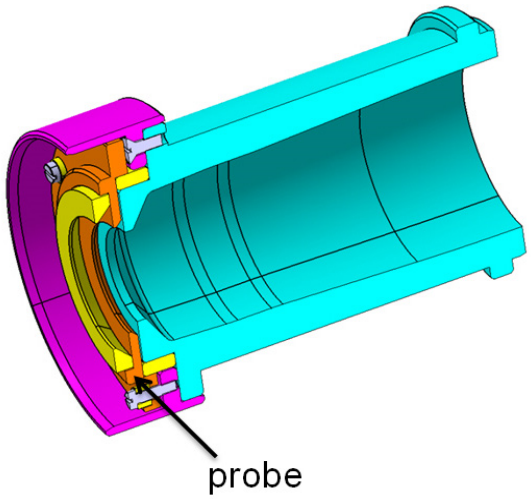

Fig. 1.3.2
Improved measurement probe

The measurement takes place at the reduced magnetic field and with low-energy electron beam at ~5 kV accelerating voltage and total beam current ~100 mA. Before the measurement starts, the radius of the electron beam is set to be close to the inner radius of the probe. After that, using the existing dipole coils, the position of the beam is changed in the lateral plane in order to intersect with its electrons the edge of the probe. Due to the measurement of the dependency of the current to the probe with respect to the applied dipole currents, and based on the analysis of the symmetry of the measured current profiles to the probe, the displacement of the cavity position with respect to the magnetic field can be found. In the previous cavity design the position of the probe was not sufficiently well fixed to the cavity and could be displaced in case of further modifications performed on the gyrotron setup (i.e. replacement of the beam tunnel). In the improved design the probe is permanently connected to the cavity as presented in Fig. 1.3.2, which prevents a possible probe displacement during the component installations.

In order to verify the fabrication of the new cavity, the component has been installed in the 2 MW, 170 GHz coaxial-cavity short-pulse gyrotron for tests. The main goal was to validate the gyrotron output frequency at the nominal $TE_{34,19}$ mode, as well as the efficiency of the RF power generation. The tests have been done at a reduced magnetic field (~6.67 T) without activated normal conducting (NC) coil. The obtained results were in very good agreement with results achieved with the previous version of the cavity. Furthermore, an excellent agreement with the theory has been met. At reduced magnetic field, an RF power close to 1.8 MW with reasonable efficiency around 30 % has been achieved. The pulse length was around 1 ms. In addition, the resulted frequency at the nominal mode was between 169.882 GHz and 169.972 GHz (depending on currently applied value of accelerating voltage), being within specification. It confirmed also a good accuracy of the cavity fabrication. The measured results are presented in Fig. 1.3.3.

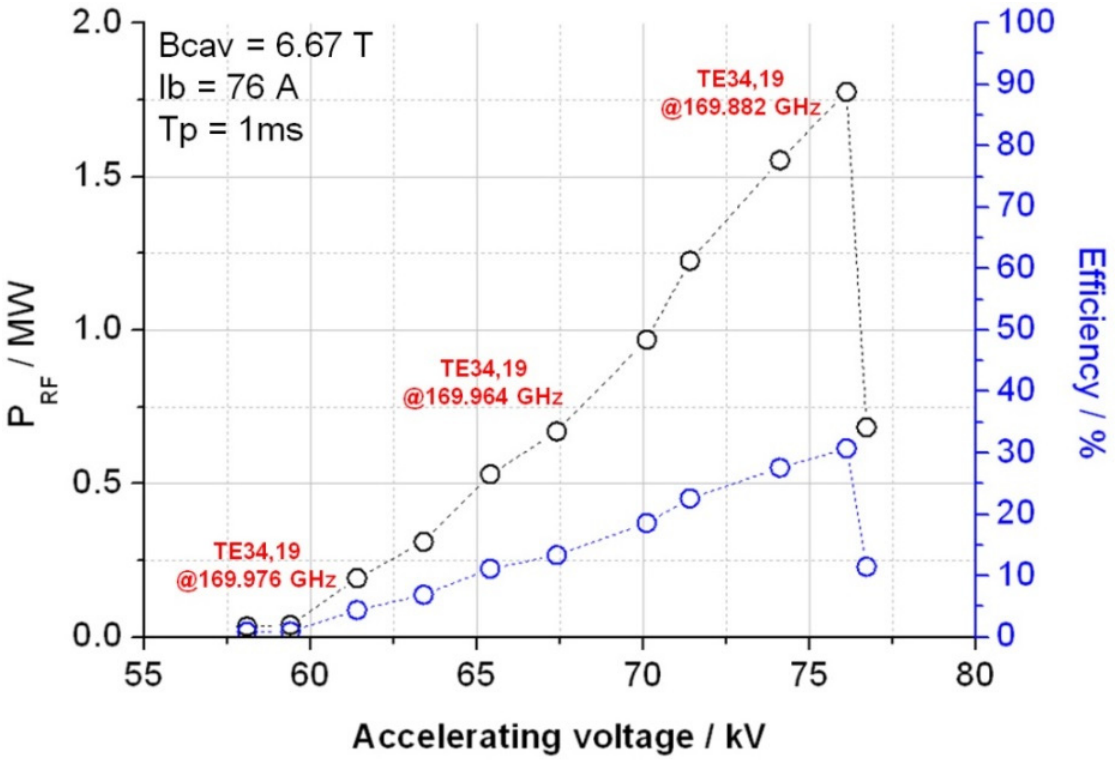

Fig. 1.3.3
Measured RF power and efficiency as a function of the accelerating voltage achieved with the modular short-pulse gyrotron equipped with the improved cavity made of Glidcop.

1.3.3 Preparation of the gyrotron setup for longer pulse operation

In order to increase the gyrotron pulse length, all subcomponents such as cavity, launcher, beam tunnel, mirrors and the collector have to be equipped by active cooling system. One of the main project requirements is the conservation of the modularity of the gyrotron. The concept is based on an independent cooling system implemented for each component. It allows the monitoring of the the internal losses in each gyrotron component and of the final energy balance of the tube during long pulse operation.

The following constrains for the thermomechanical analysis have been assumed: water flow with a velocity of 8.14 m/s (a non-laminar flow in order to increase the cooling power) and RF power dissipation of 50 kW in the cavity (which relates to a wall loading of ~2 kW/cm²). The limitation of the pulse length is a maximum allowed cavity temperature of 350 °C. The simulation results show a maximum pulse length of 1 s. The simulated radial deformation, at a cavity temperature of 350 °C, amounts to 50 µm. The occurred frequency shift is 280 MHz due to the increasing cavity radius. In a first step the launcher, cavity and beam tunnel are optimised for long pulse operation. The modifications will be described following and are shown in Fig. 1.3.4.

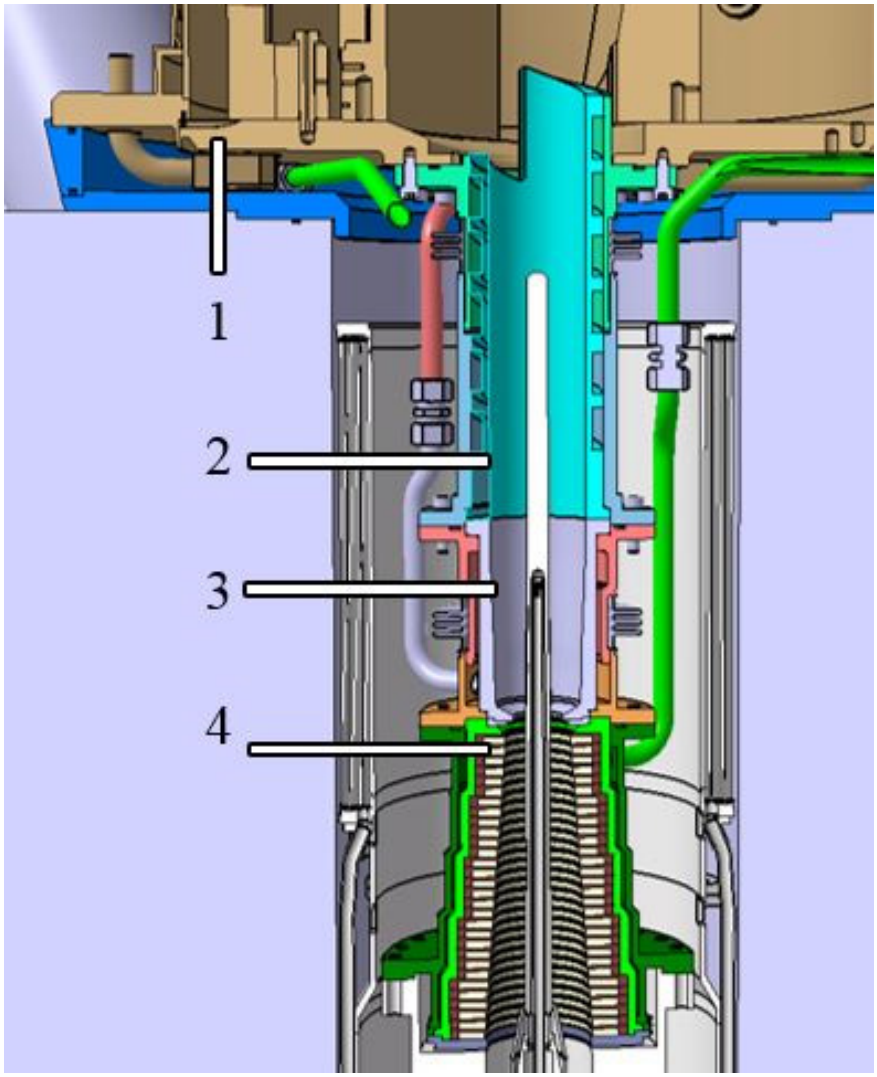

Fig. 1.3.4
Overview of the proposed cooling system for the most critical gyrotron subcomponents (1-mirror box, 2-launcher, 3-cavity, 4-beam tunnel).

Launcher: The launcher together with the following mirror system is responsible for the conversion of the main $TE_{34,19}$ mode into a fundamental Gaussian mode. During the mode conversion process the power loading at the launcher surface is very high. Especially the top part of the launcher in the area of the launcher cut, where the complete RF-power is finally focused, is critical. In order to guarantee a stable operation it has to be fulfilled that also the top of the launcher will be cooled. Unfortunately, this requirement presents some challenges, because the top part of the launcher is extended by 60 mm into the mirror box where no access from outside of the gyrotron exists. Therefore the water entrance and outlet have to be supplied from the bottom and the water flow is implemented in a helix likewise flow (see Fig. 1.3.5, right). At the top of the launcher, both helical channels will be connected in the so called “breakthtrough”. In lower regions of the launcher the channels go into “reservoirs”, where the channels end. Due to the complex structure, the channels have to be milled with a 5-axis milling cutter. In order to caulk the channels, a stainless steel coat will be imposed and welded from the outside of the launcher. Due to the fact that the launcher and coat exist of different materials that have different thermal extension coefficient, a bellow is necessary to compensate the forces as it is depicted in Fig. 1.3.5 (left).

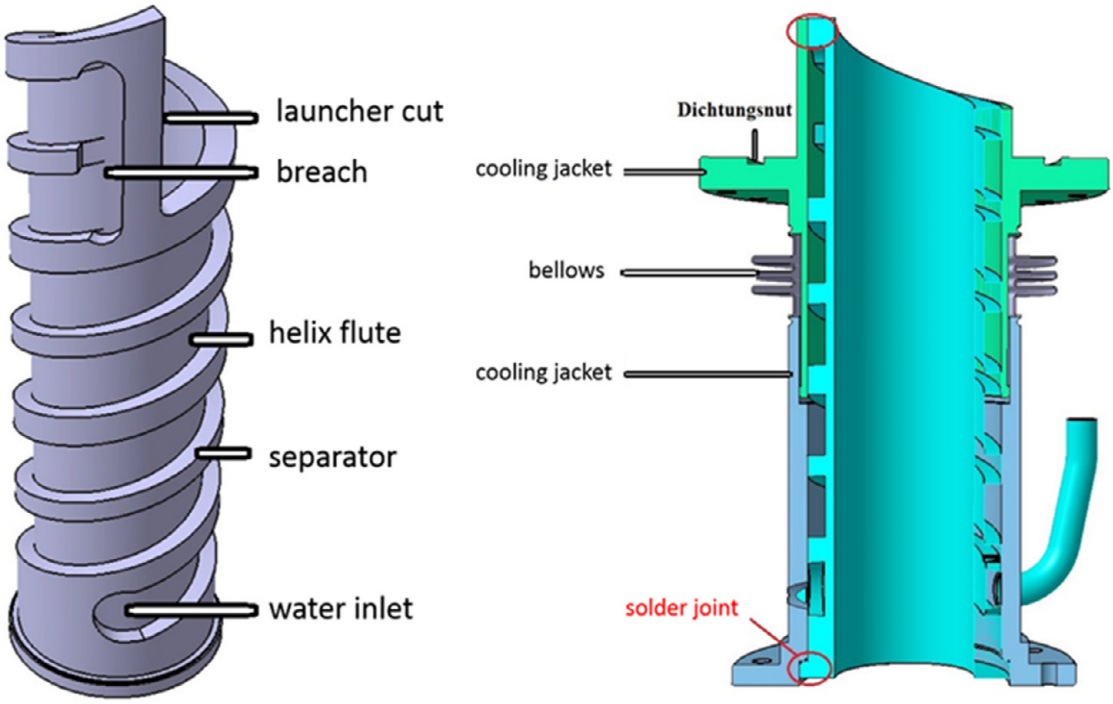

Fig. 1.3.5
Longer pulse cavity design with helical cooling channel (left) and launcher cooling.

Cavity: The cavity is the region where the RF power is generated due to interaction between the electrons and the RF field. The power loss at the surface of the cavity is 50 kW. The highest power loading ~2 kW/cm² takes place at the centre of the cavity (region with constant diameter). It leads to the extremely high temperature gradient at the inner cavity wall, which results in thermal stress and deformation. The frequency of the RF-wave depends strongly on the diameter of the cavity and hence strongly on the deformation and thermal expansion. Therefore it is inalienable to implement a water cooling system for the cavity in the longer pulse operation regime. The approach of the active cooling system is similar to the design of the launcher. However, due to the position and orientation a helix channel system is not necessary. The different temperatures, material properties of the coat and outer cavity wall require also the implementation of a bellow. The reduction of the water cooling gap (see Fig. 1.3.6) increases the velocity of the water and therefore the cooling power. The limitation of the cavity is a maximum temperature of approximately 350 °C. The *COMSOL* simulation result, shown in Fig. 1.3.6, represents the temperature of a pulse with duration of 1 s. The maximum temperature of 323 °C is, as expected, at the centre of the cavity. The resulting mechanical stresses for the presented configuration amounts to 500 MPa.

Beam tunnel: The beam tunnel consists of stacked copper and ceramic rings. Compared to the cavity, the power loading is relatively low. However, the structure is very sensitive to the excitation of the parasitic modes that can significantly increase the level of power losses in the beam tunnel. Therefore the active cooling seems to be obligatoryFig. 1.3.7 shows the construction of the beam tunnel including the water cooling system. A coat is also welded to the outside and forms with the outer metal layer an annular gab cooling.

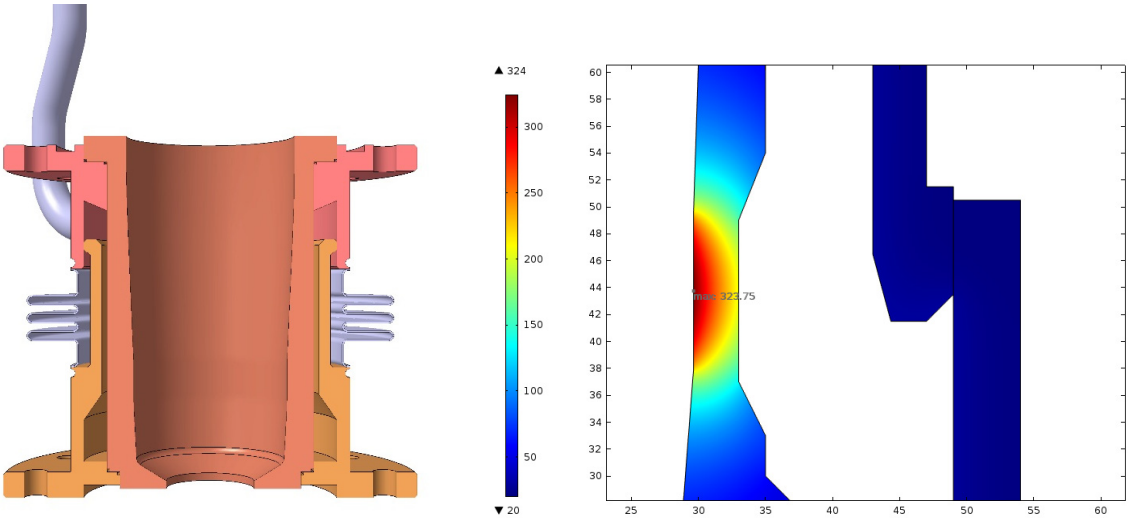

Fig. 1.3.6
Gyrotron cavity design with active cooling jacket. COMSOL cavity simulation results for 1 s pulse length.

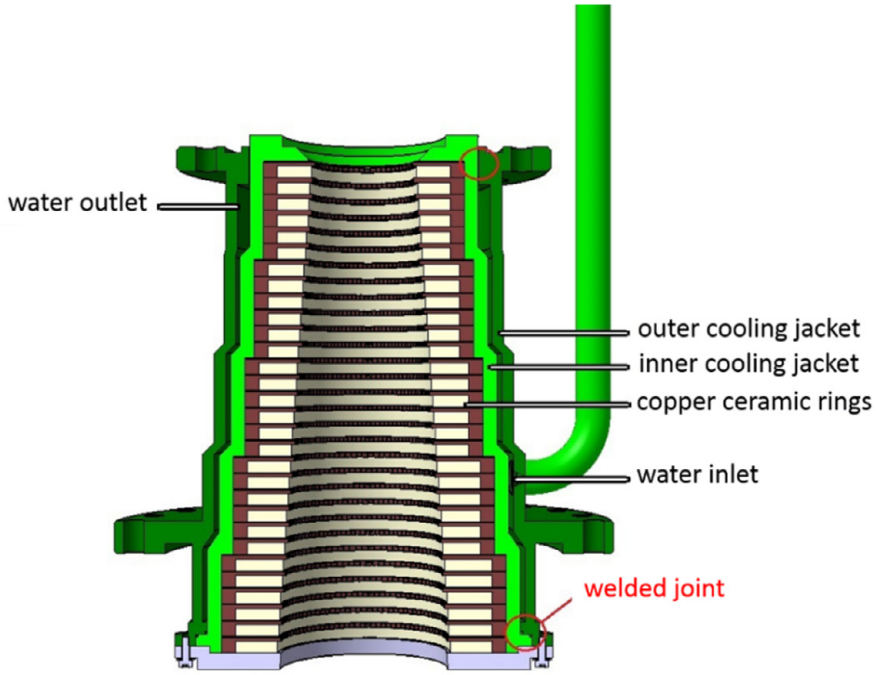

Fig. 1.3.7
Annular gap cooling of the beam tunnel.

Magnetron injection gun: Key point for the successful operation of the modular coaxial cavity gyrotron in longer pulse length is the suppression of the electron trapping mechanisms in the gun region. A triode gun which satisfies all design criteria for the suppression of the trapped electrons has been completed. No potential well is formed in the rear part of the gun and the low pitch factor of electrons emitted from the cathode surface ensures the suppression of the harmful beam halo generation. All other criteria concerning the beam quality and the electric field limitations for stable voltage stand-off are also satisfied.

1.3.4 Inverse Magnetron Injection Gun

1.3.4.1 Introduction

An important criterion for stable gyrotron operation and the operation with longer pulses is the suppression of the electron beam halo which is caused by the magnetically trapped electrons in the region between the cathode and the cavity. Theoretically, different reasons can contribute to the generation of magnetically trapped electrons, which are precisely described in. It is very unlikely to prevent the beam halo in most of the designs. Therefore, always, beam halo electrons exchange a small amount of their energy with the system. After some oscillations those electrons gain enough energy to reach the cathode which causes the generation of secondary electrons. The secondary electrons, finally, follow the magnetic field lines towards the cavity. For the gyrotron operation it is crucial that those secondary electrons are not magnetically trapped. In order to keep the magnetically trapped electrons at a low level the gun design has to fulfill the design criteria, which are specified. The first proposal in order to vanish the beam halo is the optimized and advanced design of an inverse magnetron injection gun (IMIG).

1.3.4.2 Magnetron Injection Gun Geometry

The proposal for an inverse MIG is presented in Fig. 1.3.8. The construction was optimized by using the self-consistent, electrostatic trajectory 3D code *Ariadne.* The optimization was realized for the cathode, body, insert and anode in order to minimize the electron velocity spread of the electron beam and to provide the appropriate electron pitch factor, beam thickness and beam radius at the cavity. In addition, the gun was optimized in order to suppress the trapping mechanism.

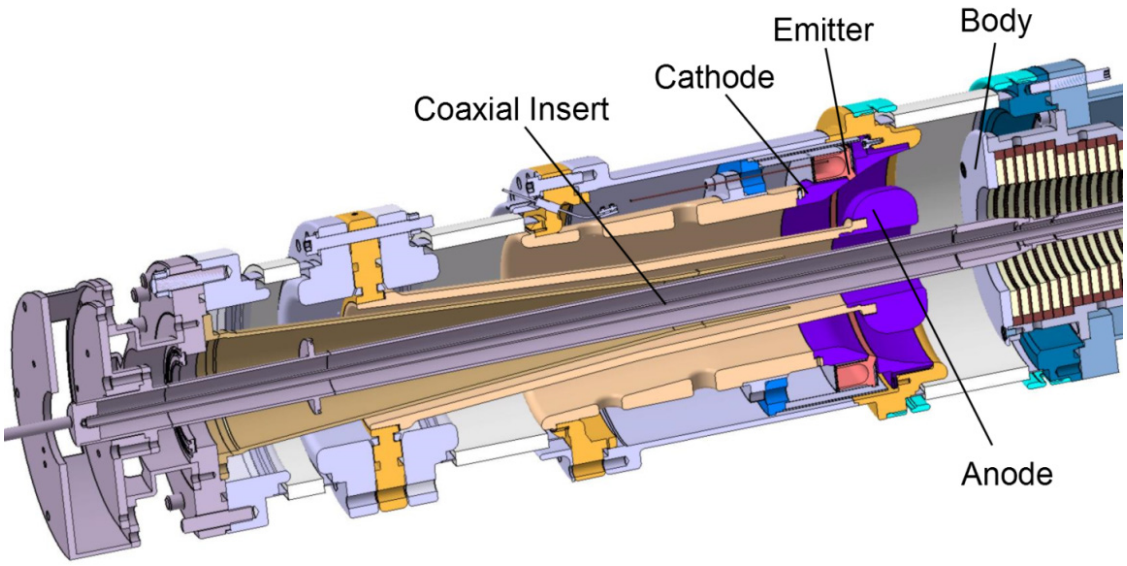

Fig. 1.3.8
Design of the coaxial magnetron injection gun in triode configuration

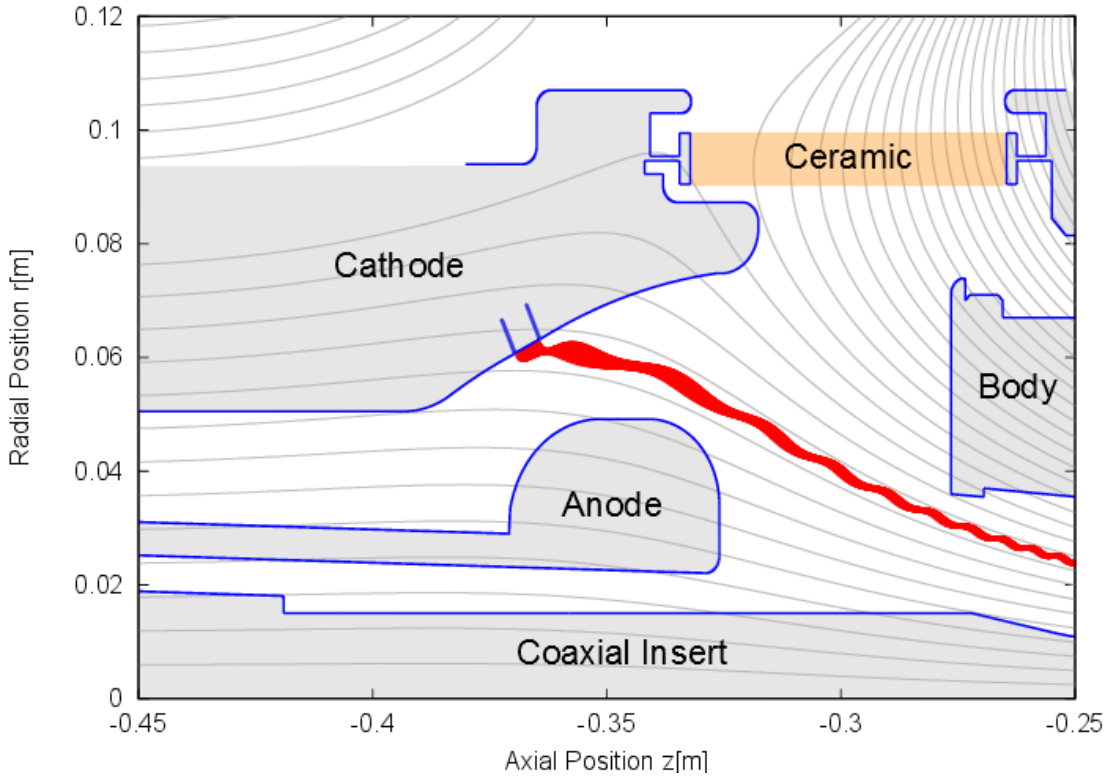

Fig. 1.3.9
Geometrical shape of the electrodes with magnetic field lines and electron trajectories.

The detailed profiles of the electrodes including the magnetic field lines and the electron beam trajectories are shown in Fig. 1.3.9. Fundamental for the design is the emission of the electrons from the emitter inwards, towards the axis of the gyrotron. Immediately, a much larger radius of the emitter ring can be used without to increase the total size (diameter) of the MIG construction. In the present design the emitter radius was fixed to 62 mm with a horizontal emitter thickness of 5 mm. The emitter is slanted at an angle of 25 degrees with respect to the axis of the tube.

The final beam quality is one of the most important criterion in the design of a MIG. It determines the excitation of the correct operating mode, and, it is dominating the achievable efficiency of the gyrotron. Therefore, an appropriate electron beam is required which has to fulfill the following design criteria:

(a) the beam average radius r_b must have a value very close to the first maximum of the operating TE mode;

(b) the beam thickness Δr_b (expansion of guiding center) should be less than the fifth of the wavelength ($\Delta r_{b,max}$ = 0.35 mm at 170 GHz) in order to achieve an efficient interaction;

(c) the average pitch factor α should be in the range between α = 1.2 and α = 1.4;

(d) the transverse velocity spread $\delta\beta_t$ should be minimized. For the nominal electron beam parameters (seeTable 1.3.1) the simulated operating parameters are summarized in Table 1.3.2. These parameters are simulated at the center of the cavity and satisfy the demanded specifications.

Beam Voltage V_{beam}	90 kV
Beam Current I_b	75 A
Cavity Magnetic Field B_{cav}	6.86 T

Table 1.3.1
Nominal operating paramenters.

Radius Guiding Center R_g	10 mm
Beam Thickness Δr_b	0.3 mm
Pitch Factor α	1.3
Velocity Spread $\delta\beta_t$	2.4 %

Table 1.3.2
Beam parameters at the cavity.

1.3.5 Electric Field Optimization

The amplitude of the electric field under consideration of the space charge is shown in Fig. 1.3.10. The highest amplitude of the electric field is located at the anode nose. It reaches a value of approximately 76 kV/cm. The highest amplitude of the electric field on the cathode surface is about 43 kV/cm. The limit for the maximum electric field is assumed to be 82 kV/cm for the anode surface and 65 kV/cm for the cathode. As can be seen from Fig. 1.3.10 the design criteria concerning the maximum electric field are satisfied in the new proposed MIG.

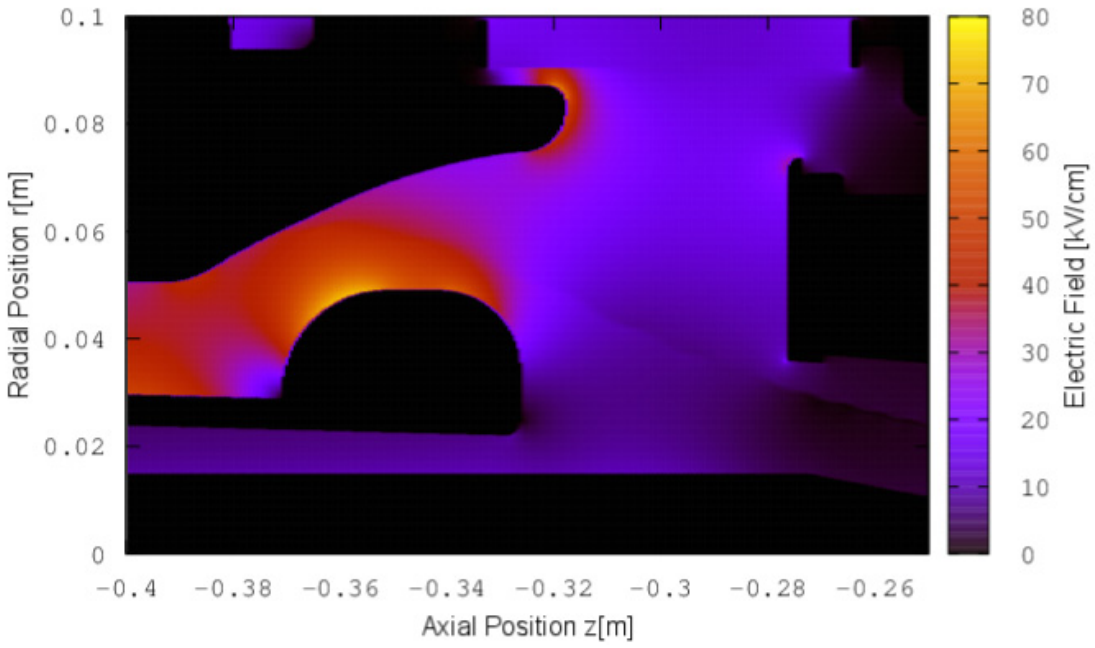

Fig. 1.3.10
Electric field strength of the inverse MIG in the cathode region.

1.3.6 Suppression of Beam Halo

Recent experiments have shown that the correlation between the existence of trapped electrons and limitations in the final gyrotron operation. An important criterion for stable gyrotron operation is the suppression of the electron beam halo which is caused by the magnetically trapped electrons in the gun region. Theoretically, different reasons can contribute to the generation of magnetically trapped electrons. It is very unlikely to prevent the beam halo in most of the designs. Therefore, always beam halo electrons exchange a small amount of their energy with the system. After some oscillations those electrons gain enough energy to reach the cathode which causes the generation of secondary electrons. The secondary electrons, finally, follow the magnetic field lines towards the cavity. For gyrotron operation it is crucial that those secondary electrons are not magnetically trapped. The following basic criteria for the electron beam, which are published in [8], prevent trapped electrons:

(a) no magnetic field line cross the same equipotential line twice (magnetic potential well);

(b) all secondary electrons emitted from the cathode surface should not be magnetically trapped;

(c) low pitch factor for all electrons emitted from the cathode surface and passing through the cavity need to be achieved.

In order to keep in the IMIG design magnetically trapped electrons at a low level, all electrons from high electric field regions are gathered by the anode and body. For the design of the IMIG the design criteria for the suppression of the trapped electrons have been considered.

The trajectories of the electrons emitted by the cathode surface are shown in Fig. 1.3.11. Electrons which are emitted from the cathode nose (with an electron ID>128) are guided by the magnetic field lines towards the body, while electrons emitted from the cathode prolongator (with an electron ID<52) are collected by the anode. On the other hand, the electrons emitted from the cathode surface close to the emitter ring can pass through the cavity towards the collector. However, the pitch factor of those electrons (Fig. 1.3.12) at the cavity is smaller than α<1.4 and is significantly smaller than the maximum pitch factor of α_{max}=2.63. The calculation of this maximum pitch factor is based on the equation and the assumption of an acceleration voltage U_a = 90 kV, magnetic compression of κ_b=38.4 and an initial transverse kinetic energy of $E_{0\phi}$ = 10 eV.

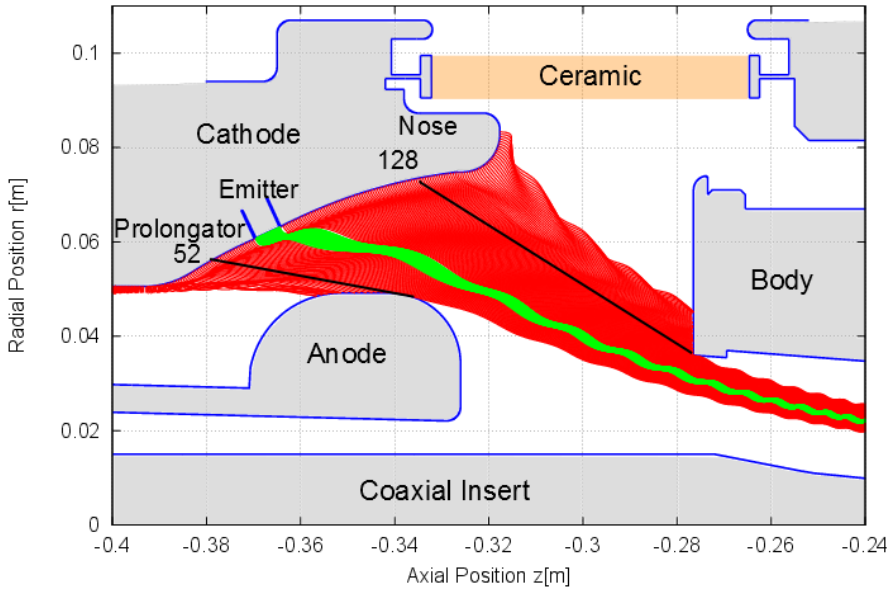

Fig. 1.3.11
Trajectories of electrons emitted from the whole cathode structure.

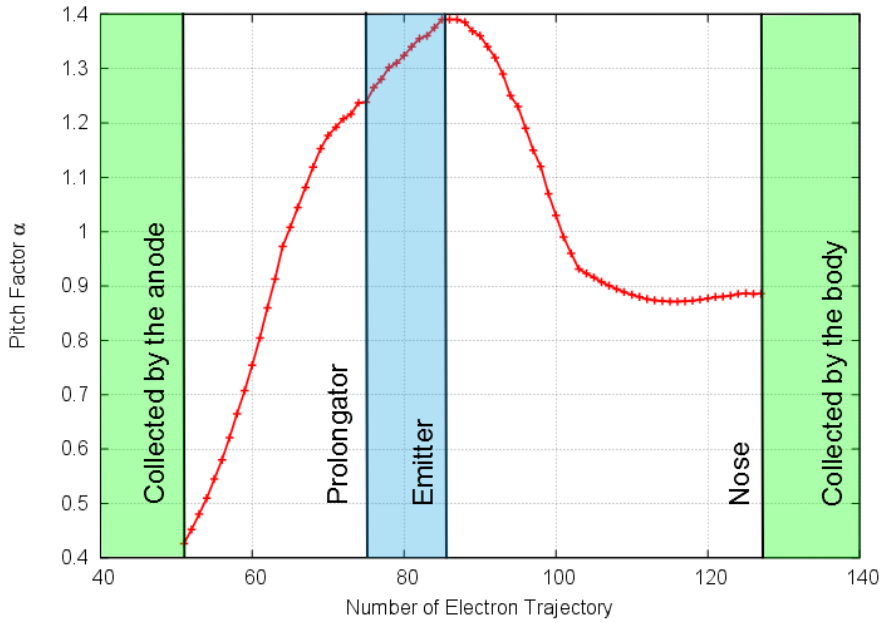

Fig. 1.3.12
Pitch factor of the cathode electrons.

1.3.7 Potential Wells

A further type which is related to trapped electrons is the magnetic potential well. The simulation of the IMIG (Fig. 1.3.13, Case 1) has shown the existence of a potential well in the region of the anode with a depth of ~10 kV. This potential well can be avoided by modifying the anode shape, as it is shown in Fig. 1.3.13 (Case 2), and can be reduced to ~60 V. Unfortunately, by decreasing the potential well depth, the beam quality is decreasing significantly due to a modified anode shape. The influence of the potential well close to the anode will be investigated experimentally by the use of both anode configurations.

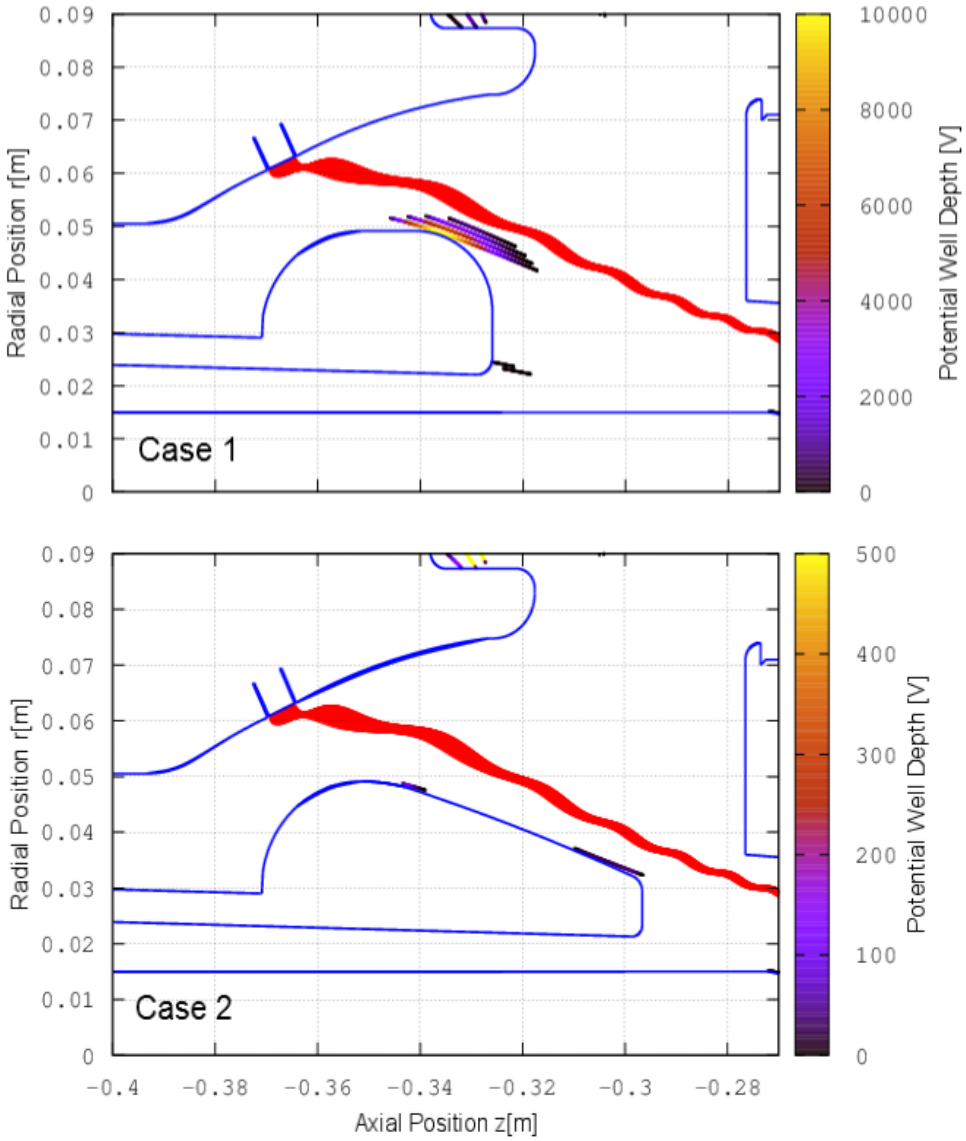

Fig. 1.3.13
Potential well study with different anode shapes.

1.3.8 Investigation of Tolerances and Study of Operating Ranges

Misalignment

The alignment and coaxial alignment of the anode has a significant influence on the quality of the electron beam, and therefore on the generated output power and efficiency. By reason of the long anode (Fig. 1.3.13) and the summation of the tolerances between the anode and cathode, the correct alignment is a critical issue and has to be minimized for mechanical implementation. In addition, the thermal expansion of the anode hinders the adjustment of the anode. The simulation results, presented in Fig. 1.3.14, show the dependency of the beam parameters and the deviation of the radius of the anode, where the nominal case is marked with a black vertical line. The demanded pitch factor α should be in the range between 1.2 and 1.4. Therefore the approved radial deviation is ± 300 µm, while the axial misalignment has a smaller influence within the specified range. The maximum tolerance margin has to be taken into account in the planning of the manufacturing drawings.

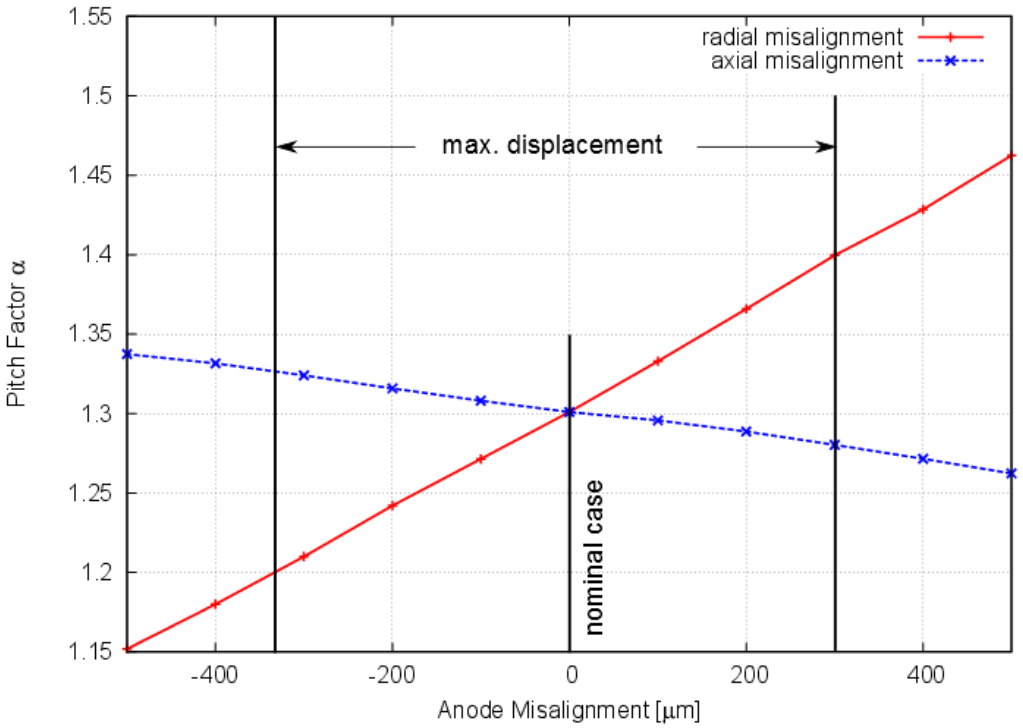

Fig. 1.3.14
Correlation of electron beam pitch factor and velocity spread and the radial misalignment of the anode.

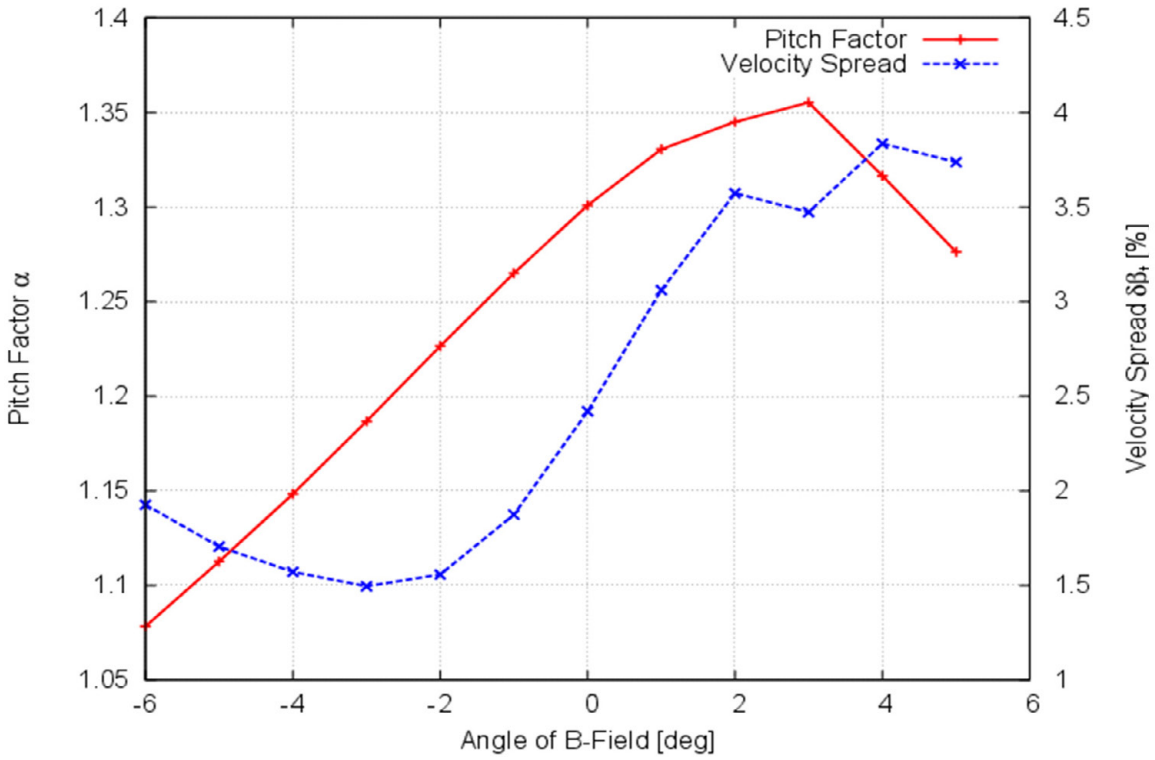

Fig. 1.3.15
Pitch factor and velocity spread in case of a varying magnetic field line angle at the emitter region.

Magnetic Field Margin

The beam parameters α and $\delta\beta_t$ depend strongly on the magnetic field distribution in the gun region. The variation of the trajectory inclination angle in the gun region can be achieved by an adjustable coil current. The magnetic field angle at the emitter position was varied between -6 degree and +5 degree. The simulated pitch factor α and velocity spread $\delta\beta_t$ are shown in Fig. 1.3.15. The pitch factor increases from -6 degree up to an angle of 3 degree and decreases for higher angles, while the strength of the magnetic field remains approximately constant. In the nominal case (0 degree) the pitch factor is 1.3. The pitch factor varies from 1.06 to 1.36, which corresponds to a deviation of 22.1 %. The transverse velocity spread could be considered low for all magnetic field configurations.

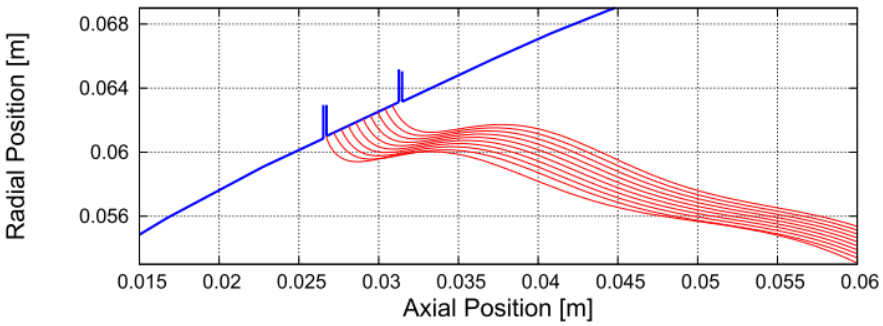

(a) Laminar Beam ϕ_B < 0 degree
magnetic filed angle < 0°

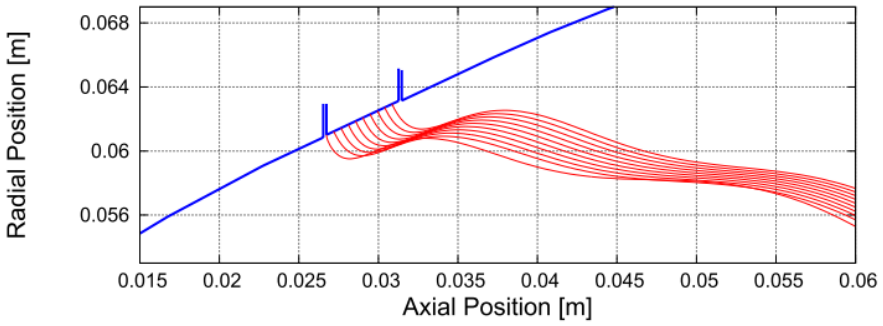

(b) Quasi-Laminar Beam φ_B = 0 degree
magnetic field angle = 0°

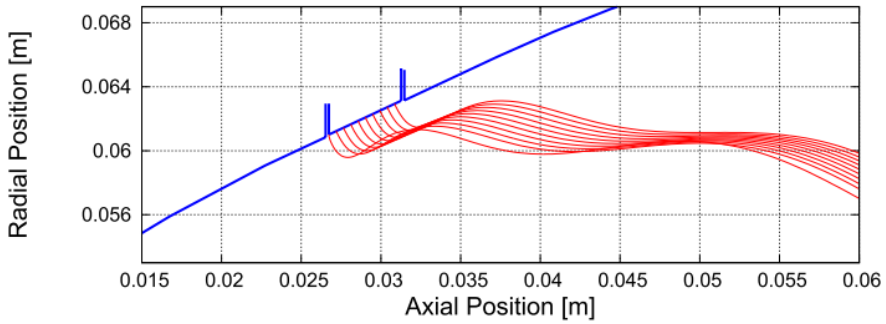

(c) Non-Laminar Beam ϕ_B > 0 degree
magnetic field angle > 0°

Fig. 1.3.16
Electron trajectories near the emitter surface for different magnetic field distributions.

In Fig. 1.3.16 (a)-(c), the shape of the beam at the region of the emitter ring for 3 different magnetic field angles are plotted. For < 0 degree the beam is approximately laminar, in the nominal case quasi-laminar, while for > 0 degree the beam is non-laminar since the electron trajectories are intersecting each other.

Emitter Study

The emitter has a radius of 62 mm and an angle of 25°. The surface roughness amounts 0,8 µm which corresponds to the best trade of between emissivity and electron velocity spread. The emitter is impregnated with BaO, CaO and Al_2O_3. For an increasing live time the emitter was finally coated with Osmium and Ruthenium (M-type coating). The nominal operating temperature is at 1000°C (Fig. 3.1.17, left) which corresponds to a filament current of 24.095 A and a filament power of 987 W. The temperature distribution of the emitter at nominal operation is amounts ± 7°C, measured with an optical pyrometer.shown in Fig. 3.1.17 (right). The deviation of the temperature:

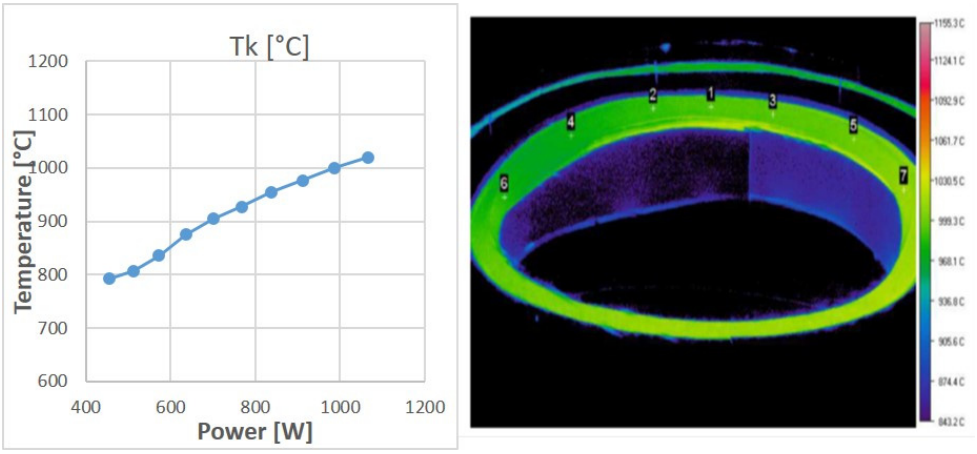

Fig. 1.3.17
Emitter surface temperature versus the filament power and obtained uniformity of the temperature distribution at the emitter surface.

1.4 EUROfusion: Research and development towards a Gyrotron for future DEMO

1.4.1 Physical design of a coaxial-cavity gyrotron

The physical design of the triode-type coaxial magnetron injection gun (tCMIG) was finalized, using the codes *Ariadne* (on the HELIOS supercomputer) and *Esray*. See Fig. 1.4.1 for details. The magnet design received last year was left unchanged.

Gun and cavity were studied with respect to multi-frequency operability, in this case operation at 170.0 GHz, 203.75 GHz and 237.5 GHz, using the codes *Esray* and *Euridice*, respectively. The corresponding modes $TE_{35,21}$, $TE_{42,25}$ and $TE_{49,29}$ have been chosen according to our mode-selection criteria published in January this year. If beam voltage and current are fixed at the values for 237.5 GHz, output power and efficiency will remain above 1.8 MW and 30 %, respectively.

Detailed investigations of the coaxial insert, especially effects caused by the number of corrugations and possible misalignments on mode content and electron beam quality, have been started.

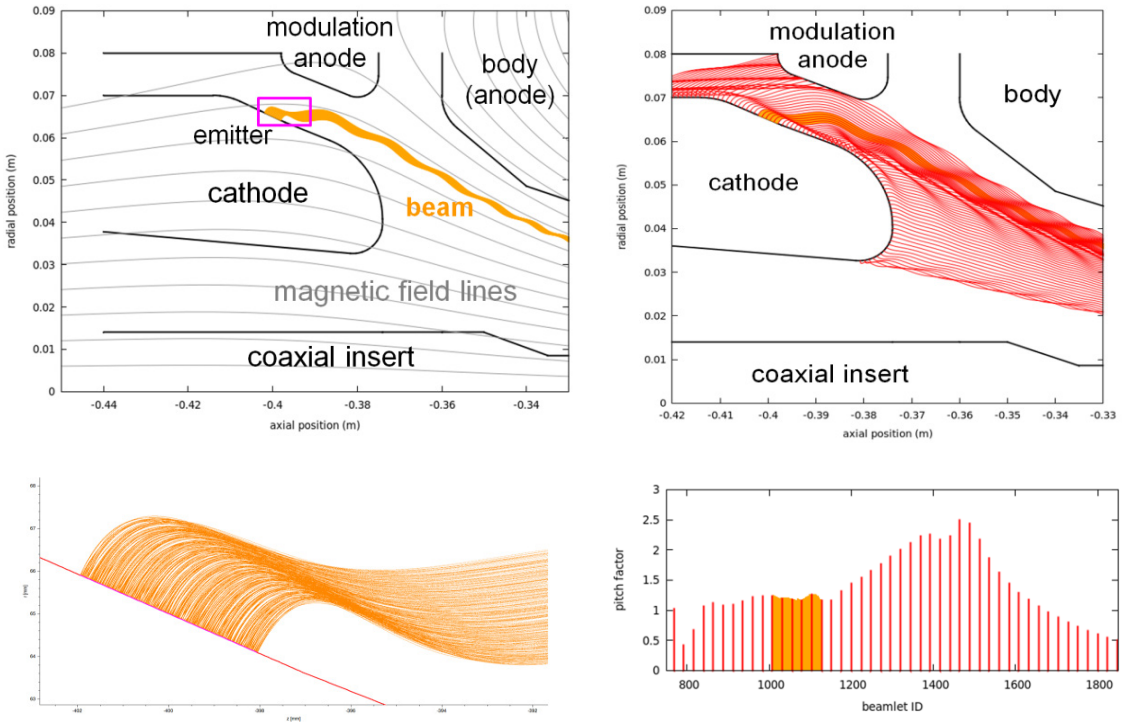

Fig. 1.4.1
Details of the triode coaxial MIG design. Left column: top – general design including magnetic field lines and electron beam; bottom – beam detail at the emitter for surface structure size 20 µm. Right column: top – trajectories of possible secondary electrons (red); bottom – pitch factor histogram of the electrons at the cavity entrance.

1.4.2 Physical design of a conventional cavity gyrotron

The detailed analysis of the interaction section design and a tolerance study of a DEMO-compatible 236 GHz (1 MW) hollow cavity gyrotron have been initiated in 2015. The suitable operating mode series has been selected according to the multi-frequency gyrotron operation and frequency-tunability criteria. Using proposed systematic cavity design approach, the selected cavity design for the analysis is presented in Fig. 1.4.2. Due to higher resistance to thermal softening and radiation damage, a Glidcop material is preferred for the cavity of future gyrotrons. A formula for the temperature and surface roughness dependent conductivity has been derived and incorporated into the simulations. Considering realistic electron beam parameters and realistic conductivity of a Glidcop material, the multi-mode, time-dependent simulations using *EURIDICE* code suggest a stable RF output of 920 kW with interaction efficiency of 36 % (without depressed collector).

Fast-frequency tunable gyrotrons (tuning within a few seconds) are recommended for plasma stabilization using a fixed, non-movable antenna. To satisfy frequency-tunability requirements of DEMO, suitable operating parameters have been estimated. The step tunability of the 236 GHz gyrotron within the frequency range of ±10 GHz has been theoretically demonstrated in steps of 2-3 GHz (see Fig. 1.4.3). The performance of a gyrotron has been also successfully verified with the operating frequencies of 170 GHz, 203 GHz and 269 GHz to support multi-purpose operations. The effects of electron beam radius on gyrotron operation have been analyzed and found that, a mode competition and a start-up scenario can be improved with an electron beam radius of 9.10 mm instead of the analytically calculated beam radius of 9.06 mm. An electron beam misalignment study with the realistic beam parameters (velocity spread = 6 % and radial

width = λ/4) supports a stable gyrotron operation till radial beam misalignment of 0.317 mm. A beam velocity spread and radial width implementation model have been successfully developed and benchmarked with the TWANG code (interaction code developed at CRPP-EPFL, Switzerland).

The generic methods to find eigenvalue limits for steady state stable gyrotron operation are under investigation. Having information of a mode eigenvalue limit will help to find suitable modes for high output power per tube and to estimate maximum possible output power. Along with the optimized cavity design, the first design of multi-frequency Quasi-Optical Launcher (QOL) have been also suggested which converts high order TE modes into the Gaussian mode. Further optimization of the launcher and designing of the mirror system are progressing.

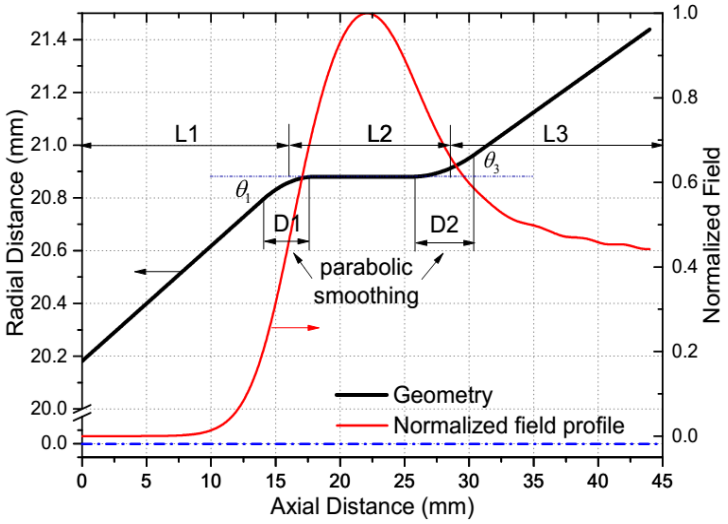

Fig. 1.4.2
Conventional cavity design for the 236 GHz DEMO.

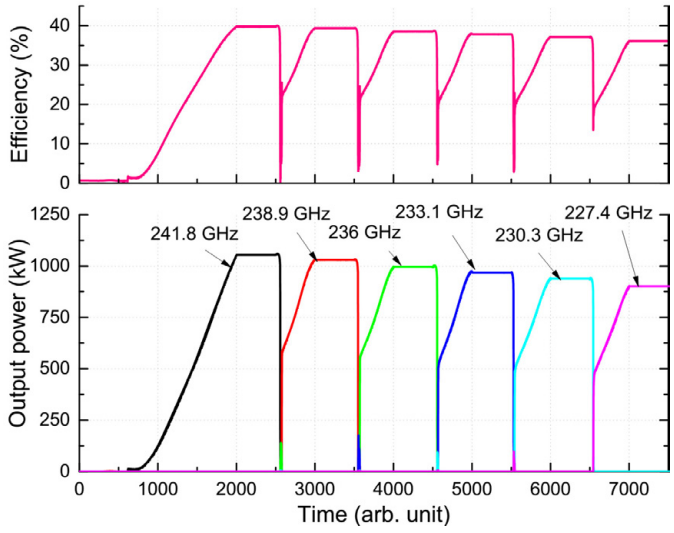

Fig. 1.4.3
Step-wise fast-frequency tuning with a changing magnetic field and beam energy. Stable output power(~ 1 MW) with the interaction efficiency more than 36 % have been achieved at the different operating frequencies.

1.4.3 Multistage Depressed Collector Studies

In gyrotrons, typically an electronic efficiency of up to about 35 to 40 % can be achieved. Consequently, after the interaction a significant amount of energy remains in the electron beam. An enhancement of the overall efficiency is achieved by energy recovery in a depressed collector. The kinetic energy of the electron beam after the interaction with the RF-field in the cavity is partly converted into electrostatic energy, thus reducing the power consumption of the tube and increasing the overall efficiency of the device. Single-stage depressed collectors with efficiency of about 60 % have been successfully used in gyrotrons increasing the overall efficiency of the tube to above 50 %. It is understood that still a huge amount of spent electron beam energy is transformed into heat.

It is possible to increase the efficiency even more by using a Multi-stage Depressed Collector (MDC). A MDC design is based on the configuration of an appropriate electric field using a set of electrodes (stages) and a magnetic field so as to direct electrons of the highest energy to the electrode with the greatest negative potential, the electrons with the lowest energy to the electrode with the least negative potential and the electrons with intermediate energies to electrodes with intermediate voltages to maximize energy recovery. Two concepts have been proposed for the efficient sorting of the electrons on the electrodes. The first one based on the controlled non-adiabatic trajectories and the second based on the ExB drift. Even if several theoretical designs have been proposed for low and high power gyrotrons never a MDC system have been built and experimentally tested in a real gyrotron mainly due to the complexity of the proposed designs.

If the electric potential and the magnetic vector potential have no variation in angular direction of the cylindrical coordinate, then the electron trajectories obey Busch's theorem, which means the cyclotron motions of electrons in the spent electron beam always overlap, no matter how weak the magnetic field is. Thus the trajectories of electrons cannot be fully separated. On the other hand, if the cyclotron motion has a larger dimension of the resolution of fields, electrons can still be sorted locally. In order to make the dimension of cyclotron motion large, we will let the electron beam pass a quickly-decreasing (non-adiabatic) magnetic field. After the non-adiabatic transition, two modulations appear, as shown in Fig. 1.4.4: a) the maximal reachable of radii, b) the axial periodic length; both depend on the kinetic energy of electrons. Based on this modulation, we simulated a MDC, which has 73 % collection efficiency (without considering secondary electrons). The applied depression voltages are 30 keV and 48 keV for the first and second stage, respectively. In the older approach the residual rotational motion of electrons is unwound, non-adiabatic transition of magnetic field is used to keep the transition compact; whereas in this concept, we will use non-adiabatic transitions to modulate the electron beam and the transversal motion is not considered harmful since the electrons can be decelerated also in the radial direction.

Fig. 1.4.5 shows the electron trajectories in the MDC. The electrons are well sorted according to their energy and have a spread over 0.5 m along the z-axis. Even though no electrons are returned back to the cavity; however, the secondary electrons cause a current between electrodes and reduce the efficiency of the collector as visualized in Fig. 1.4.6a. Corrugations on the electrodes surface has been simulated, where the situation with secondary electrons are improved (Fig. 1.4.6b). We will continue investigating method to better suppress secondary electrons.

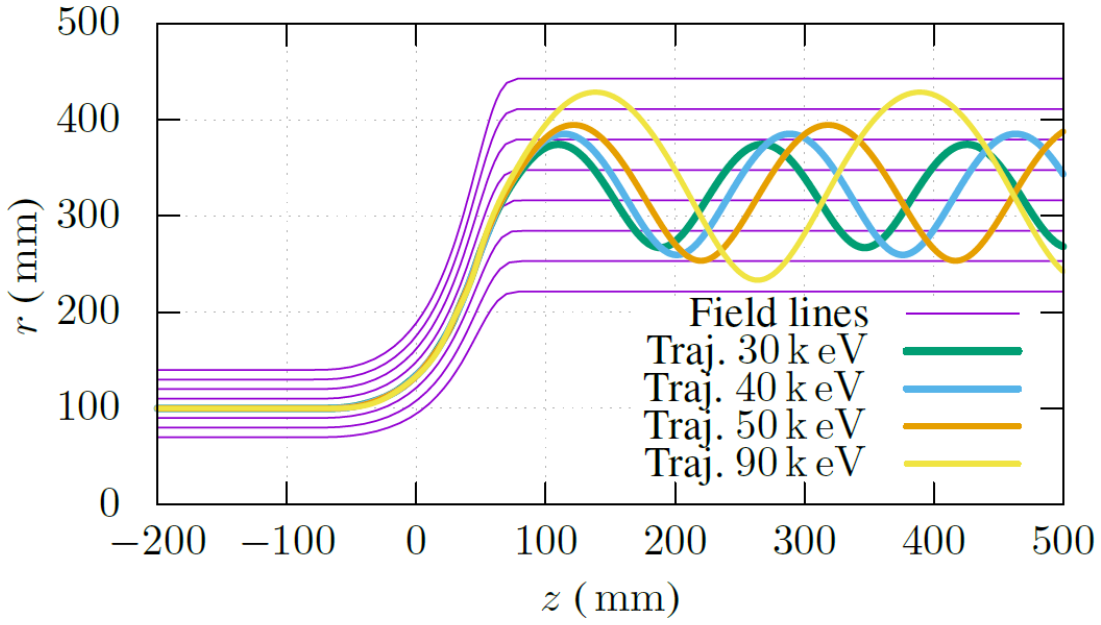

Fig. 1.4.4
Spatial modulation of electron trajectories through a non-adiabatic transition.

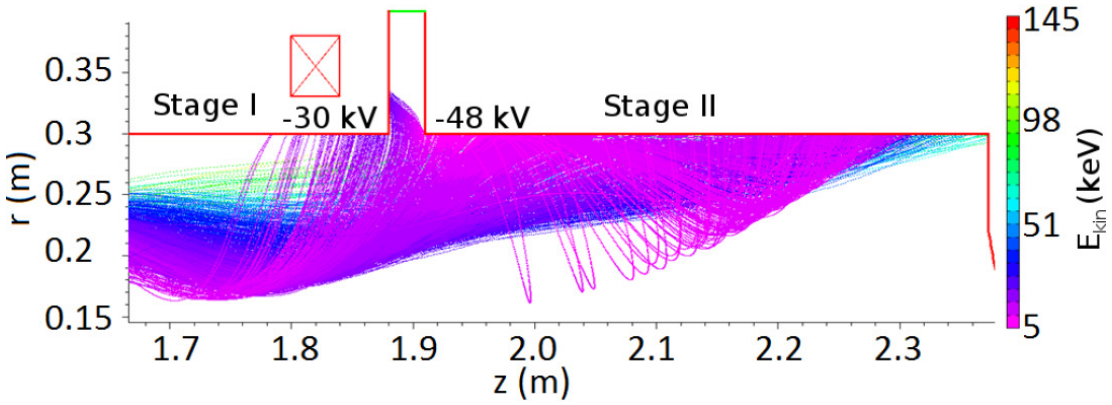

Fig. 1.4.5
Electron trajectories in the two-stage collector.

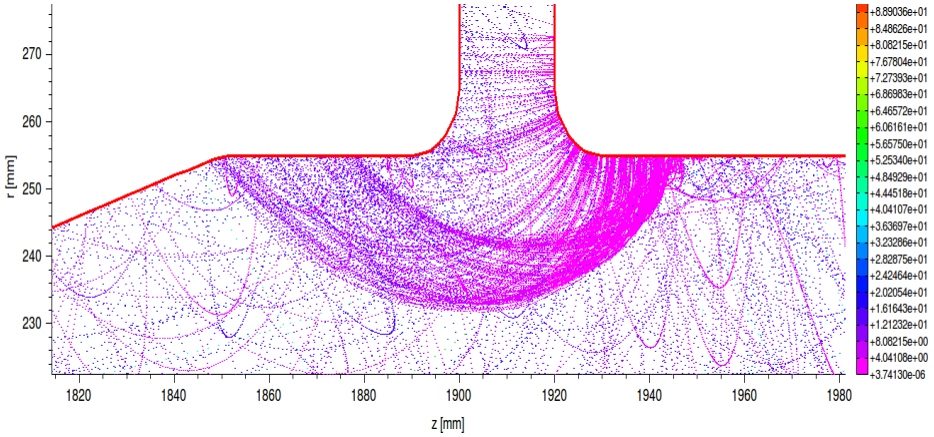

a) Current consisting of secondary electrons

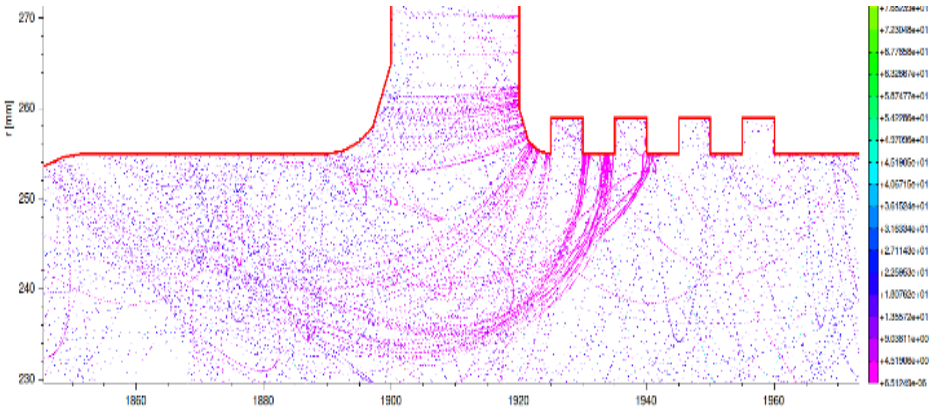

b) Corrugation to reduce secondary electrons

Fig. 1.4.6
Trajectories of secondary electrons.

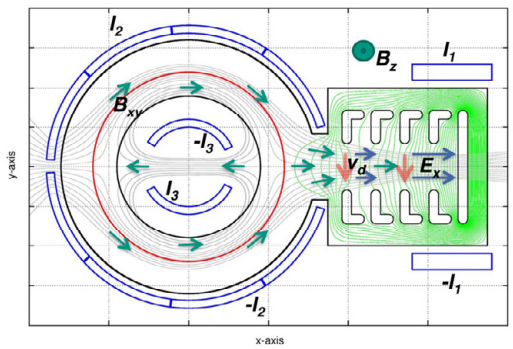

Fig. 1.4.7
Cross-section of the new type of multistage depressed collector system.

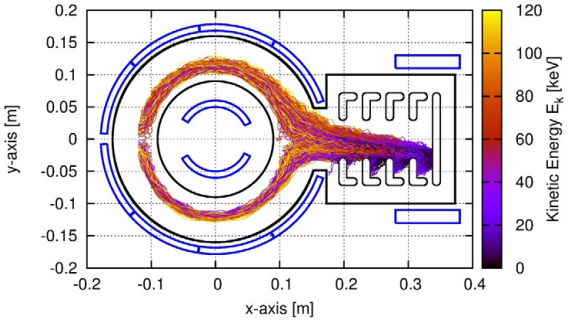

Fig. 1.4.8
Electron beam trajectories in the proposed MDC system.

Another completely different design concept, which may get rid of secondary electron issues is using the ExB drift to sort the electron beam and push the secondary electrons back to the electrodes where they were generated. A new MDC design approach based on the ExB drift concept has been developed during the last year which is much less complex than the other designs based on that concept. It is based on two steps: (i) the transformation of the cylindrical hollow beam to sheet beam, and (ii) the sorting of the sheet beam on the electrodes in order to achieve the optimal efficiency. A cross-section of the proposed collector design is shown in Fig. 1.4.7. A set of normal conducting coils (shown in blue) generates a magnetic field B_{xy}, which guides the initial beam (in red) towards the sector of the beam collection where separation of the electrons according to their initial velocity takes place. The required electric field E_x is generated by a set of electrodes as is shown in Fig. 1.4.5. The operation and the efficiency of the collector depend on the voltage applied on each electrode individually, which, in turn, depends on the initial energy beam distribution of the beam. Each electrode is a long cooled metallic rod fixed at the top or/and at the bottom side of the collector. The drift velocity $v_d = E_xB_z/B$, generated by the electric and magnetic field at the sector of the beam collection region pushes the electrons towards the electrode-set placed in the negative y direction.

Simulations of the proposed design approach with one and three sectors of the beam collection were performed using the upgraded Ariadne code, considering a uniform energy distribution of the spent beam (see Fig. 1.4.8). Collection efficiency of the order of 85 % was demonstrated. Simulation results and new design approach was validated using the commercial code CST. Further simplifications and optimization is planned for the next year.

1.5 Advanced technologies for future high-power gyrotrons

1.5.1 Advanced technologies for future high-power gyrotrons

1.5.1.1 Test of emitter emission inhomogeneity

The emitter emission inhomogeneity will increase the velocity spread, energy spread, guiding center spread of the gyrotron electron beam. Emission inhomogeneity can be measured from the transition region of gyrotron current voltage characteristics (CVC), as shown in Fig. 1.5.1.

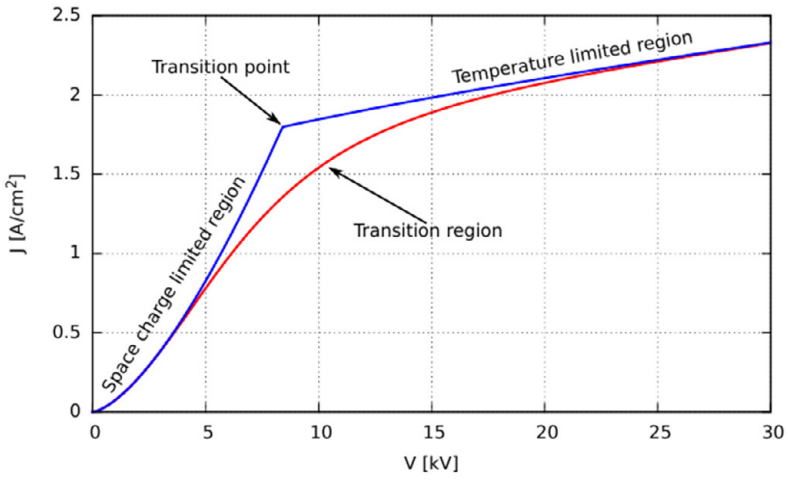

Fig. 1.5.1
Current voltage characteristics of ideal (blue) and inhomogeneous (red) emitter.

An ideal emitter has a transition point between the space charge limited region and temperature limited region while an inhomogeneous emitter has a broader transition region. The test results of CVC measurements for several KIT gyrotrons are listed in Table 1.5.1.

Gyrotrons	10 kW/28 GHz	W7-X SN7I	W7-X SN5I	ITER 170 GHz	Coaxial-cavity
δ_J	0.27	0.17	0.08	0.05	0.66

Table 1.5.1
Emitter emission inhomogenity values (relative standard deviation of the current density) for several KIT gyrotrons.

The influence of the emission inhomogeneity on the electron beam quality is calculated using the 3D electrostatic code *Ariadne*. Its influence on gyrotron efficiency is calculated using the code *Euridice*. The calculation shows that normalized current density distribution δ_J=0.3 will results in 2 % decrease of the gyrotron efficiency.

1.5.1.2 Trapped electrons and low frequency oscillations (LFO) in gyrotron

Due to the surface roughness, emission inhomogeneity and misalignment of the gyrotron MIG some electrons will be reflected from the magnetic mirror even for moderate pitch-factor values ($\alpha \approx 1.3 - 1.5$). These reflected electrons could make lots of problems in the MIG. For example, reflected electrons could bombard the cathode surface and generate secondary electrons. The bombardment will decrease the emitter quality and furthermore will decrease the gyrotron life time. The secondary electrons from the cathode surface other than the emitter surface will also decrease the beam quality. Reflected electrons could accumulate and generate LFO in the MIG. Trapped electrons and low frequency oscillations are two main features which deteriorate the electron beam quality by increasing the velocity and energy spread thus decreasing the stability and efficiency of the gyrotron. These two problems cannot be simulated by the static code since the gyrotron can never achieve a static status with these problem. The quasi-static PIC code *ESPIC* was used for these calculations; the typical LFO of the total space charge is shown in Fig. 1.5.2.

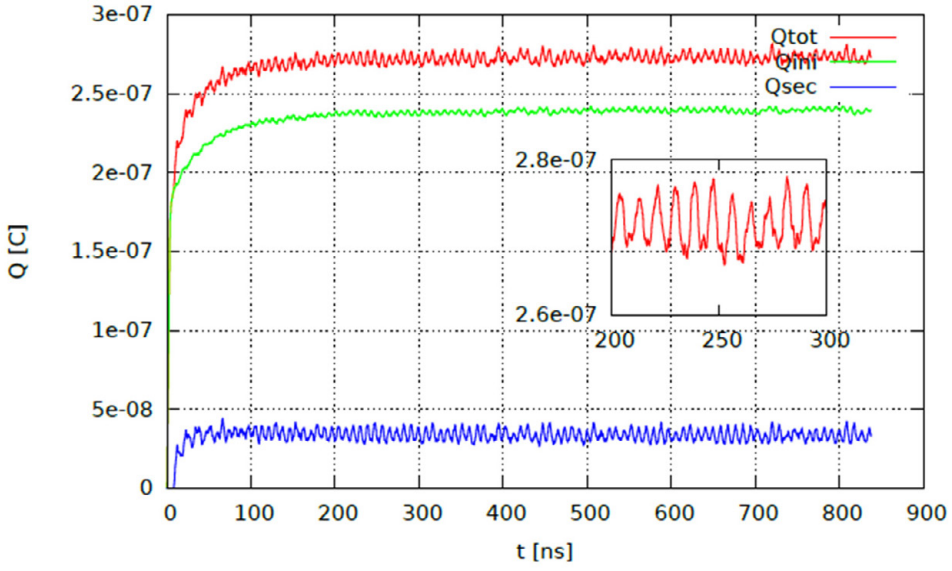

Fig. 1.5.2
Low frequency oscillation of the total space charge in the gyrotron.

1.6 FULGOR (Fusion Long-Pulse Gyrotron Laboratory)

The existing gyrotron test facility at KIT, which had been designed and built about 30 years ago, plays a worldwide leading role in the development of high-power gyrotrons for nuclear fusion applications. This facility offered the unique opportunity to develop and test the first CW high power series gyrotrons for the stellarator W7-X in collaboration with IPP and Thales Electron Devices as the industrial partner.

The target parameters of the new gyrotron test facility are well beyond the capabilities of the existing one. The new teststand will strongly support KIT's leading role in the development of advanced gyrotrons. It will help to answer the questions regarding the technical limits and new physical designs for future high-power microwave tubes. The key parameters of FULGOR will be:

- Full CW operation with up to 10 MW electrical power, corresponding to
  >= 4 MW RF power (assuming an efficiency of the gyrotron >= 40 %)
- Support of advanced energy recovery concepts, e.g. multi-stage depressed collector (MSDC)

The high voltage power supply (HVPS) will support an operating voltage of up to 130 kV with up to 120 A beam current. A superconducting magnet which allows operation of gyrotrons at frequencies well above 200 GHz will be a major component of FULGOR. Other significant components of the teststand will be: cooling system, control electronics and interlock system, RF diagnostics including high-power RF absorber loads.

The capabilities of FULGOR will enable the development and CW tests of gyrotrons for future fusion machines like ITER and DEMO. Fig. 1.6.1 is a simplified CAD view of the complete FULGOR system.

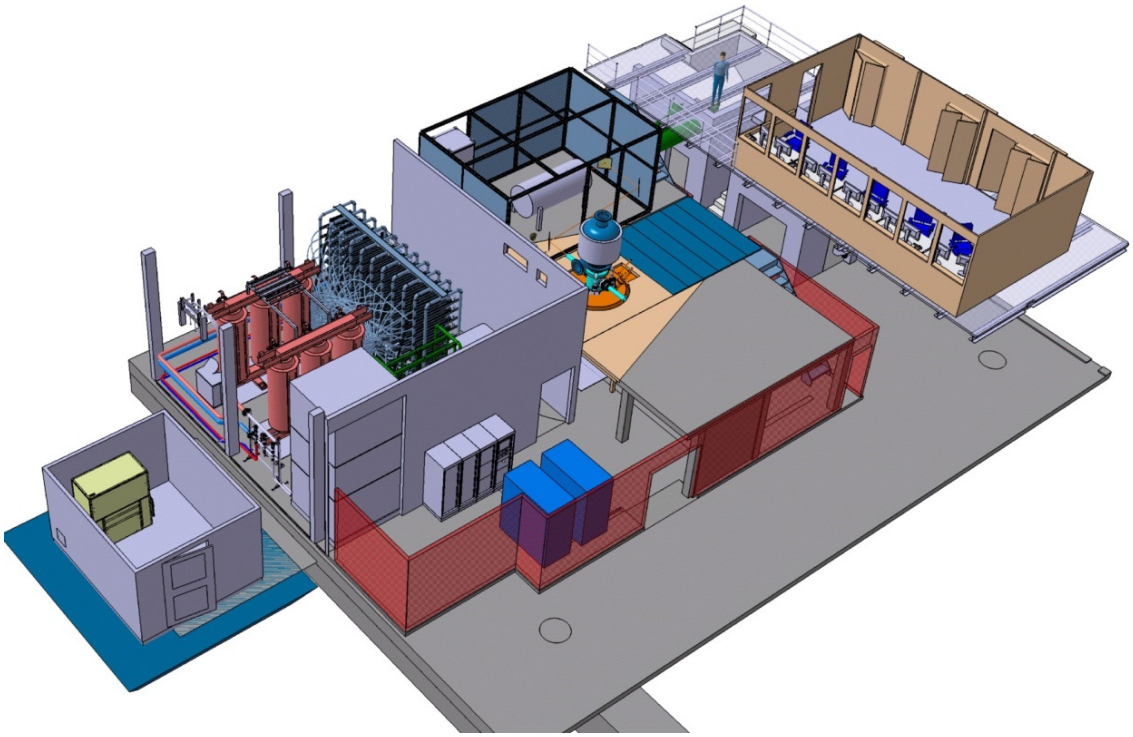

Fig. 1.6.1
CAD view of FULGOR installation including control room.

In 2015 the preliminary and final design of the high voltage power supply has been discussed and agreed with the supplier (Ampegon, CH). According to the agreed schedule delivery of first components to KIT will start in summer 2016.

Substantial progress has been achieved in the planning of the auxiliary systems for plant operation, e.g. 10 MW cooling system and SCADA system. First considerations and discussions with suppliers have been performed for the superconducting magnet and microwave diagnostic system.

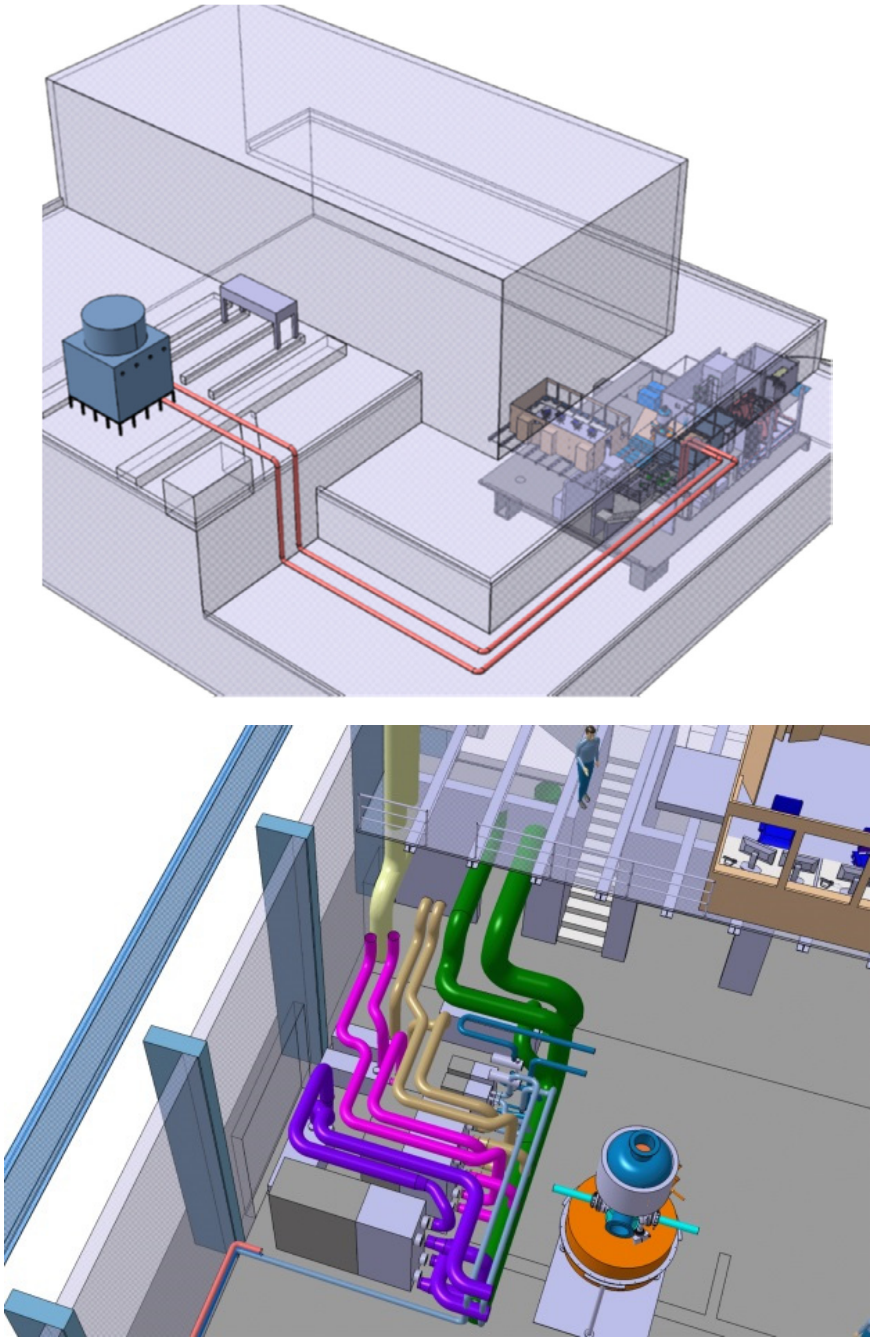

Fig. 1.6.2
Overall view of the cooling system with cooling towers and piping to the test facility (top) and location of cooling manifold (pumps, heat exchanger etc.) close to the gyrotron (bottom).

1.7 Launcher Handling and Testing facility LHT

The Launcher Handling and Testing facility for the ITER ECRH Upper Launcher consists of a prototype test bed for the structural launcher components, like single wall, double wall and blanket shield module (BSM - incl. first wall panel (FWP)). It provides a water circuit with a large range of temperatures and pressures up to ITER bake out (max. 240°C at 4.4 MPa) and the ability to apply fast thermal transients. An experimental verification of normal and baking conditions in ITER can be simulated in a real scenario.

The structural front part of an ECH&CD Upper Launcher consists of the Blanket Shield Module (BSM) which has to meet strong demands on dissipation of up to 3 MW/m³ nuclear heat and maximum 0.35 MW/m² radiation heat, which is why it needs powerful integrated cooling systems. Behind the BSM is another structural component, the Double Wall Main Frame (DWMF), which experiences also nuclear heat. Although this heat is in the order of a tenth of the BSM, integral cooling of the DWMF is required.

The basic design of both components is identical – it features meandering sets of water cooling channels, machined into stainless steel structures and finally formed as welded assemblies. Since such components are not industrial standard, manufacturing of prototypes is essential. Beside specification of an optimum manufacturing route, prove of dimensional accuracy, the main purpose of doing this is to demonstrate the efficiency of the internal cooling channels, which actually depends strongly on a uniform coolant flow in parallel channels. As no electric or pneumatic control devices are permitted in the ITER vacuum vessel, this can be achieved only by installation of individual throttles inside the cooling channels. Position and apertures of these throttles were determined by computer simulations and also the resulting flow scheme was investigated by CFD (Computational Fluid Dynamics)

However, it is essential to compare these simulation´s results with a real test series, which is why the prototypes of BSM and DWMF both were equipped with the full set of cooling channels, throttles and manifolds that is designed for the reference components. Fitting flanges and pipes were installed as well, in order to connect these prototypes to the Launcher Handling Test Facility (LHT) at KIT, where a wide range of ITER operational cooling water scenarios can be applied to test components.

Both prototypes were manufactured by MAN Diesel & Turbo in Deggendorf (Germany) in close collaboration with KIT. After completion and delivery of both double wall prototypes to Karlsruhe, an extensive Test-program at the LHT is under development and will start in 2016. The figures below show the prototypes during manufacturing and as they were delivered.

Fig. 1.7.1
DWMF and BSM prototypes for testing at LHT.

1.8 Complementary Work

1.8.1 Cavity design for the TCV 126 / 84 GHz 1 MW gyrotron

In view of a TCV upgrade, a dual-frequency 1 MW gyrotron, based on the configuration of the 1 MW, 140 GHz gyrotron for W7-X, has been designed in collaboration with EPFL/SPC, Lausanne and is currently under procurement. The operating frequencies are 126 GHz and 84 GHz and the targeted pulse length is 2 s. Three alternatives for the cavity have been investigated, which have been obtained by increasing the midsection of the W7-X gyrotron cavity by 4 mm, 5 mm, and 6 mm, respectively. (A length increase is necessary in order to adapt from 140 GHz to the lower frequencies of 126 GHz and 84 GHz.) Investigations on optimum operating points have been performed, supported by realistic multi-mode start-up simulations by EURIDICE to validate the operation of the three cavities at the two prescribed frequencies. It turns out that the cavity with 5 mm longer midsection is the best compromise in terms of power and efficiency at both frequencies, as well as ohmic wall loading. This is the configuration selected for the final design of the gyrotron. The simulated performance of this cavity at the two frequencies, considering a realistic electron beam with a 6 % rms spread in perpendicular velocity and a guiding-center spread of two Larmor radii, is shown in Fig. 1.8.1. At the operating point of 78 kV, 40 A, and assuming a pitch factor α = 1.3, the $TE_{26,7}$ mode delivers at 126.15 GHz a power of 1.23 MW (at the end of the cavity) with 41 % interaction efficiency and 2.1 kW/cm^2 ohmic wall loading, whereas the $TE_{17,5}$ mode delivers at 83.91 GHz a power of 1.06 MW with 35 % interaction efficiency and 1.1 kW/cm^2 ohmic wall loading. The actual power at the gyrotron window is expected to be typically ~5 % lower, due to the additional losses between the cavity and the window. The ohmic loading is within acceptable limits.

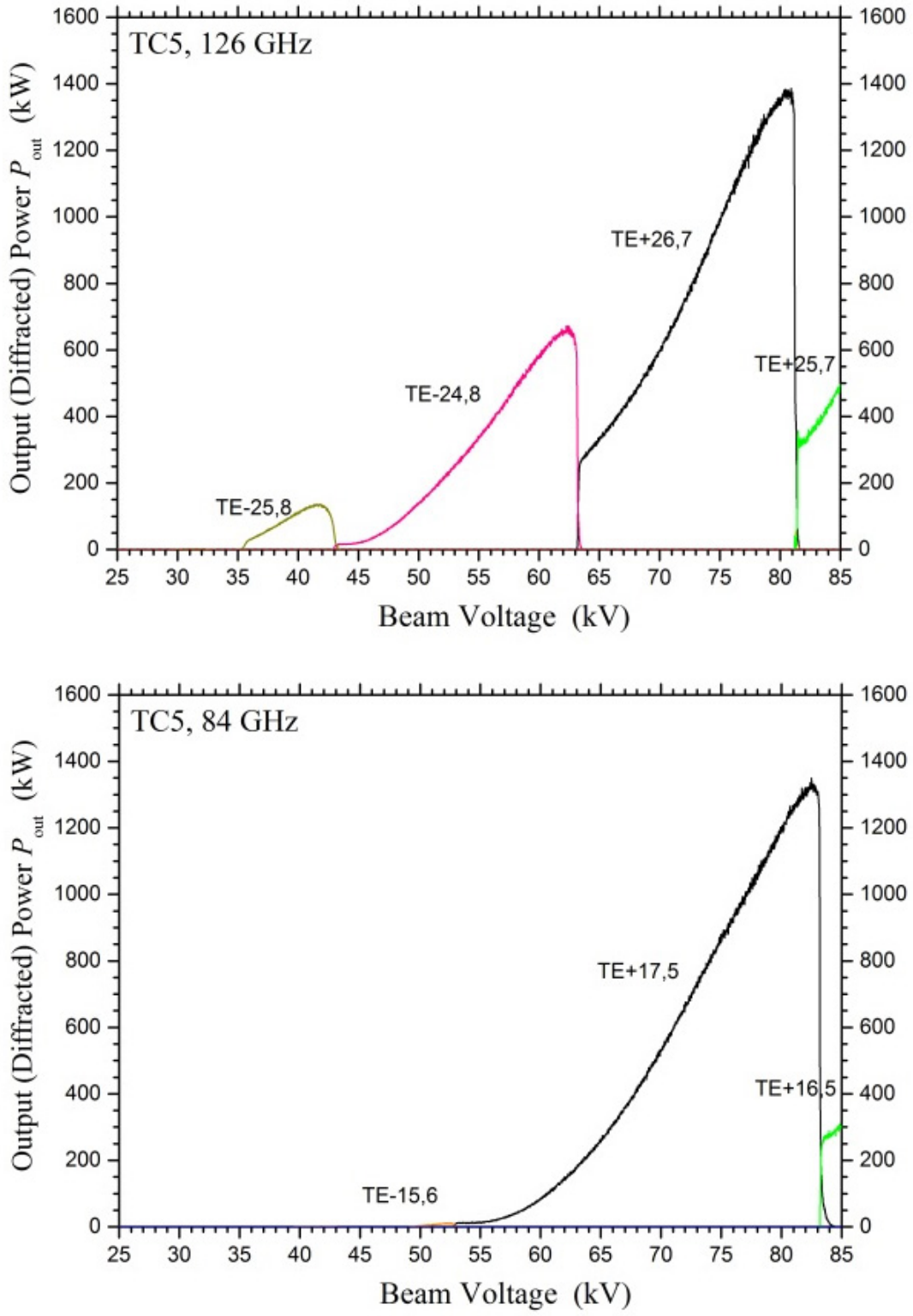

Fig. 1.8.1
Realistic multi-mode start-up simulations of the cavity design for the dual-frequency gyrotron for TCV upgrade. Top: High frequency (126 GHz) operation with the $TE_{26,7}$ mode (magnetic field 4.98 T). Bottom: Low frequency (84 GHz) operation with the $TE_{17,5}$ mode (magnetic field 3.31 T).

1.8.2 Gun design for the TCV 126 / 84 GHz 1 MW gyrotron

A triode MIG design has been developed for the TCV dual-frequency gyrotron. It satisfies all design criteria for the suppression of the trapped electrons. In addition, it ensures a high quality beam generation in both frequencies while the electric field limitations for stable voltage stand-off are also satisfied.

1.8.3 Improvements of the ESRAY beam optics code

For a typical simulation of the beam forming zone of gyrotrons the *ESRAY* beam optics code usually uses the fast, internal module *maggen* to calculate the magnetic field distribution generated by a set of solenoids. In this case a straightforward numerical integration of the Biot-Savart law is used. Unfortunately, this method has the drawback that effects caused by ferromagnetic materials (including permanent magnets) or eddy currents (caused by slow frequency collector sweeping) can not be taken into account. To handle also these effects, the freely available Finite Element Method Magnetics (*FEMM*) tool has been already used to simulate several problems in the past, especially those connected to longitudinal collector sweeping. The latest version of *ESRAY* now includes a much better integration of *FEMM* in the *maggen* module. For example, it is now possible to specify the shape and properties of metallic structures or permanent magnets and the geometries of coils directly in the *maggen* input file. This makes the workflow of the beam optics simulation much more efficient and less error-prone. In addition, the new concept also allows integrating the *FEMM* calculation step in the parallel *ESRAY* parameter sweep utility, which helps to reduce the overall simulation time significantly.

A design study of a permanent magnet system for a proposed 24 GHz industrial gyrotron is ongoing at the moment, based on the new possibilities implemented in the *ESRAY* beam optics code.

1.8.4 Gun Design Theory

A key parameter for the gyrotron operation and efficiency is the presence of trapped electrons. Two electron trapping mechanisms can take place in gyrotrons: (i) the adiabatic trap, and (ii) the magnetic potential well. Two gun design criteria were proposed for the suppression of both mechanisms in order to minimize the risk of possible problems. Experimental results of three high power gyrotrons were analysed in relation to the proposed design criteria. The extended analytical study has been accepted for publication in Physics of Plasma.

1.8.5 Ariadne Code Package Upgrades

In order to simulate the MDC geometry with our in-house code-package Ariadne, several upgrades and improvements have been performed which are listed below:

- A wider variety of geometries is compatible (including the proposed collector design) with the code possibilities
- Simplification of the geometry introduction
- Script language upgraded
- Fast localisation of the beam electrons in the mesh which significantly accelerates the calculations of the particle dynamics

In addition, the possibility of 3D simulation of cylindrical geometries (without the presence of the coaxial insert) has been incorporated in the Ariadne code facilities. Using this possibility non-uniform emission studies were performed on the EU cylindrical cavity gyrotron for ITER.

Involved Staff:

KIT/IHM: K. Avramidis, J. Franck, M. Fuchs, Dr. G. Gantenbein, Dr. H. Hunger, Dr. S. Illy, Prof. J. Jelonnek, Dr. J. Jin, Th. Kobarg, R. Lang, W. Leonhardt, M. Losert, D. Mellein, A. Meier (KIT, IAM-AWP), Dr. I. Pagonakis, A. Papenfuß, K. Parth, S. Ruess (KIT CS), Dr. T. Rzesnicki, Dr. A. Samartsev, Prof. Dr. Theo A. Scherer (KIT, IAM-AWP), Dr. A. Schlaich (KIT CS), M. Schmid, W. Spiess, Dr. D. Strauss (KIT, IAW-AWP), Prof. M. Thumm, S. Wadle, J. Weggen, Ch. Wu, J. Zhang, IGVP (University of Stuttgart): Dr. W. Kasparek, Dr. C. Lechte, R. Munk, Dr. B. Plaum, F. Remppel, H. Röhlinger, B. Roth, K.H. Schlüter, S. Wolf, A. Zeitler, IPP (Greifswald/Garching): B. Berndt, Dr. H. Braune, Dr. V. Erckmann (PMW), F. Hollmann, L. Jonitz, Dr. H. Laqua, Dr. S. Marsen, F. Noke, M. Preynas, F. Purps, A. Reintrog, T. Schulz, T. Stange, P. Uhren, M. Weißgerber

2. HGF Program: Energy, Topic Renewable Energy

2.1 Overview

This year's focus was laid on application-oriented R&D for high mass-flow PEF-treatment of microalgae. It could be shown, that PEF treatment with long pulses (≥50µs) can result in precipitation of biomass on cross linear treatment chambers' anodes. Biomass precipitation is considerably lower if pulses of 10 µs and shorter are applied.

ROS-signaling was identified to play an important role in nanosecond PEF-induced stress responses in plant cells.

Patch-clamp measurements provided new insights in membrane permeabilization mechanisms. A memory effect could be observed by membrane conductance measurements during the application of pulse trains.

2.1.1 Algae precipitation on electrode surfaces during Pulsed Electric Field (PEF) treatment

PEF treatment of microalgae has been demonstrated to exhibit processing advantages compared to conventional processing. To minimize processing energy demand, the treatment of pre-concentrated microalgae suspensions is advantageous. For concentrated suspensions at elevated biomass density (biomass density of approximately 80 g of dry weight per liter), microalgae precipitation on the electrodes of cross-linear treatment chambers was observed (Fig. 2.1.1). An interrelation between pH and zeta potential on the one hand and the amount of precipitated microalgae on the electrodes on the other hand is emerging. Impact of electric pulse parameters and pH was investigated and suggest that precipitation is caused by electrophoretic forces. The results indicate that shorter pulses can be used to reduce the parasitic precipitation.

Fig. 2.1.1
Illustration of the precipitation of the algae on the electrodes. Photos of the electrode were taken before processing PEF-processing of algae (left), just after processing (center) and after an additional drying step (right). The pictures illustrate the typical precipitation of algae after PEF-processing of 250 mL of a concentrated microalgae-suspension (*A. protothecoides)*.

2.1.1.1 Electrode-specific precipitation

In order to investigate the relationship between the observed precipitation and the applied process parameters, the two microalgae strains, *Auxenochlorella protothecoides* (*A. protothecoides*) and *Chlorella vulgaris* (*C. vulgaris*) were treated with a wide range of different treatment parameter. Specific energies from

W_{spec} = 50 kJ/kg up to W_{spec} = 100 kJ/kg, electric field intensities from E = 5-25 kV/cm and rectangular pulses of t_{Imp} = 10-200 µs width were utilized. Experiments were conducted with flow-rates between Q=0.1mL/s and Q=0.2mL/s. Throughout all experiments the observed microalgae precipitation occurred predominantly on the anode surface (Fig. 2.1.2). Precipitation on the cathode was not of relevance.

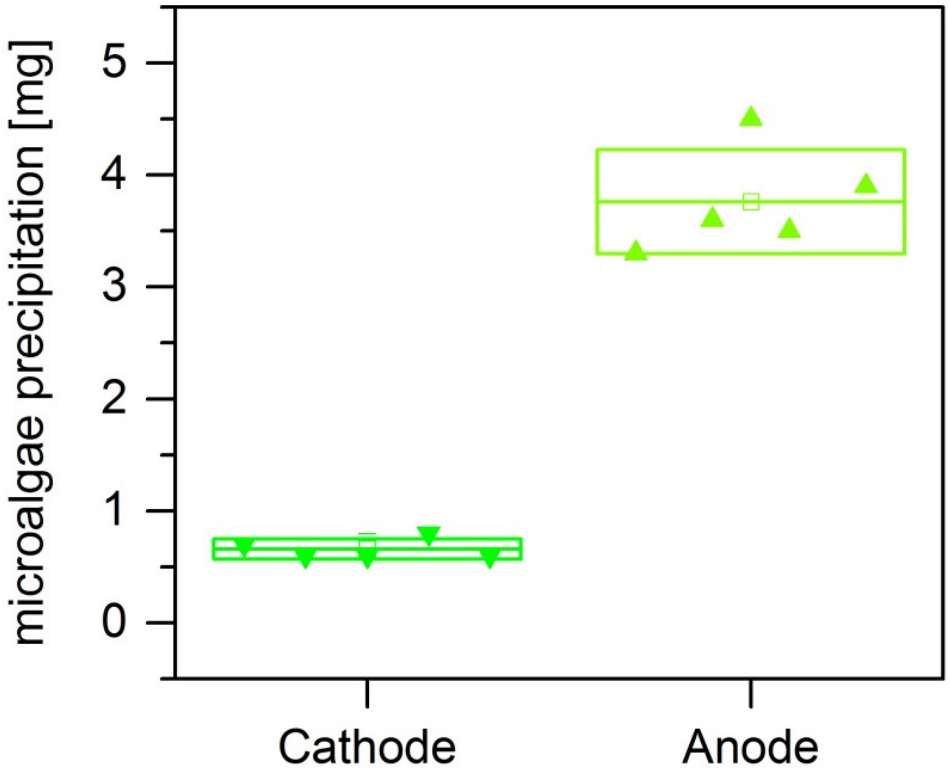

Fig. 2.1.2
Reproducibility of the precipitation of microalgae on the electrodes. The diagram displays the results of five experiments performed with the same cultivation batch of *C. vulgaris*. For each experiment, 75 mL of algae were treated with 50 µs-pulses and an electric-field magnitude of 5 kV/cm. Specific energy was adjusted at 50 kJ/kg and the flow of the suspension through the treatment chamber at 0.10 mL/s. Boxes show the average ± SD (standard deviation) and markers, the individual data-points.

2.1.1.2 Influence of pulse parameters on microalgae precipitation

The results showed only marginal precipitation on the electrode surfaces when applying 10 µs-pulses, while a significant increase of precipitation could be observed with longer pulses of 50 µs- and 200 µs pulse duration (Fig. 2.1.3). This knowledge can be helpful in applications, where short pulses are sufficient and precipitation need to be avoided.

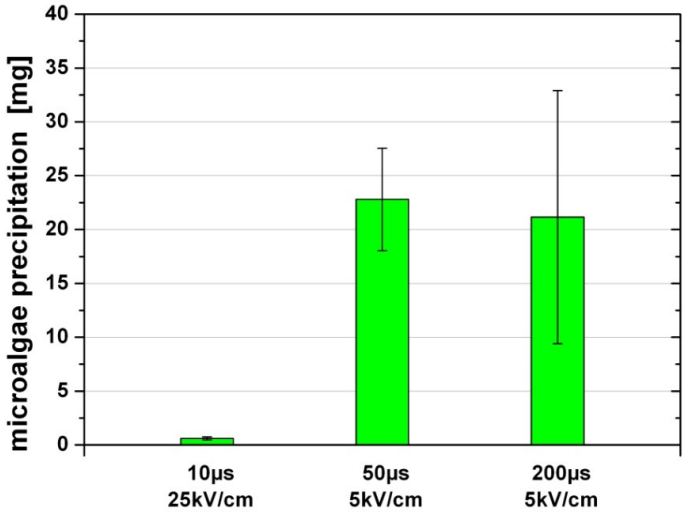

Fig. 2.1.3
Influence of pulse duration on microalgae precipitation (*A. protothecoides*). Specific energy was kept constant at 50 kJ/kg for all tested pulse parameters. Flow of the suspension through the treatment chamber was Q=0.10 mL/s.

In summary it can be said, that shorter pulses with a duration of e.g. t_{Imp}=10 µs causes only negligible precipitation, while longer pulses with a duration of t_{Imp}=50 µs and 200 µs effect considerable precipitation on the electrode surfaces. To avoid treatment chamber clogging, we take advantage of this finding and preferably apply pulse protocols with short pulse duration, if appropriate. The fact, that microalgae favor the anode side for precipitation, suggests that microalgae cells carry a negative net charge as commonly represented by their zeta potential value. The correlation between zeta potential and precipitated biomass will be subject of future investigations.

2.1.2 Stimulation of algae and plant growth by nanosecond pulsed electric field (nsPEF) treatment

No doubt, microalgae biomass is a valuable feedstock for high-yield production of lipids, proteins, antioxidants and other fine chemicals. Algae cultivation doesn't compete with food production, recycles CO_2, and can be done on barren lands. From the economic point of view one major future challenge is the reduction of production costs for algal biomass. This either can be achieved by reducing investment and operational costs of photobioreactors and/or by increasing the microalgae biomass yield. In a previous study, supported by the Baden Württemberg Foundation, it was shown that nsPEF treatment in combination with Auxin admixture induced accelerated growth of the microalgae *Chlamydomonas reinhardtii*, resulting in an increased biomass yield on the order of 10-20 %, compared to untreated samples.

Nevertheless, the magnitude of yield increase obtained with microalgae after nsPEF treatment is considerably lower than observed with C4-plants. It has been demonstrated, that the growth of seedlings of *Arabidopsis thaliana* increases by a factor of 2.5 (250 %) after nsPEF treatment. To clarify this contradiction, basic investigations on signaling pathways for nsPEF induced stress reactions of microalgae have been started in collaboration with the molecular cell biology division of the botanical institute at KIT.

In general, the plant molecular responses responds to abiotic stress, i.e. nutrient deficiency, heat, cold, light, salt, involve interactions and crosstalk with many molecular pathways, as indicated in Fig. 2.1.4 for *Arabidopsis thaliana*.

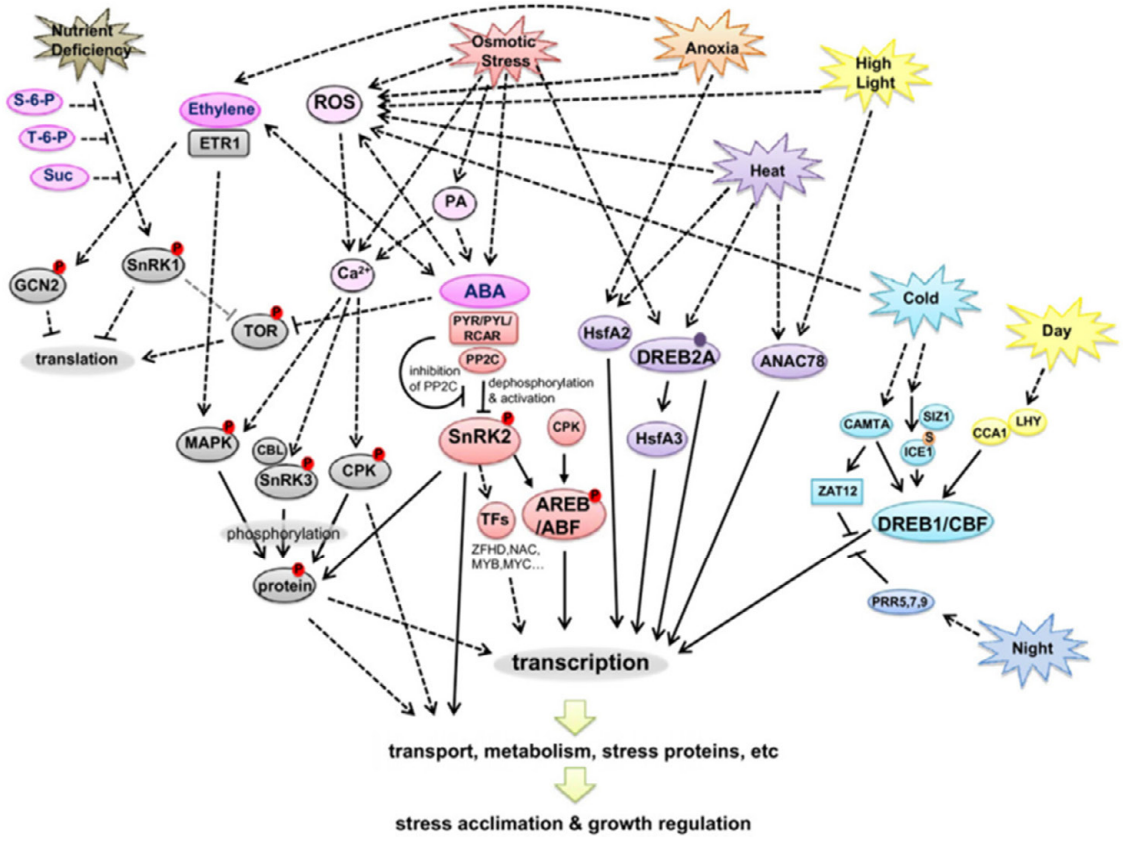

Fig. 2.1.4
A simplified working model of a signaling network of plant responses to abiotic stress [adopted from Cramer et al. BMC Plant Biology 2011, 11:163]

Besides Ca^{++} emission from mitochondria which is evident to be caused by nsPEFs and well described in literature, reactive oxygen species (ROS) also play a major role in stress response signaling pathways of plant cells, Fig. 1. One of the earliest signals in many abiotic stresses involve ROS and reactive nitrogen species (RNS), which modify enzyme activity and gene regulation. Also phospolipid oxidation involving PEF-induced ROS generation is suspected to play a role in membrane permeabilization, see next chapter. To check the ROS response after nsPEF treatment, cell suspensions of the microalgae *Clamydomonas rheinhardtii* were tested by Malondialdehyde (MDA) detection. MDA and lipid peroxide is generated by ROS-impact on unsaturated fatty acids. In combination with thiobarbituric acid MDA reacts to thiobarbituric acid reactive substances (TBARS). The TBARS concentration can be determined spectrophotometrically and gives direct feedback on nsPEF induced ROS concentration.

First experiments have shown, that MDA concentration, representing ROS generation, increases within minutes up to 2 hours after nsPEF treatment in suspensions of *C. reinhardtii*. After 2 hours the MDA signal went back to control values and increased again after three days. In summary, a fast response after nsPEF administration (short-term response) and a delayed response 3 days after nsPEF treatment (long-term response) clearly could be identified. The fast response, in terms of ROS generation, correlates well with

the increased cell diameter and optical density (OD). The cell swelling was larger for higher treatment energy and lasts for 2 hours. The performed treatment was non-lethal as indicated by staining the cells with Evans blue. Only a pure membrane selective permeability, due to the PEF treatment, was detected, which recovers quickly within seconds to minutes in dependence of the energy input. On long term following events could be observed: Inhibited cell division or delayed cell cycle and increased cell elongation. Microscopic analysis reveled that non-lethal nsPEF treatment induced a prolonged stage of telophase and cytokinesis of cell division, which clearly correlates with the oxidative burst observed 3 days after treatment.

Future work will focus on the role of the integral membrane protein RboH (respiratory burst oxidase homologs - to NADPH oxidases) which also is involved in natural ROS signaling in plant cells. The hypotheses to be followed are: 1) ROS are directly generated by the high electric field intensity across the cell membrane and 2) RboH generates ROS as signal molecule in response to abiotic stress (plant defense).

2.1.3 Studying membrane permeabilization of DC-3F cells with the patch clamp technique: Voltage pulse trains of positive or negative polarity reveal a memory effect

Previous experiments (see Annual Report 2014 and Wegner et al. 2015) had provided strong evidence that (at least) two separate processes are underlying electroporation at the molecular level in DC-3F cells, a cell line derived from lungs of Chinese hamster: A ‘transient electroporation’ that is probably associated with a physical interaction of the electrical field with the membrane bilayer, and a ‘persistent electropermeabilisation’ that may reflect a field-induced oxidation of lipids. The former is reversible within tens of milliseconds, whereas the latter prevails for minutes. Both could be separated by repetitively applying voltage pulses of 5-10 ms length and moderate amplitude. This type of pulse would elicit transient electroporation in a reproducible manner from the first pulse onwards (as indicated by the current response recorded on the cell while being clamped in the ‘whole cell” configuration’, reflecting membrane electrical properties) whereas a series of several pulses (usually three or more) would be required to induce the persistent electropermeabilisation. Hence, the cellular response to this pulse protocol depended strongly on the “pre-treatment history”. This effect deserved further attention.

For a more detailed study of this memory effect, a so-called double-pulse protocol was employed (Fig. 2.1.5 AB, top). The membrane was repetitively depolarized to the same clamped voltage (ranging from +280 to +360 mV among different cells; n = 8). Pulse length was 10 ms; after each pulse, the clamped voltage was lowered to 80 mV for 25 or 100 ms, before it was returned to zero mV and kept at this value for 5 s. The last voltage step and the respective current response (arrows in the enlarged details of the current traces) were used to calculate the membrane resistance in the intermediate voltage range, which served as a measure to quantify persistent electropermeabilization.

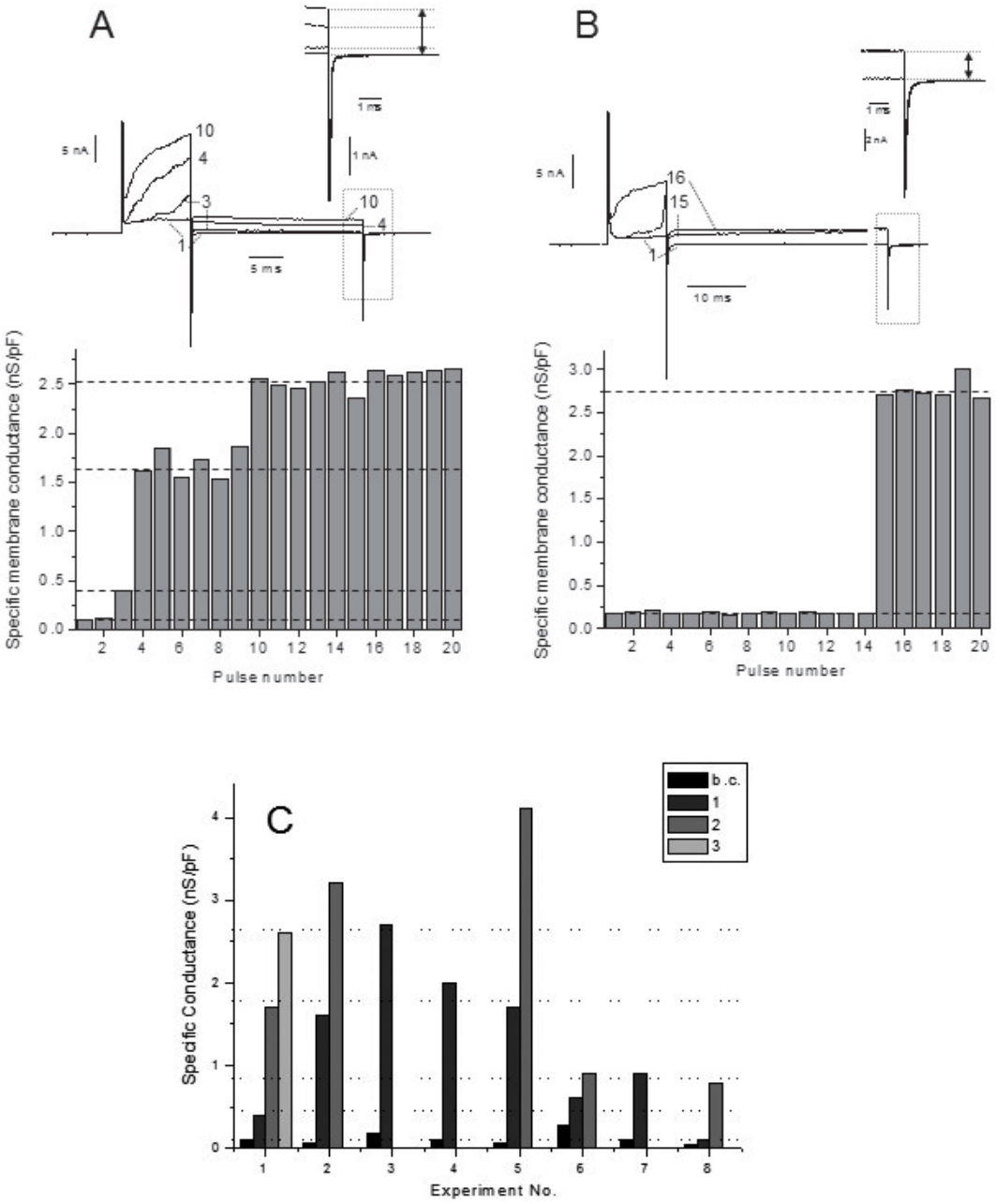

Fig. 2.1.5

Two examples of the current response to repetitive application of a double-pulse protocol, consisting of a depolarization to 320 mV command voltage for 10 ms, followed by a clamp at 80 mV for 25 (A, top) or 100 ms (B, top; note that part of the trace was omitted). Subsequently, the membrane was stepped back to 0 mV for 5 s before the next pulse of the same type was applied. Individual repetitions are superimposed as indicated by numbers. The membrane conductance at the physiological voltage range was calculated from the difference in steady state current level induced by a voltage step from 80 to 0 mV (re-drawn at an enlarged scale in A and B, arrows). For both experiments, conductance levels for the sequence of pulses applied in A and B were plotted at the lower panels of the figures. Note conductance increase (dotted lines) in several steps (A; see pulse 3, 4 and 10) or just one step (B; pulse 15). In C, data for 8 experiments carried out in the same way are summarized. Cells No. 1 and 3 correspond to the experiments shown in Figs A and B, respectively; in the other experiments, the same protocol as in Fig, B was employed. Apparently, the distribution of conductances normalized to cell capacitance were non-gaussian but reflected preferred conductance states of the membrane (dotted lines; b.c., background conductance).

Results for two representative examples are depicted here. In the experiment shown in Fig. 2.1.5 A, the conductance increased stepwise at the third, fourth and tenth pulse, respectively, whereas in B it was a one-step change (at pulse 15). In 8 independent experiments, up to 3 levels of elevated conductance could be identified in addition to the background level (shown in Fig. 2.1.5, C), indicating that distinct degrees of persistent permeabilization could be discerned. Note that conductance changes did not reflect a deterioration of the seal, but resulted from a general increase in membrane permeability as verified by monitoring uptake of the fluorescent dye propidium iodide (not shown here; see Wegner et al. 2015). A plausible explanation for the pronounced 'memory effect' is that a change in membrane properties, most likely of a chemical nature (e.g. lipid oxidation), is induced by the administration of an electric field pulse. This modification is not (fully) reversible during the interpulse period and tends to accumulate until a threshold is reached that leads to a stepwise or gradual increase in membrane conductance over the whole voltage range.

Interestingly, when the same type of experiment was repeated, but the cell was hyperpolarized instead of being depolarized, changes in membrane conductance within a train of 20 pulses appeared to be more gradual (not shown). No transition between distinct conductance levels was observed, indicating some asymmetrical polarity in this process for which there was no obvious explanation.

Involved Staff:

H. Brüsemeister, J. Fleig, Dr. W. Frey, Dr. C. Gusbeth, D. Herzog, M. Hochberg, S. Keipert, K. Leber, Prof. G. Müller, K. Paulus, D. Quattrocchi, Frau S. Rocke, Dr. M. Sack, Frau Dr. A. Silve, DI R. Sträßner, R. Wüstner

2.2 Conditioning of Biomass by Pulsed Power Techniques

2.2.1 Modules for a Semiconductor-based Pulse Generator for Food Preparation

The permeabilization of the cell membranes by application of pulsed electric fields (PEF) to biological tissue can be used as an alternative way for food preparation instead of thermal treatment. For this application a semiconductor-based pulse generator is currently being developed. The pulse generator consists of modules comprising IGBT switches, pulse capacitors, and control circuitry. Fig. 2.2.1 shows one module.

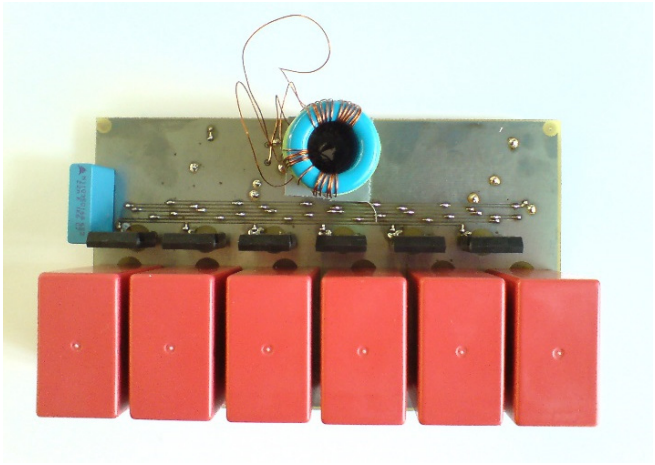

Fig. 2.2.1
One module of the pulse generator.

Each module has been designed for a charging voltage up to 1 kV. The IGBT switch has been set up using six inexpensive single IGBTs in parallel connection. The modules are stacked to form a Marx configuration. So far, a stack of ten modules has been set up (Fig. 2.2.2). The charging path is formed by common-mode chokes. All modules are switched on synchronously. The switching signal is transferred to the stages inductively. Fig. 2.2.3 shows voltage and current at a combined resistive and inductive load when operating a stack of ten modules at a charging voltage of 1 kV per stage. The inductivity of the load circuit in combination with comparably fast switching enables an energy-efficient soft turn-on condition. The inteded application allows for a complete discharge of the capacitors. Hence, the switches open in a zero-current condition after the pulse.

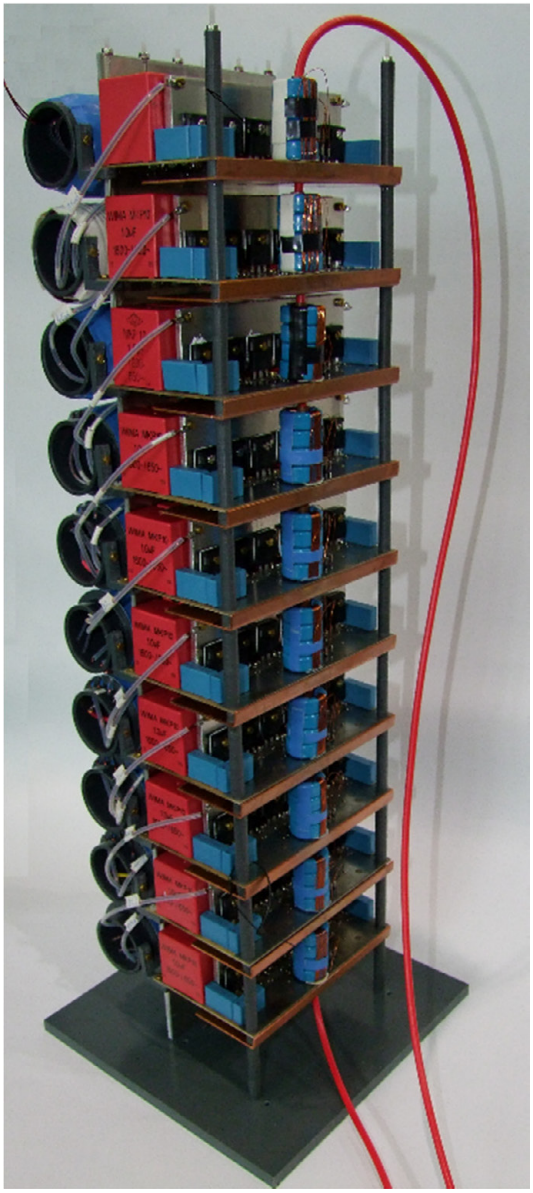

Fig. 2.2.2
Pulse generator comprising ten modules.

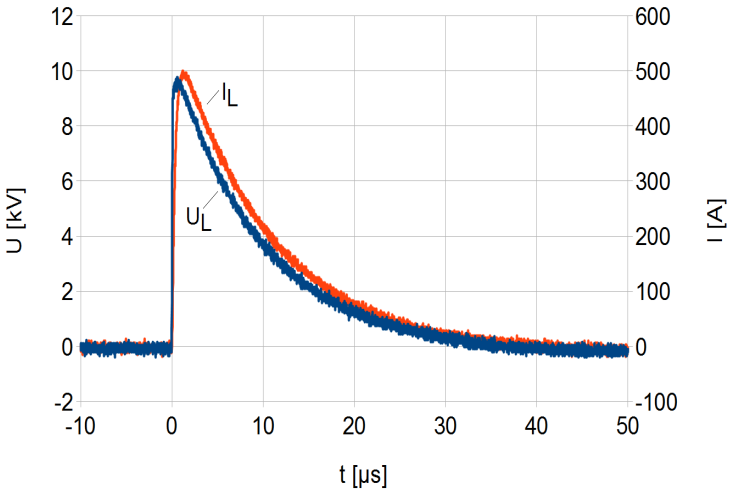

Fig. 2.2.3
Voltage and current across a combined resistive and inductive load when operating a 10-stage generator at 1 kV charging voltage per stage.

2.2.2 Gate Boosting Circuit for IGBT Devices

Rise and fall time of current and voltage across an IGBT determine the switching losses under hard switching conditions typical for many pulsed-power applications. Due to parasitic inductances in the gate drive circuit and the device leads, gate charging is delayed and hence switching speed is limited. A simple gate-boosting circuit comprising a peaking capacitor allows for fast charging of the gate and, hence, faster turn-on and turn-off of the device. The gate driver has been designed such, that during switching an over-voltage pulse is applied to the gate terminals of the package, whereas the voltage across the internal gate structure of the IGBT does not exceed the limits according to the device specifications. Fig. 2.2.4 and Fig. 2.2.5 show the collector current of an IGBT depending on the driver voltage and the normalized loss energy for each curve, respectively. Under hard switching conditions at a collector current of 80 % of the maximum rated pulse current, reduction of turn-on speed and turn-on losses in the order of 90 % could be achieved.

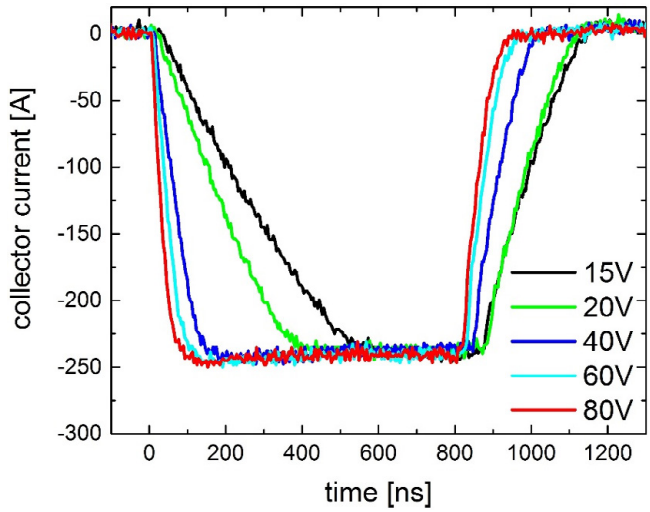

Fig. 2.2.4
Pulse current of 80 % maximum rated pulse current for different driver voltages.

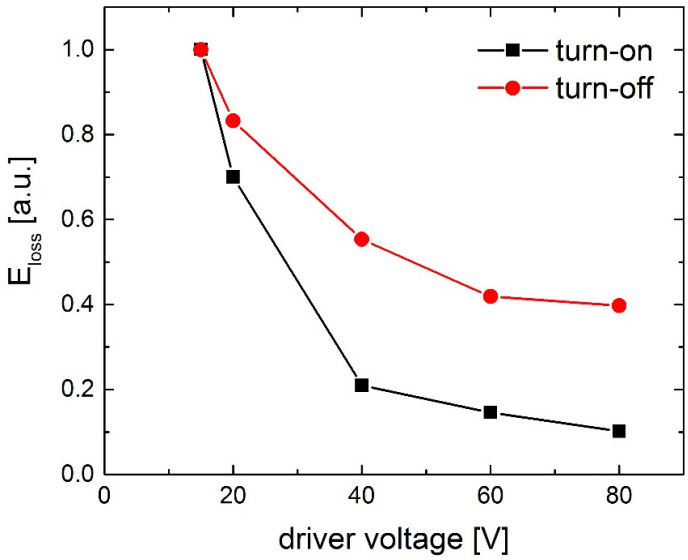

Fig. 2.2.5
Normalized loss energy for each curve according to.

Involved Staff:

J. Fleig, D. Herzog, M. Hochberg, S. Keipert, Dr. M. Sack.

2.3 35.12.02 – Concentrating solar power (CSP)/ Liquid metal – Material research – improving the compatibility of materials for CSP

The use of liquid metals as heat-transfer- and storage media is a new research area started in the frame of POF3 together with IKET, INR and IAM. The basis of this work including experimental capabilities is funded on the experience and expertise gained in the last years on research performed in the nuclear program. Based on fundamental aspects of material liquid metal compatibility material concepts and related experimental are the major target of our research. Surface modification of materials using pulsed electron beams is well established in the nuclear community dealing with the use of liquid metal coolants. In-situ diagnostics of beam formation and target beam interaction will be targeted combining a new constructed GESA – SOFIE and simulations using MAGIC and other software tools.

2.3.1 Development of material concepts for the use of liquid metals at high temperatures

2.3.1a CO_2 free Methane cracking in liquid Sn

In the period of 1.12.2012-31.05.2015 a joint project between the IASS (Institute for Advanced Sustainability Studies e.V) and the KIT was carried out with the final aim to develop an experimental reactor for continuous hydrogen production by thermal decomposition of methane in liquid metals. On KIT side three institute participated: IKET, IHM and IAM. The work of the IHM at this project can be divided in three topics:

1. Test related analysis and studies
    - Examination of the produced solid carbon
    - Investigation of the catalytic effect of Sn or the produced carbon
2. Selection and test of possible structural material for a reactor
3. Screening test for the selection of most suitable catalyst materials for a downstream fixed bed section

Detailed descriptions of the related work was given in previous annual reports. Therefore, a final short summary after the end of the project is given here.

Hydrogen is one of the promising energy carriers of the future. Up to now 96 % of the world wide hydrogen production is based on fossils, with a high amount of CO_2 emissions. Therefore, several CO_2 free hydrogen production processes are under development. A medium term solution can be Methane cracking or Methane decarburation. This process is based on splitting the Methane molecule into its atomic components, hydrogen and carbon. To avoid blocking of methane cracking facilities by the formed solid carbon liquid metals might be a good option as heat transfer medium. Carbon can swim up to the surface of the liquid metal due to the density difference, from where it can be removed. In the past, the principal feasibility of this process has been shown using lead (Pb) or tin (Sn) as heat transfer medium. However, at the desired temperatures (up to 950°C) the liquid metals contribute significantly to the corrosion of the reactor materials due to the high solubility of the steel.

Topic 1:

A quartz glass-steel bubble column reactor filled with liquid tin was used for the experiments. Cylindrical quartz glass rings served as a packed bed. Tests were conducted with liquid metal temperatures between 930°C and 1175°C. The majority of the produced carbon accumulates as expected at the surface of the liquid metal. Only a small proportion was transported with the off gas stream to the filters installed. In the liquid metal basically no carbon was found only a thin carbon layer of about 10µm was deposit on the inner surface of the quartz tube. Surface area, geometry and size of particles of the produced carbon are quite similar in all experiments. The carbon above the liquid metal appears as flake shaped agglomerations in the size range of 1.5 µm to 24 µm consisting of single particles with sizes between 40 nm and 214 nm, having most likely spherical shape. The specific surface area of the carbon, based on BET measurements, varied from 8-23 m^2/g (carbon above the liquid metal) to 40 m^2/g (carbon taken from gas outlet filter). After the baking of the powder for the BET measurement a slight yellow deposition on the quartz vessel appeared. This can be explained by hydrocarbons sticking on the carbon powder. Apart from that, the powder is highly pure, only minor traces of tin (0.70 wt%) were measured by EDX. The contamination of the carbon with tin in the gas part could have occurred from tin splashes off the surface during operation. But, more likely during the filling process in which liquid tin flows from the supply tank located above the reactor through the whole packed bed inventory. The analysed carbon seems to be not well crystallized, indicated by week XRD reflection pattern.

Neither the produced carbon powder nor the tin exhibit in several tests using thermogravimetry (TGA) with an attached mass spectrometer a clear catalytic effect.

Topic 2:

Long-term corrosion tests (up to 840h) were performed with different materials. The most promising material for the high temperature parts is graphite and for temperatures up to 559°C Mo can be considered. Based on the results of the material tests a proposal for a possible reactor design was made (Fig. 1 sketch of bottom part of the reactor). The gas inlet part requires lower temperatures to avoid an early cracking of methane, which can reulst in a blocking of the gas inlet; parts made of Mo can be employed. For the hot part an inner tube of graphite is proposed. To protect the graphite tube from an oxidizing atmosphere at high temperature an outer tube of an e.g. alumina forming alloy like FeCrAl will be considered.

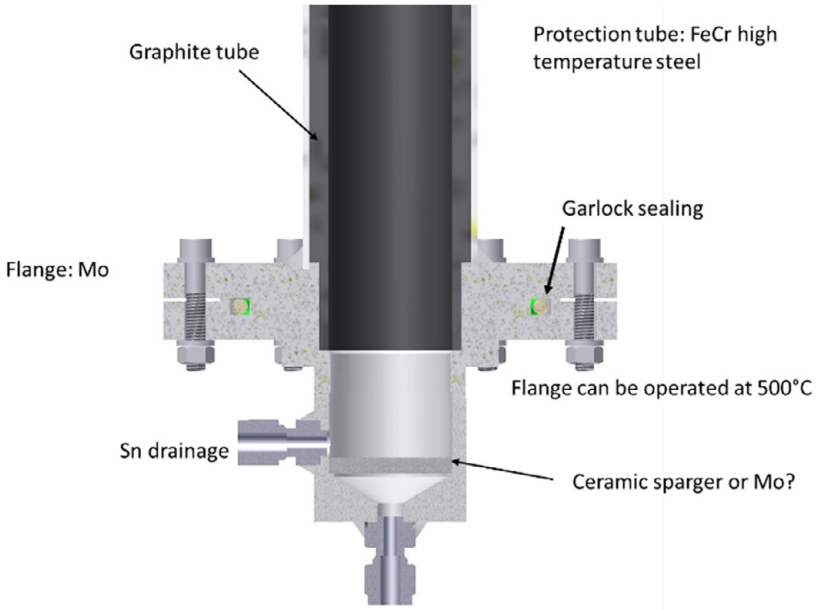

Fig. 2.3.1
Proposal for a possible reactor design.

Topic 3:

Tests on possible catalytic material for a second catalytic section for hydrogen have been performed using thermogravimetry (TGA) with an attached mass spectrometer. The tests revealed that Ni nano powder has the best catalytic effect: Ni_{nano}> $Ni_{smaler\ 45\mu m}$ > Ti_{nano} > BP2000. BP2000 is a carbon powder with a surface area of 1500m²/g. Almost no catalytic effect could be observed for Ag_{nano}, Pt_{nano} and Ru powder.

2.3.1b Design and construction of Na corrosion test facilities for CSP tower receivers

The most promising liquid metal to be employed as heat transfer media in CSP tower receivers is liquid Na. Na was already used in the past for this purpose, but some Na fire stopped all activities in that direction. Therefore, all materials that are intended to be used have to be fully compatible with Na and no stress induced failure is allowed. Most steels are corrosion resistant at least up to 650°C in oxygen free Na. For efficient use of CSP the final target is to operate the receiver at temperatures above 750°C. To assure the use of steels and Ni-based alloys and surface modified materials corrosion test in stagnant Na are envisaged. The day and night cycle and the occurrence of clouds induce stresses in the materials. Rapid temperature changes at high temperatures will be simulated by a dedicated test facility. Two temperature

ranges are considered to be of interest. For short term realization of Na as CSP heat transfer media HT-steels without and with surface engineering (alloying with non-soluble materials or Al including pre-oxidation) will be tested at temperatures below 700°C. For long term perspective higher temperatures up to T_{melt} of 883°C are the target. There Ni base alloys with and without surface engineering, Ceramics, Maxphases or new concepts like WCu-laminated tubes will be considered.

Compared to experiments performed with Pb alloys in the past Sn sodium requires significant improved safety measures that assure to avoid any contact of Na at high temperatures with water and air. Therefore, a new Na-Corrosion lab containing a COSTA-SOL for corrosion tests in stagnant Na at temperatures up to 880°C and a high temperature thermal cycling loop SOLTEC-TCT (700°C + 880°C) was established.

A dedicated COSTA facility the COSTA-SOL was designed. For safety and compatibility issues the quartz tube, which is employed in existing COSTA'S is replaced by a stainless steel tube. Oxygen free Na will be established by purging small amounts of ArH2 through the tube. The Na will be contained in Al_2O_3 crucibles placed on a steel tray that will be located in the stainless steel tube. The filling of the crucibles with Na and the exchange of samples cannot be done in similar way to the lead alloy experiments. To minimize any possible contact of Na at high temperatures with air or even moisture the furnace tube is attached to a glove box by welding. In the glove box, the Na can be melted and cleaned and filled into the crucibles. Specimens and Na will never be in hot stage handled out-side the glove box.

The entire high temperature thermal cycling loop SOLTEC-TCT consists of two parts; the loop and the thermal cycling test section. The loop part, which was designed by colleagues from INR, is now contracted to a construction company. The thermal cycling test section is designed and almost manufactured in the IHM workshop. The safety and operating systems are also designed and will be assembled.

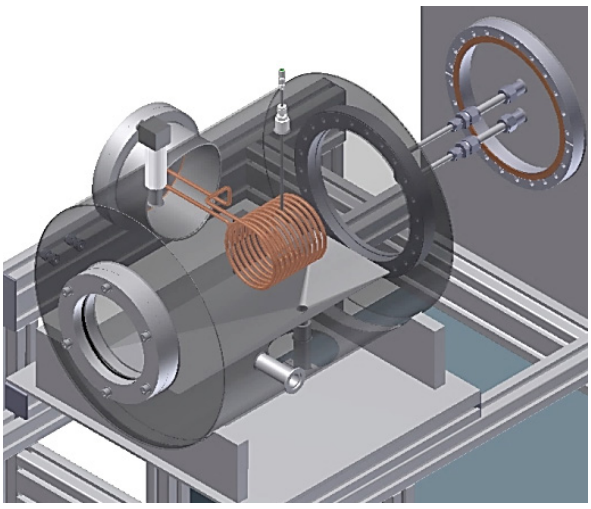

Thermal cycling test section

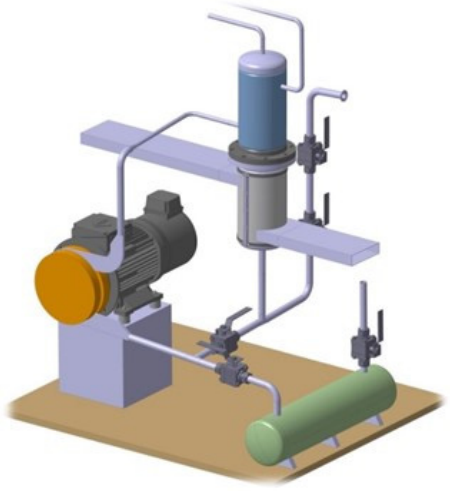

Loop part of SOLTEC-

Fig. 2.3.2
Sketch of SOLTEC-TCT loop and thermal cycling test section.

An inductive heater will be employed to heat the sample tube shape, which is placed in a vacuum vessel. The sample will have tube shape and will be attached to the outlet of the loop. During the experiments the hot Na leaving the loop with up to 700°C will flow through the tube sample and will be heated by the inductive heater. The oxygen and moisture content will be permanently surveyed and if required adjusted. A pressure sensor controls any pressure increase, which can be induced either by a leakage of the vacuum

vessel or by a rupture of the tube shaped specimen, and gives signal for fast draining of the loop and the shut down of all heaters.

2.3.2 GESA-SOFIE and related simulations

The concept of the new facility GESA-SOFIE is based on the approved operation principle of the facilities GESA I and GESA II. Many years of experience with the old accelerators as well as particle-in-cell code simulations (MAGIC3d and esray) were used to develop an optimized design for the new facility. The optimization concerned an improved adjustment of static electric field and magnetic field configurations, the possibility to tune shape and position of the electrodes, and an easy access for diagnostic tools to monitor the areas critical for operation. It is expected to obtain a stable operation of the facility over a wide range of impedances between cathode and grid as well as between grid and anode. In the cathode-grid gap, the impedance is influenced by the cathode emission behavior, while the impedance in the grid-anode gap is controlled by the field distribution.

The GESA-SOFIE facility consists of four functional components: Marx generator, pulse duration control unit, magnetic field configuration, electron accelerator.

The Marx generator has several stages connected in series, each consisting of a LC forming line. In order to keep the shock resistance as low as possible, the number of stages is limited to three. In spite of the compact design, operation of the generator is possible up to a charging voltage of 50 kV. Thus, the output voltage on a 1 kΩ load can reach 150 kV.

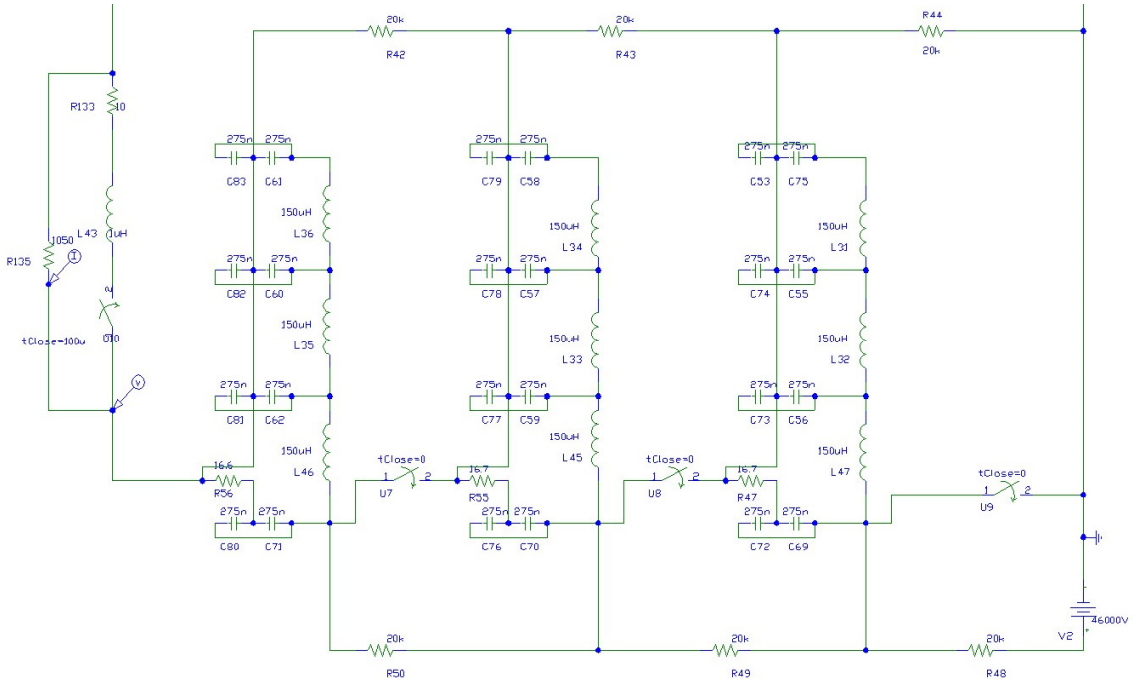

Fig. 2.3.3
PSpice model of the Marx generator of GESA-SOFIE.

The pulse duration control unit consists of two serial spark gaps. The distances of the electrodes and the gas pressure are adjusted such that the dielectric strength is slightly above the output voltage of the Marx generator. The control unit is triggered by a 120 kV pulse applied to the lower, near earth spark gap. For

generation of the trigger pulse the generator MiniMarx by Ion Physics Corporation is used. The control unit allows a reliable control of the pulse duration at a voltage decrease of up to 20 %. This corresponds to a pulse duration of more than 200 µs at a total load current of 200 A.

The magnetic field is generated by 5 coils. The optimum position, dimension, and number of turns were determined with the simulation software FEMM 4.2 under consideration of the eddy currents induced in the metallic parts of the accelerator. The coils are fed by a generator with output voltage up to 5 kV and capacity 2.8 mF.

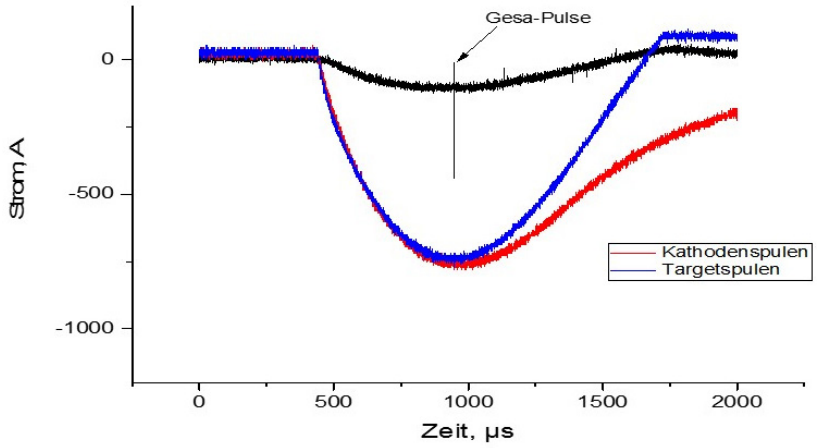

Fig. 2.3.4
Current evolution of the magnetic coils.

The maximum field strengths are 0.5 T at the target and 0.15 T at the cathode. Default settings at normal operation are 120 mT at the target and 20 mT at the cathode.

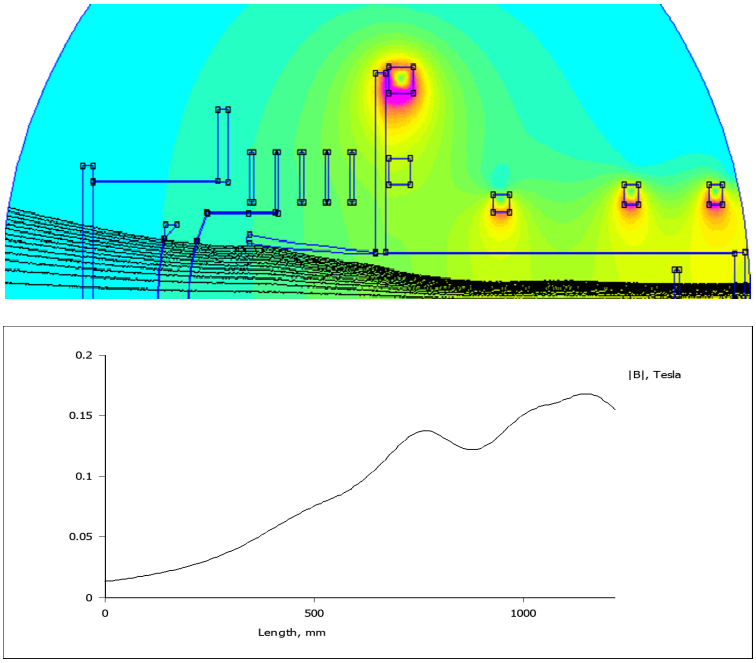

Fig. 2.3.5
FEMM 4.2 calculation of the magnetic field strength for a current of 800 A flowing through all coils.

The electron accelerator is of triode type with a controlling grid, as were GESA I and GESA II. The electron emission source consists of 300 carbon fiber bundles, which are connected to the cathode potential via 2 kΩ resistors. The resistors significantly contribute to the ignition behavior of the fiber bundles.

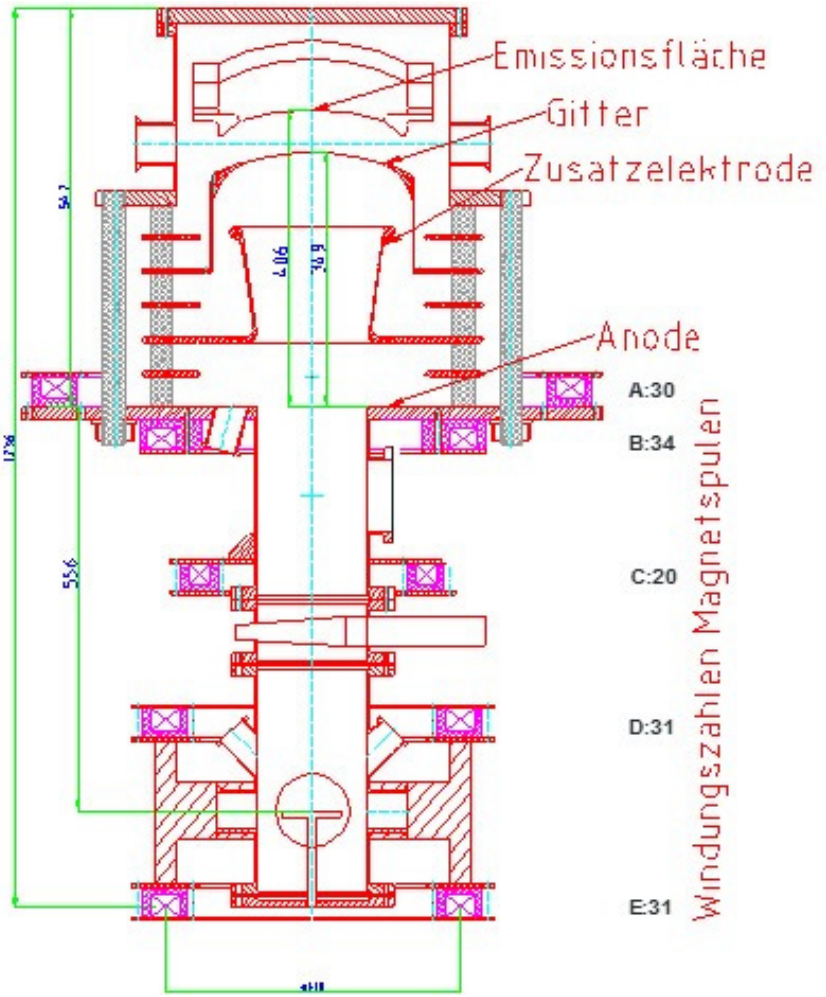

Fig. 2.3.6
Accelerator chamber of GESA-SOFIE.

The grid holder is specifically shaped such that the static electric field configuration in the region where the electron beam is compressed compensates space charge effects. For further improvement of electric and magnetic field distributions, an additional cone shaped electrode is provided. This electrode can be connected either to the anode potential or to a potential between grid and anode. Via the electric conductivity of the cone material the magnetic field distribution can be tuned locally.

For normal operation the vacuum is kept at 1.0-5.0x10^{-6} mbar.

The facility GESA-SOFIE including all units was put in full operation in April 2015. The typical difficulties specific to the startup phase of such a facility were encountered as expected: the cathode needed some conditioning. The startup phase was investigated in detail using fast framing imaging. Typical for this stage of operation is an excessive plasma generation at the cathode, which leads to an unstable current waveform and frequent short circuiting between cathode and grid.

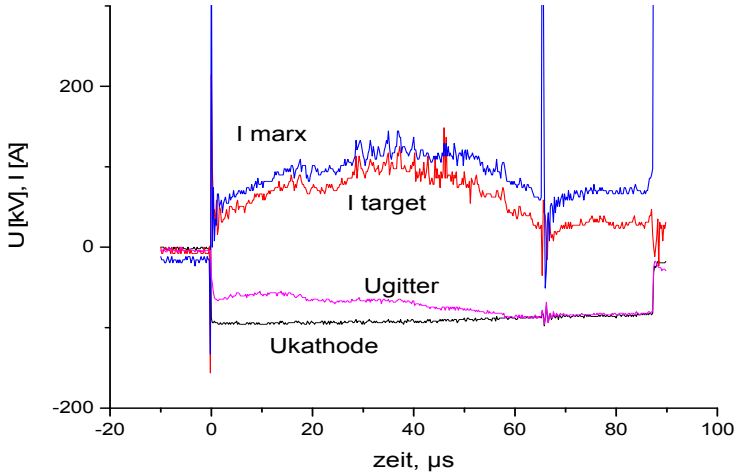

Fig. 2.3.7
Voltage and current waveforms of typical pulse during startup phase.

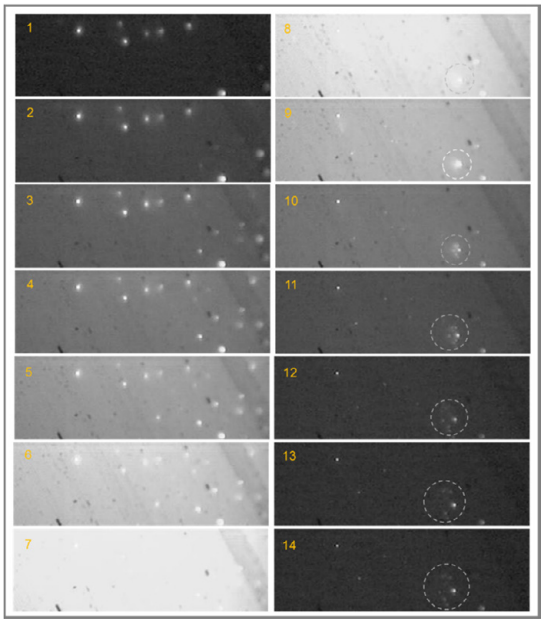

Fig. 2.3.8
Images of the cathode during emission, recorded with NAC HX-3-camera at a frame rate of 200000/s.

The images show a very inhomogeneous ignition pattern of the cathode. This might be explained by the larger contamination of the new carbon fiber bundles due to the higher adsorption capacity. Adsorbates are released during each pulse, which leads to subsequent cleaning and a more and more homogenous and stable ignition. Additionally, newly prepared fiber bundles are never perfect. A few fibers may stick out from the bundles and serve as preferred emission sources. These fibers will break off progressively due to thermal stresses (right images). It takes tens of pulses for the emission behavior to stabilize.

Typical voltage and current waveforms of a conditioned cathode are shown below, together with the corresponding streak image of the X-ray signal generated by the electron beam at the target.

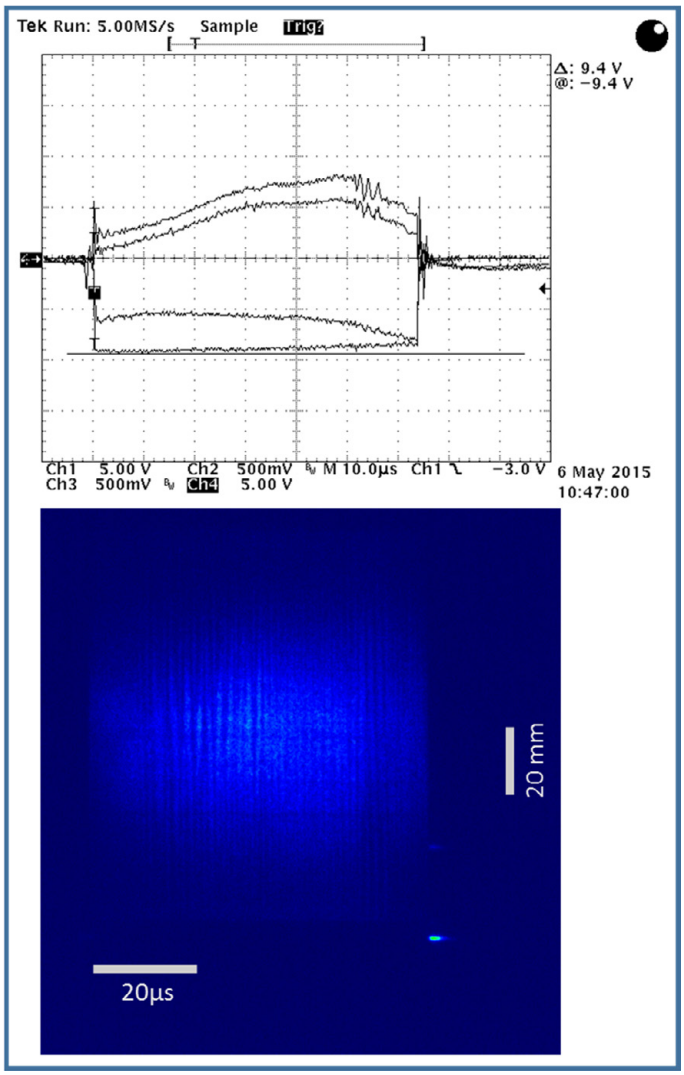

Fig. 2.3.9
Voltage and current waveforms and corresponding streak image of the beam profile. The cathode is conditioned.

Typical values of GESA-SOFIE operation with default voltage division and magnetic field configuration are:

cathode – anode voltage:	90-100 kV
cathode – grid voltage:	35-40 kV
total current:	150-180 A
target current:	100–120 A
pulse duration at max. 20 % voltage drop:	up to 200µs
pulse duration till breakdown of cathode – grid voltage:	70-80µs
beam diameter at target:	40 -50 mm

A parameter useful to find the optimum magnetic field distribution is the compression coefficient, defined as the ratio of B in the transport channel and B at the cathode, K=Bt/Bc.

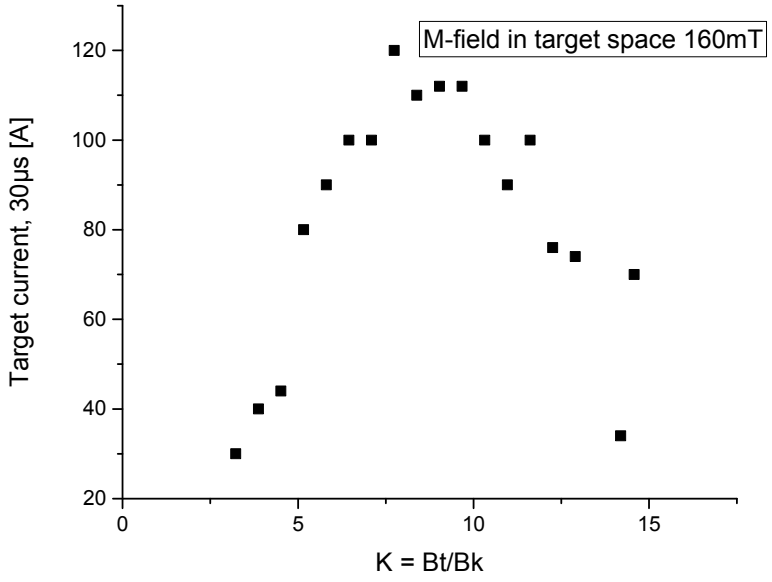

Fig. 2.3.10
Target current as a function of the compression coefficient. The magnetic field strength at the target was kept constant.

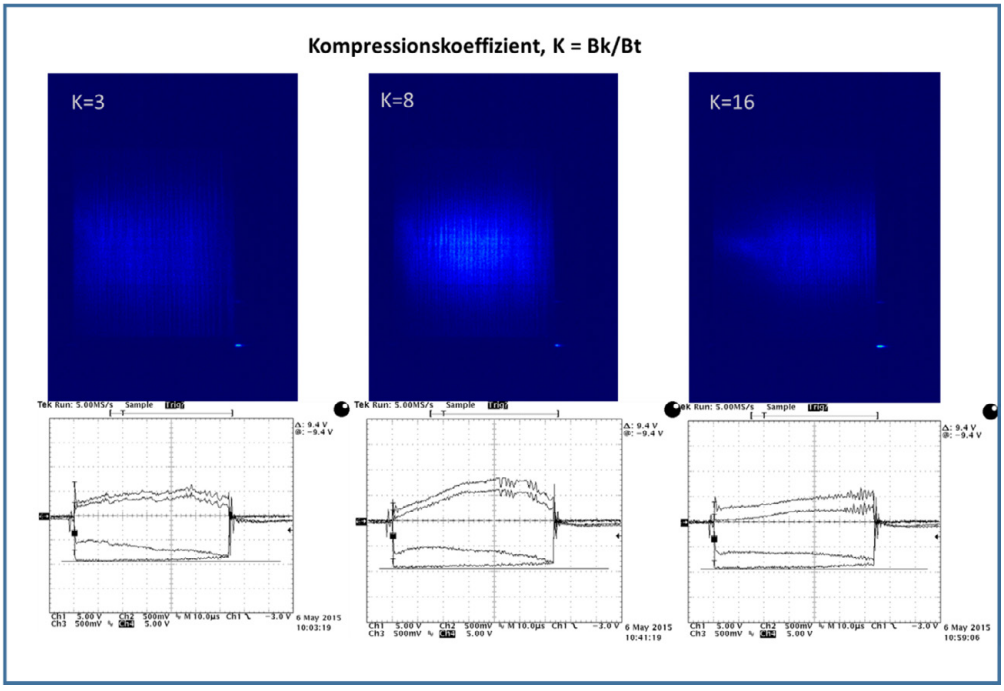

Fig. 2.3.11
Streak images of the beam profile and corresponding voltage and current waveforms for three different magnetic field distributions, characterized by their compression coefficient K.

A strong magnetic field at the emission area influences the plasma generation and dynamics at the cathode. As a consequence, the impedance of the cathode-grid gap is unstable. At a higher value of the compression coefficient K, more electrons are reflected at the magnetic mirror at the entrance to the transport channel back towards to cathode. Thus, the impedance of the facility increases. An optimum was achieved for K~8.

The grid potential is a very important parameter to control the operation of GESA facilities. It allows the variation of the plasma generation intensity over a wide range. Depending on the electric field between cathode and grid, different stable operation regimes can be achieved. Related to the specific application, GESA-SOFIE can be operated either in a high-impedance regime with long pulse duration and moderate current or in a low-impedance regime with maximum current. The grid potential is controlled by the circuit connected to cathode, grid, and anode with low-inductive high-voltage resistors and capacitors. An interesting regime is found for the voltage divider having a total resistance similar to the accelerator impedance. In that case, the grid current has only minor influence on the grid potential and the acceleration voltage between cathode and grid can be kept constant for a rather long time. Thus, the target current data allow direct conclusions on the dynamics of the cathode plasma.

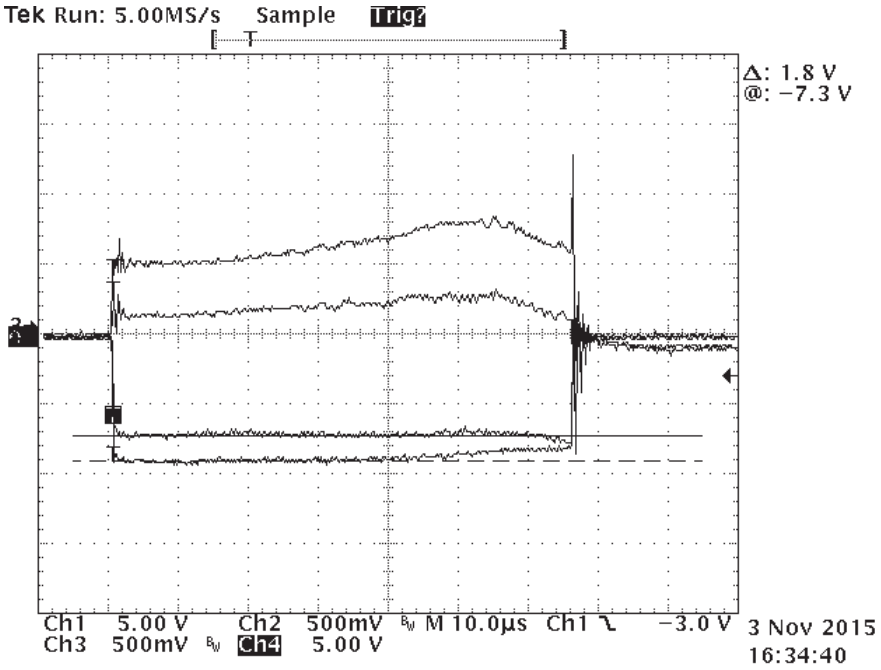

Fig. 2.3.12
Operation with constant cathode-grid voltage.

In the regime of low impedance between cathode and grid, a potential barrier builds up between grid and anode, which might reach the depth of a virtual cathode. The barrier leads to an increase of the total impedance of the facility. The problem was solved by introducing an additional electrode, which affects the static electric and magnetic fields locally. Shape and position of the electrode were optimized by means of simulations with the PIC code MAGIC3d. Although space was very limited, an additional cone-shaped electrode could be installed in GESA-SOFIE without affecting the dielectric strength too much. The dielectric strength was still high enough to ensure stable operation of GESA-SOFIE. As expected, a significant increase of the target current could be achieved by the introduction of the cone shaped electrode.

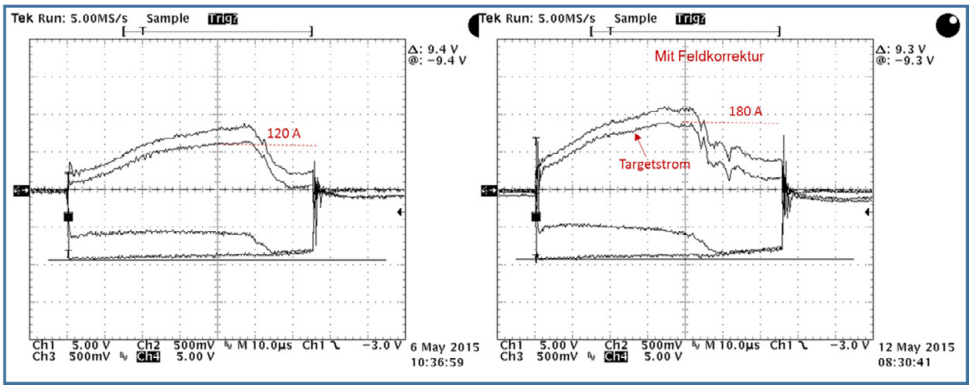

Fig. 2.3.13
Typical voltage and current waveforms for GESA-SOFIE without (left) and with (right) additional cone shaped electrode in the space between grid and anode.

In most situations where plasma is used as an emission source, its control is a huge challenge. The situation becomes even more complex if the accelerator is used in the regime of long pulse duration. At pulse durations comparable with the timescale of plasma dynamics, effects such as variation of the gap distance or of the plasma emissivity are crucial to the stability of the operation. GESA-SOFIE was developed in such a way that the emission source can be accessed by optical diagnostics. Using a fast framing camera NAC 3 ($2x10^5$ frames/s), the plasma behavior in the cathode-grid gap was investigated. The images give information about the ignition behavior of the cathode, plasma generation and plasma dynamics. Detailed analysis of the experiment data will be done in the future.

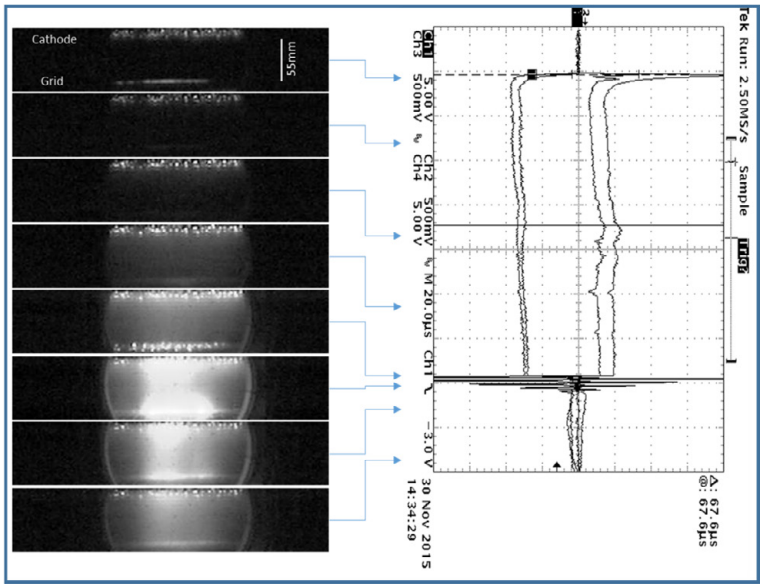

Fig. 2.3.14
Micrographs of the gap between cathode and grid. The specific time of each snapshot is indicated in the corresponding oscillogram on the right.

Involved Staff:

DP W. An, A. Neukirch, Dr. A. Heinzel, DI (Fh) F. Lang, Prof. G. Müller, Dr. G. Schumacher (Gast), A. Sivkovich, Dr. A. Weisenburger, DI (Fh) F. Zimmermann

3. HGF Program NUSAFE: Safety Research for Nuclear Reactors

3.1 32-24-03 Transmutation – Liquid Metal Technology

Materials and oxygen transport and control in heavy liquid metal cooled subcritical systems (MYRRHA).

Long-living high-level radioactive waste from existing nuclear power reactors should be transmuted in short-living radio nuclides using fast neutrons provided by a spallation target in an accelerator driven subcritical system or by a fast nuclear reactor. The objective is to reduce the final disposal time of high-level radioactive waste (plutonium, minor actinides) from some 10^6 years down to about 1000 years. Lead (Pb) and lead-bismuth (PbBi) are foreseen as spallation-target and coolant of such devices.

The aim of the institute's contribution is the development of a suitable corrosion protection especially for parts under high loads like fuel claddings or pump materials in contact with liquid Pb or PbBi. Pulsed large area electron beams (GESA) are used to modify the surface of steels such that they fulfill the requirements of their surrounding environment. Corrosion test stands for exposure of specimens under relevant conditions are developed and operated. Test facilities for combined loads like erosion and corrosion and fretting corrosion were developed, built and operated. Conditioning the Pb with regard to its oxygen concentration and the transport of oxygen in PbBi are additional aspects of the work.

All tasks are embedded in European and international projects and cooperations like e.g. SEARCH, ESNIIplus and MaTISSE.

The most relevant results obtained in the reporting period are briefly presented:

Erosion-tests of promising materials for liquid metal pumps (MATISSE).

In MATISSE so called MAXPHASE materials (ternary carbides) are explored for their use in Pb alloy cooled nuclear systems. One objective beside the production of new types of such materials including CERMETS is the testing of their stability against erosion/corrosion in the CORELLA facility. In the last annual report, the result of two tests including MAXPHASE materials was reported. Test conditions of these tests were: liquid metal - PbBi at temperature of 300°C, duration of 500 h, PbBi velocity of v~8 m/s (700 rpm) – highly turbulent flow and a target oxygen content of O~10^{-7} wt%. The samples tested are: 316L with and without surface polishing, Ti_2AlC (MAXTHAL 211®) and Ti_3SiC_2 (MAXTHAL 312®) and graphite. Only MAXTHAL 211 showed a little corrosion erosion attack. To verify these results especially also for longer exposure times, the same specimens tested in the first two experiments were tested a third time for 1000h now. Total test duration of all test was 2000h. To verify and exclude all manufacturing problems for observing the erosion attack all specimens were inspected using a white light interferometer before and after the test run. For all the specimens no erosion corrosion attack is visible. At least under these conditions 300°C 10^{-7}wt% oxygen erosion corrosion attack is not an issue for all tested materials.

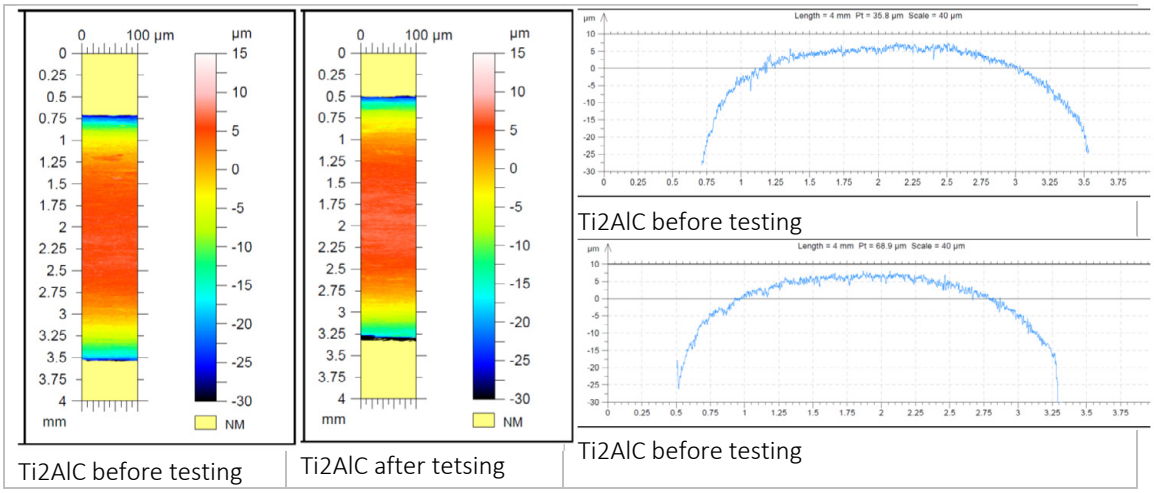

Fig. 3.1.1
Surface profiles of MAXTHAL 211 (Ti2AlC) before and after 1000h erosion corrosion test at 300°C

3.1.1 Corrosion test of MAXPHASE materials (MATISSE)

Most of the new designs of heavy liquid metal cooled reactors like ELSY and BREST 300 assume cladding temperature of around 550°C or higher. At this high temperatures steel components have an increased solubility in liquid lead or LBE (lead bismuth eutectic). A counter measure against dissolution by liquid metal is to form a stable oxide layer on the steel by solving oxygen in the liquid metal. But, corrosion tests on austenitic and ferritic/martensitic steels in liquid Pb or LBE (lead bismuth eutectic) revealed that they can´t be use without an additional corrosion protection at these temperatures, e.g. by protective coatings. Another solution could be the use of potentially insoluble MaxPhase materials. MAXphases ($M_{n+1}AX_n$) are ceramics, where M is an early transition metal, A is one of elements in group 13-16 and X is carbon or nitrogen. The layered ternary carbides and nitrides exhibit properties that are typical for ceramics as well as for metals. They show high electrical and thermal conductivity, machinability, damage tolerance, thermal shock resistance and are promising for application at high temperatures. Two Max-phases, Ti_3SiC_2 and Ti_2AlC, were chosen for the tests. Due to the synthesis process Max-phase material have beside the Max-phase always impurity- or secondary phases. TiC was detected by XRD as the secondary phase of Ti_3SiC_2. The XRD pattern of Ti_2AlC exhibits structures of Ti_2AlC, TiC, Al_5Ti_2 and $Ti_4Al_2C_2$.

Both material were tested in liquid eutectic PbBi up to 10 000h at temperatures between 550 and 700°C. The tests were conducted with two different oxygen concentrations (10^{-6}wt% and 10^{-8}wt%) in the liquid metal. The corrosion behaviour of max-phase material in liquid LBE/Pb depends strongly on the behaviour of the secondary phases in the max-phase material. This can lead to a severe oxidation or liquid metal dissolution attack in the space between the max-phase grains.

<u>Ti_3SiC_2</u>

- Like described in literature at 550°C/10^{-6}wt% TiO_2 (rutile) is formed at the surface, but after 10.000h parts of the surface start to disintegrate, which might lead to erosion in flowing PbBi.
- At 650°C and 700°C / 10^{-6}wt% the surface is protected by a double layered oxide structure with an outer part of TiO_2 (rutile) and a mixed inner layer of SiO_2 and TiO_2. After longer exposure at 700°C SiO_2 was measured by XRD in addition. The higher temperature favours protective oxide scales formation, which does not occurs at lower temperatures.

- At 10^{-8}wt% after longer exposure times at 550°C and 650°C defects can be observed at the surface, at the higher temperature a non-homogenous rutile layer protects the surface, here mainly the secondary phases are oxidized. The oxygen concentration is too low for formation of protective oxide scales.

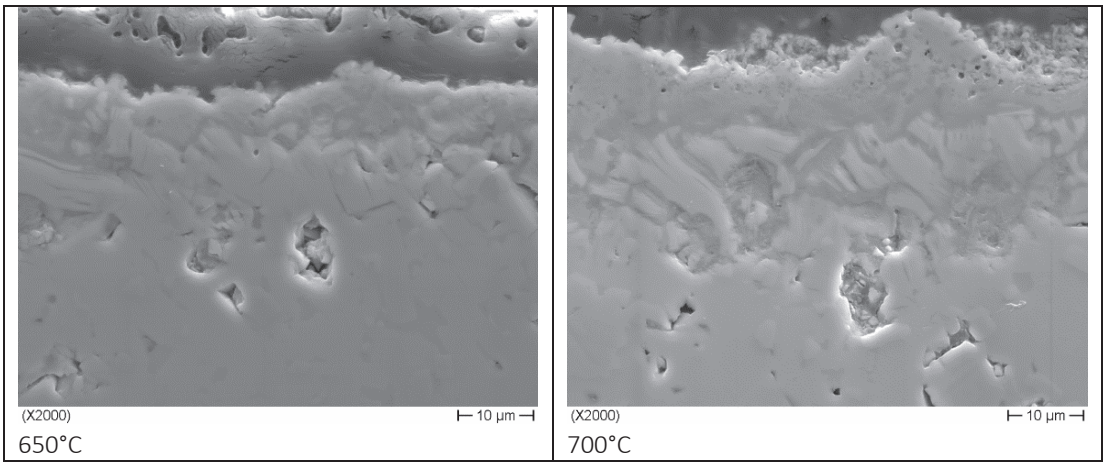

Fig. 3.1.2
Ti_3SiC_2 exposed in LBE with 10^{-6}wt% oxygen at 650°C (left) and 700°C (right) after 10.000h, showing an oxide layer at the surface mainly of TiO_2 with a rutile structure.

Ti_2AlC

- At 550°C/ 10^{-6}wt% a scale of TiO_2 (rutile) with inclusions of PbBi is formed, which lead to a 4.7µm thick mixed layer after 10.000 h. At the higher temperature no PbBi was found within the oxide scale. Additionally, Al_2O_3 peaks occur after 10.000h at 700°C in the XRD pattern. The formation of a protective oxide layer is to slow at temperature below 650°C, perhaps a pre-oxidation can help to avoid PbBi inclusions in the rutile layer.

- At 550°C/ 10-8wt% rutile was formed at the surface. At higher temperature and longer exposure times a strong dissolution attack occurred, due to the high activity of Al in the secondary phases. The oxygen concentration is too low to form a protective oxide scale.

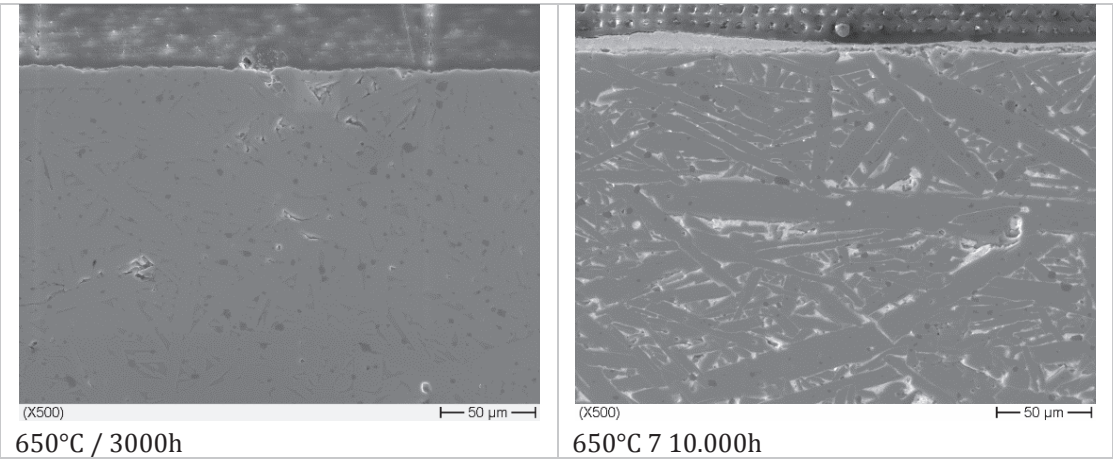

Fig. 3.1.3
Ti_2AlC after 3000h (left) and 10.000h (right) exposure in LBE containing 10^{-8}wt% at 650°C.

The results of all experiments are summarized in Table 3.1.1. They can be divided in 4 groups: good behavior (protective oxide layer at the surface or no change of the surface visible), some defects, defects or LBE inclusions and LBE infiltrated.

		10^{-6}wt% oxygen				10^{-8}wt% oxygen			
Material	Temperature	1000h	3000h	5000h	10.000h	1000h	3000h	5000h	10.000h
Ti_3SiC_2	550°C	☺	☺		○		☺		○
	650°C		☺		☺		○		○
	700°C	☺	☺	☺	☺	☺	☺	☺	○
Ti_2AlC	550°C		☺		○		☺		☺
	650°C		☺		☺		☺		●
	700°C		☺	☺	☺			●	●

Table 3.1.1
Summary of the results: ☺ good behavior, ○ some defects, ○ defects or LBE inclusions, ● LBE infiltrated

3.1.2 Oxygen Transport in liquid metals (SEARCH)

In the previous report, first results of tests performed in the MINIPOT device for oxygen transport measurements were presented. All oxygen sensors followed quite well the changes of oxygen potential of the gas phase. Several unexpected behaviour of the oxygen sensor signal was explained by interaction of oxygen with dissolved impurities. Further tests to clarify this interaction and water ingress tests and its influence on oxygen distribution are reported.

As mentioned above impurities dissolved in the LBE might play an important role in the oxidation transport and chemistry. Several experiments aiming to understand at least qualitatively were performed. Details on the reaction of the five oxygen sensors were investigated while the LBE temperature was changed from 411°C to 440°C. The oxygen content in the purge gas was kept constant at reducing conditions during this experiment.

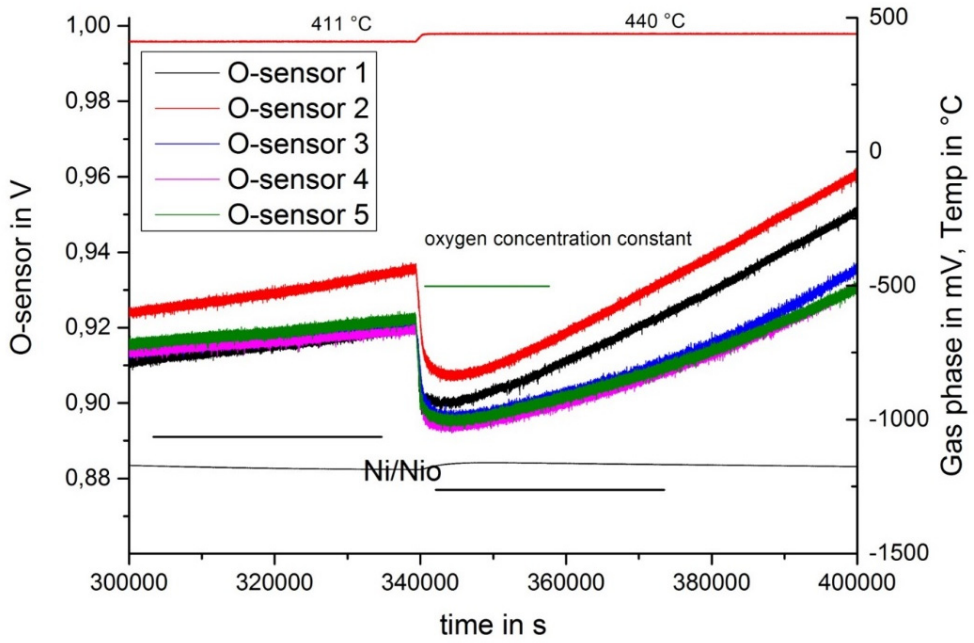

Fig. 3.1.4
Oxygen content in cover gas purge flow constant at reducing conditions –temperature increase from 422°C to 440°C

In the 40000s starting from time step 300000 all sensors show constantly increasing voltage signals (lower oxygen content in the LBE) while the Zirox reading (black line between Ni/NiO lines) also indicates that the oxygen content of the cover gas is reducing further in time. Increasing the temperature at such conditions should by theory result in a further increase in voltage of the oxygen sensors. However, with increasing temperature one can observe a short drop in voltage of sensors. The later increase in voltage is as expected at such reducing conditions. The green horizontal line labelled with *oxygen concentration constant* shows the expected values for the sensors 1, 3, 4 and 5 immediately after increasing the temperature. The black horizontal lines labelled with Ni/NiO show the theoretical values for Ni/NiO formation at the lower and higher temperature. A reduction of the voltage reading of the oxygen sensors can only be explained by oxidation or reduction of metallic impurities. If all Ni atoms in the vicinity of the oxygen sensors are reduced the oxygen sensor are showing increasing voltage values again.

To prove this assumption a similar experiment, changing the temperature at constant oxygen in the purge gas, was performed at a lower starting level of oxygen in the LBE.

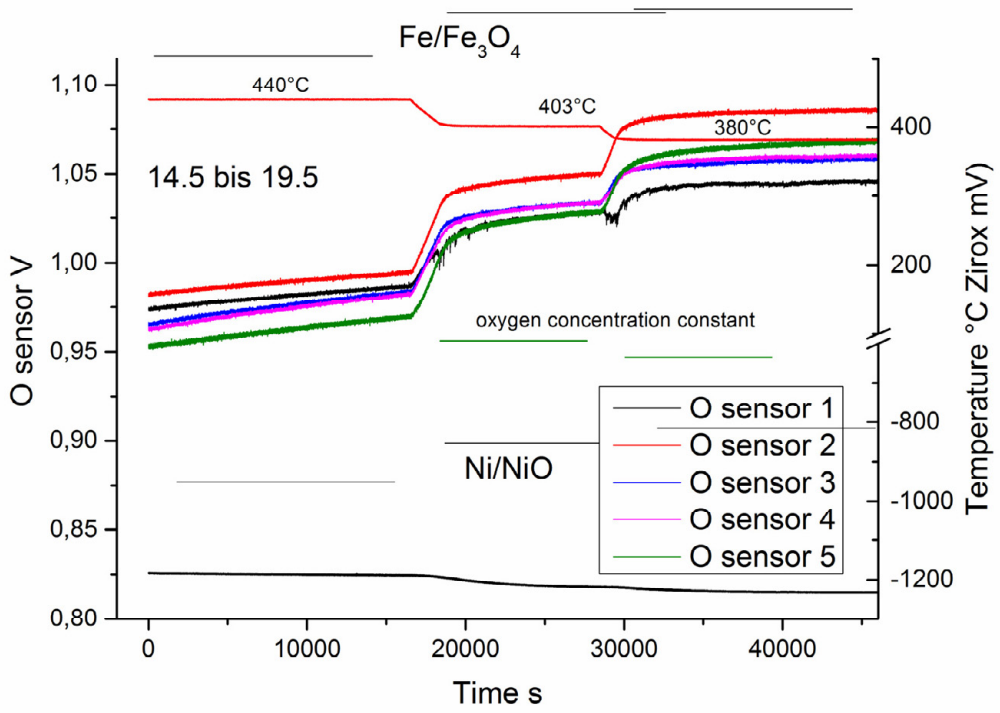

Fig. 3.1.5
Oxygen content in cover gas purge flow constant at reducing conditions –temperature decrease from 440°C to 403°C to 380°C

As expected, in the first 15000s all oxygen sensors show constantly increasing voltages (decreasing oxygen content). Lowering the LBE temperature from 440°C to 403°C° results in an increasing voltage signal at all 5 sensors. A further decrease in temperature led to a further increase of the voltage signal. Assuming that only dissolved oxygen interacts with the oxygen sensor the expected values at a temperature of 403°C and 380°C are marked as green lines in the figure as well. Such behaviour (increase of sensor voltage while temperature is decreased) can only be explained considering the formation and reduction of metal oxides like Ni/NiO or Fe/Fe_3O_4 or mixtures of both. The measured values are about in the middle of the theoretical values for Ni/NiO and Fe/Fe_3O_4 that might be an indication that mixed oxides or even more complex situations have to be considered.

Air ingress, as it may happen in an accidental scenario, was simulated purging air through the cover gas volume. The starting values for this experiment were a constant LBE temperature of 412 °C and an oxygen content in the LBE corresponding to an oxygen sensor level of about 0.92 V. All Ni impurities should be dissolved in metallic form at these conditions.

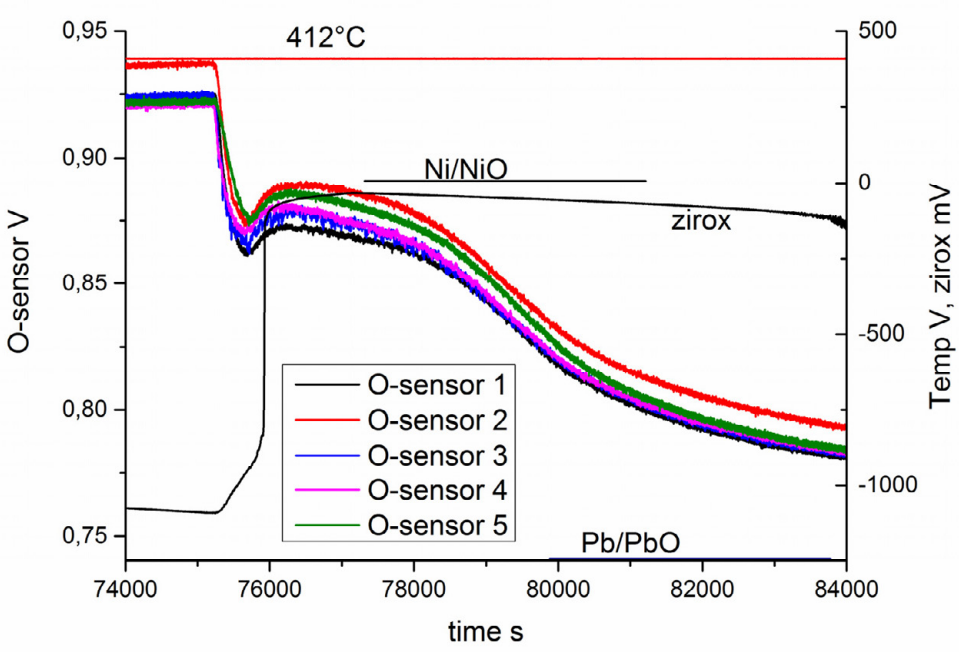

Fig. 3.1.6
Simulation of air ingress at constant LBE temperature.

After ingress of air that can be clearly seen at the black curve of the "Zirox" signal all oxygen sensor values drop sharply as expected. However, after some 100s the values increase again and remain at about 0.89V for some time before they drop again close to values indication oxygen saturation of the LBE (Pb/PbO line). The oxygen sensor reading of 0.89 V to which the sensors drift after the first decrease is very close to the Ni/NiO formation line at this temperature.

Again, like for the temperature effect, one additional experiment at a lower starting level of oxygen content in the LBE was performed. The temperature was kept constant at 410°C and the starting level of oxygen was about 1.035 V. The "Zirox" values (measured in some distance in gas atmosphere) were recalculated in equivalent oxygen sensor readings assuming that the sensor is located in the vicinity of the gas/LBE interface. Any transport mechanisms (adsorption and entrainment) via this interface are not considered, which can results in overestimating the real slope and the final values of the signal. Also here, after an initial drop the signals remain constant for a longer period of time. This again can only be explained by the influence of metallic impurities on the oxygen activity and content. The measured value of this constant period is very close to the effects seen before, which indicates the formation of mixed FeNi-oxides. Also interesting to consider are the slopes and the onsets of the different oxygen sensor curves. The slowest drop is measured with oxygen sensor 5 located in the pocket and by that separated from the main flow. This sensor also shows the latest response. Sensor 3 and 4 start reacting first sensor 1 and 2 follw. Also the slope of sensor 3 and 4 is higher than that of sensor 1 and 2. Comparing this to the simulated response of the sensors on an instantaneous jump of the oxygen content of the cover gas shows a principal agreement. There, also sensor 3 and 4 start to react and react most intensively.

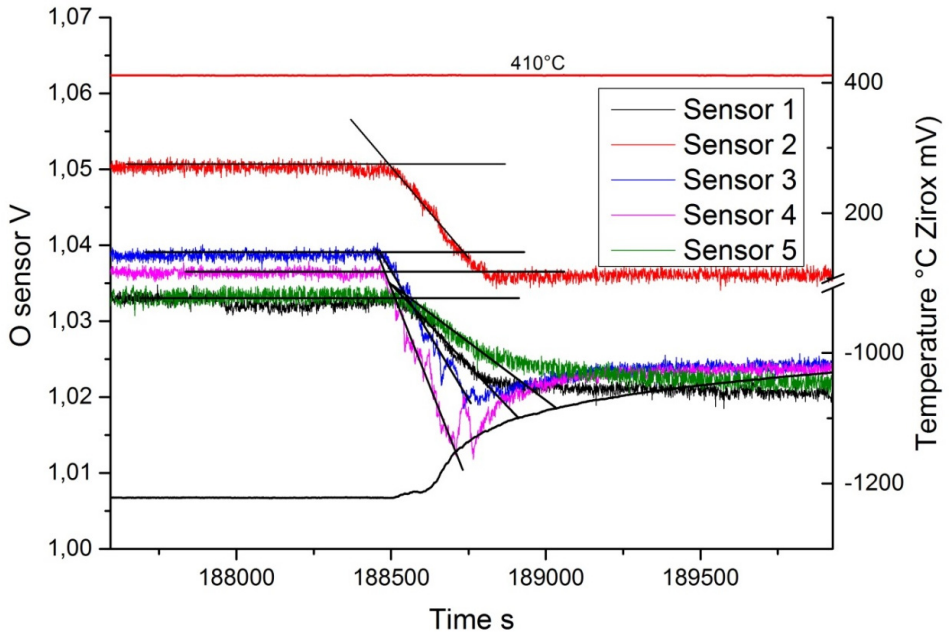

Fig. 3.1.7
Air ingress at constant temperature.

Water ingress

Some experiments to simulate water ingress into LBE were performed at the end of the SEARCH project. The LBE temperature was kept constant at 430°C and the cover gas was set to reducing conditions. The oxygen sensor reading was pretty similar for all the sensors at a value of about 0.89 V and slightly increasing over time (reducing cover gas). About 0.232ml water, which is about 1.16×10^{-5}vol %, were injected with Ar 5 %H_2 at a pressure of 2 bar into the LBE. The experiment was repeated several times and the response of the oxygen sensors and the related thermocouples was investigated. The reaction of all sensors became weaker by the later experiments most likely due to oxide formation in the tip of the lance. Zoom in data shows the distinct and almost immediate reaction of all sensors beside sensor 5. The fastest and strongest reaction is seen at sensor 4 that is located in the direct vicinity of the water ingress lance. This is also the only thermocouple that showed a little reaction – all others remain more or less unchanged. The cover gas ("Zirox") showed a reaction after about 40s, which is in good agreement with the assumed travel time of the cover gas to reach the measurement device. Several repetitions of this experiment confirmed these principal observations.

To verify these observations a mass spectrometer was installed additionally to survey the cover gas response directly. The travel time and reaction time of the MS were considered in the diagram already.

The MS signal of water is plotted together with the oxygen sensor, the "Zirox" sensor (cover gas oxygen) and the temperatures. The water injection is marked by a vertical line. The Ar and H_2 signal are both increasing almost immediately after the water injection (Ar +5 %H_2 is used to press the water into the LBE). And both signals also start decreasing immediately after this first increase. The water and the oxygen signal both are decreasing at this early time after the injection but start to increase 20 sec later. The water signal show a more steep increase compared to the oxygen signal which reacts parallel but with less intensity. Water seems to need about 20 s to reach the cover gas, which can only be explained considering that the

droplet injected is transported with the LBE flow and not just swimming up directly. During this transport there might be some dissociation of the water, which can be seen at the oxygen potentials of the sensors 1 to 4, which are showing dropping before the water has reached the cover gas.

The oxygen sensors 2, 3 and 4 show an almost instantaneous reaction, both show increasing voltages meaning reducing oxygen values. This increase stops after about 9 s and is reflected by the peak in the Ar and H_2 MS signal. Right after this peak the readings of the oxygen sensor starts dropping as expected when water is injected. The sensor 1, which is located closest to the surfaces and most far away from the injection point shows the peak in the signal a littler later than the others, sensor 5 (the one in the pocket) do not show such peak at all. Considering all these findings one can assume that this short term increase in voltage is caused by the gas used to press in the water. The MS signals also show that this gas at least partially reaches very fast the cover gas. In later stage, when the water has reached the cover gas, all sensors beside sensor 1 show a minimum, which comes about 500s after the maximum of the water peak in the cover gas. This is in agreement with the time, changes in the cover gas need to be "noticed" entirely by the oxygen sensors. Comparing the amplitude of the changes of the sensors 2 to 5 one can clearly see that sensor 5 (the one separated from the main flow) shows the smallest changes. As already said previously, this sensor also don't show increasing values just after the water inlet. Different to all the other sensors is the behavior of sensor 1 in the later stage of the experiment. The values measured do never reach lower values compared to once before the water was pressed in. So far there is no explanation for this observation.

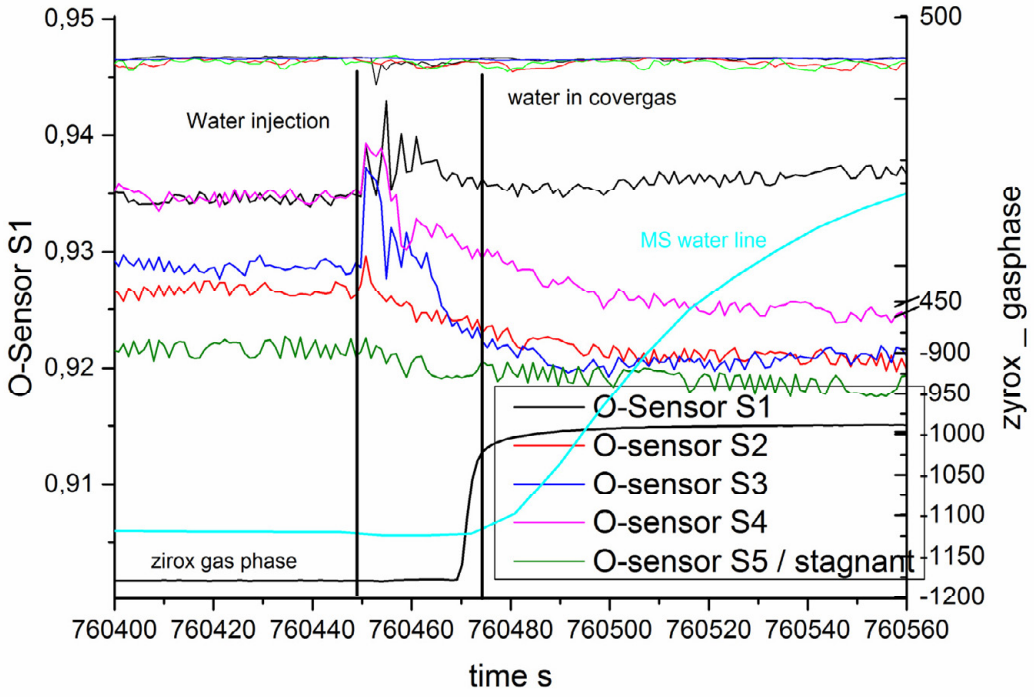

Fig. 3.1.8
2nd water ingress experiment with Mass spectrometry of cover gas. Upper: overview, lower: zoom at water injection time.

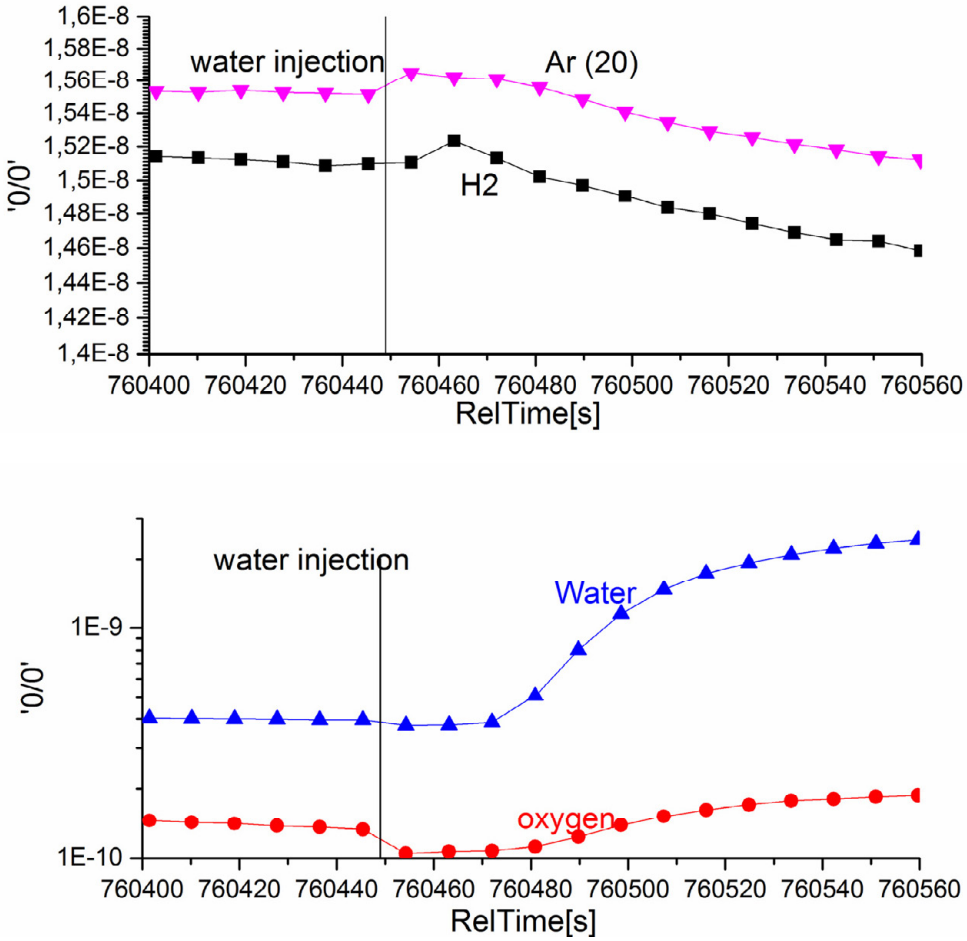

Fig. 3.1.9
Mass spectrometer signals of H_2, Ar, water and oxygen.

3.1.3 CFD simulation of dedicated tests

CFD simulations were performed using the program that was set up for the design relevant simulations. As starting and input data, recalculated data are used. Optimization of the CFD program applying mesh refinement or adaption of Schmidtnumber was performed in a very limited way so-far. The CFD code requires as boundary condition the changing oxygen content in the first LBE layer attaching the cover gas. An additional assumption was made for the oxygen content in the LBE. It should be distributed at the starting time of the changes almost homogeneously in the liquid metal. Due to experimental constraints there is no possibility to measure the oxygen content in this first upper LBE layer. Therefore, the oxygen level of the gas phase measured with the "Zirox" device installed in the cover gas control system was recalculated in time (travel time to "Zirox about 30s) and level to a corresponding oxygen content (in sensor voltage) without considering any transport resistances by the cover gas LBE interface. It is known that adsorption and transport of oxygen at the LBE gas interface plays a significant role. Therefore, any deviation between measurement and CFD can be explained easily by such issues. The CFD data shows quite similar response for the sensors 1 to 4 and significant difference to sensor 5. Compared to this, the data of measured values can be ordered in three groups: Sensor 3 and 4 reacting fastest, sensor 1 and 2 a bit slower and like for the CFD simulation sensor 5 that reacts latest and with most less intensity. Also the real measured values of the sensors are different from simulated ones. One major problem is as discussed

previously the input data. Another aspect is the observed change in measured oxygen potential due to oxidation/reduction reactions of dissolved metallic impurities. This oxidation/process influences the kinetic (slope of the curves) and the absolute values that can be reached.

Another important issue in CFD simulation is the influence of the mesh size on the reaction time of the sensors. This influence is shown comparing simulations done with a coarse and fine mesh. The coarse mesh used for the design simulations seems not being appropriate for realistic simulation of experiments. Not considered so far is the Schmidnumber, which describes the transport of species by the flowing LBE. Further efforts to optimize mesh size and all other CFD parameters are required.

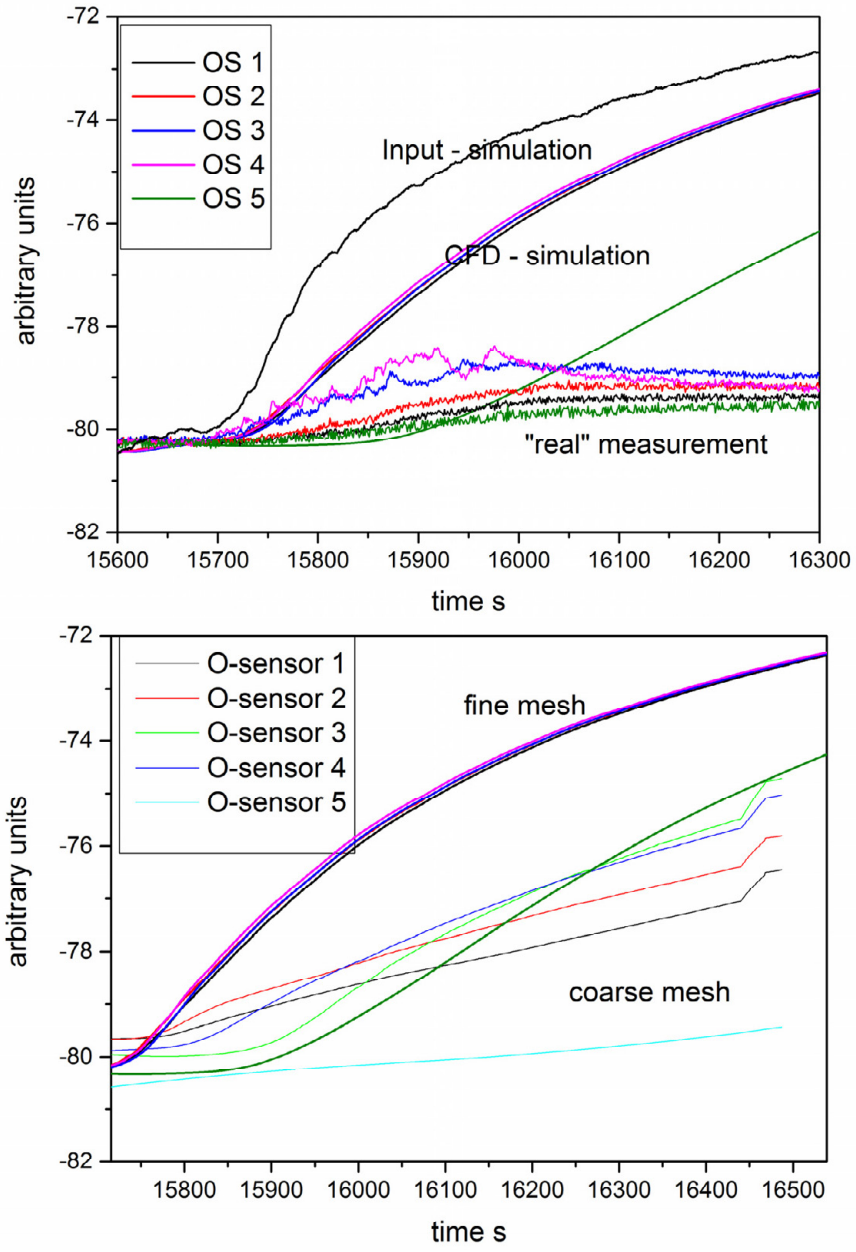

Fig. 3.1.10
Upper: Comparison of CFD- simulations (left) and "real" experimental data. Below: comparison course and fine mesh.

Summary

The basic idea of the experiment to track experimentally oxygen transport in flowing or stagnant LBE was achieved by this work. The locations of the oxygen sensors that were determined by pre-design CFD calculations allow monitoring oxygen transport. It is obvious from all experiments that oxygen transport by flowing LBE is quite different from oxygen transport by stagnant LBE (dead pocket oxygen sensor 5). Oxygen sensors give all a little bit different readings, therefore also their response time might be questionable. However, the obtained results seem to be quite reasonable and can be explained considering all involved processes.

However, some important issues have to be considered for interpreting and discussing and future experiments. The volume of the cover gas is too large for fast changes. The amount of impurities like dissolved metallic species (Ni, Fe, Cr, ..) play a very prominent role in the oxygen sensor reading and also in the amount of free oxygen (dissolved) that is available for steel oxidation. Online impurity tracking would be required or at least dedicated tests that allow determining the amounts of free oxygen as a function of dissolved impurities would be highly beneficial. CFD simulations were highly helpful to design the reactor. But, so far none of the experiments could be simulated properly – this requires further efforts in measurement and simulation.

3.1.4 Pressurized tube experiment (MATTER)

During operation of lead fast reactors (LFR) or the MYHRRA reactor in Belgium swelling of the fuel by irradiation or fuel cracking increase the stresses on the inner cladding wall, which can influence the corrosion behaviour and the stability of the cladding tubes. In the previous annual report the experimental set-up was presented. Now, first tests with pressurized tubes at 550°C in PbBi with an oxygen concentration of 10^{-6}wt% were conducted.The tested tubes are cold worked DIN 1.4970, a Ti stabilized 15/15 CrNi steel, with an outer diameter of 6.56mm and a wall thickness of 0.45mm. Tube sections of 45 mm length were welded using TIG (tungsten inert gas) welding to a 3mm outer diameter stainless steel tube that connects the test tubes with the pressure cylinder.

An alumina crucible contains the PbBi in which the samples are immersed. The hoop strain (measured as an increase of tube diameter) is transferred via a ceramic rod that is guided in a stainless steel tube to a copper plate at top of the test- cell where a laser triangulation device measures the strain. This in-situ strain measurement was influenced by thermal expansion of the test-set up due to daily temperature changes in the experimental hall and will not be presented. The entire test-cell is vacuum tight, the oxygen content in the PbBi is measured using a ZrO_2 based oxygen sensor and controlled via the gas atmosphere above the PbBi. The temperature is maintained using an external heating jacket and controlled via a thermocouple that is protected by an alumina tube, which is immersed in the liquid PbBi.

The conducted tests had an exposure time of 1008h for the reference sample and the sample with an internal pressure of 550bar. The sample with an internal pressure of 600bar were exposed 300 and 600h. After the experiment the specimens were cleaned from adjacent PbBi and the outer diameter of the tubes was measured using a micrometer gauge each at 5 different positions at least twice. The outer diameter of the reference samples measured after exposure is within the fabrication tolerance of the tubes. All other samples showed a clear increase in diameter between 17 and 23µm.

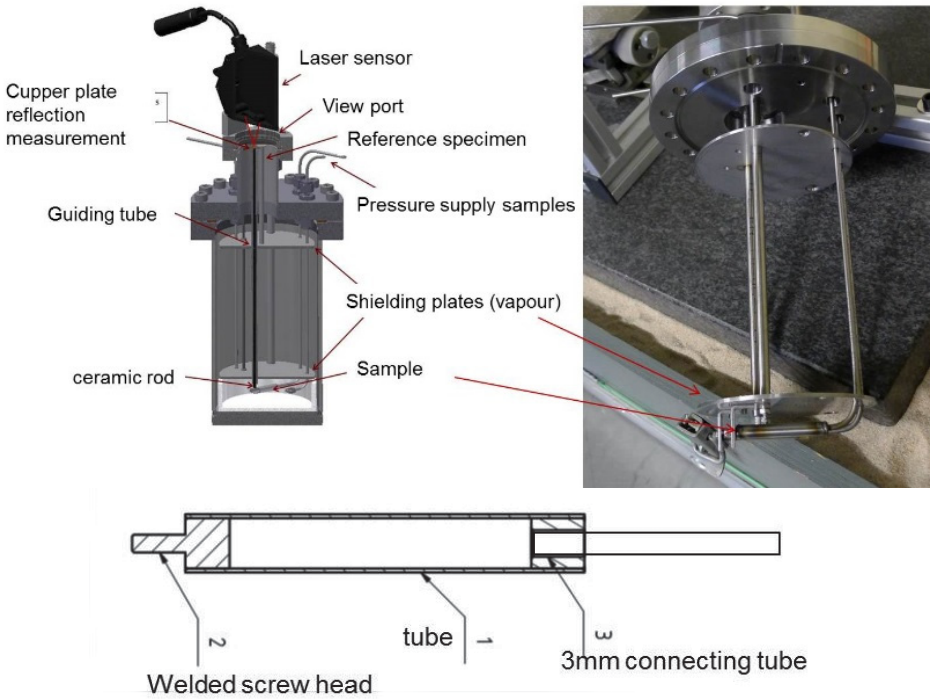

Fig. 3.1.11
Scheme of test-cell and pressurized tube sample and photo of realization (samples and ceramic rod).

As expected, a thin not visible Fe-Cr-Mn spinel with Si was formed at the surface of the reference sample. Localized the scale is interrupted by oxides nodes consisting of magnetite at the top with a spinel layer underneath and an inner oxidation zone (IOZ). At 550bar internal pressure the number of oxide nodes at the surface increases and the grain boundary oxidation is much more pronounced. The oxide roots went up to 11µm, while that on the reference sample only reaches around 5-6µm deep into the steel.

The results after 300h and 600h at 600bar are comparable and differs from previous described samples. The induced stress enhance the oxidation. Nearly the whole surface in covered by a multilayered oxide consisting of magnetite, spinel and IOZ. Sometimes the magnetite is spalled off. After 300h the IOZ going up to 15µm deep into the steel. Although, at the area with a thin Fe-Cr-Mn oxide a small IOZ can occurs. Occasionally small cracks are visible at the surface of the oxide, cracks in the balk material do not occure.

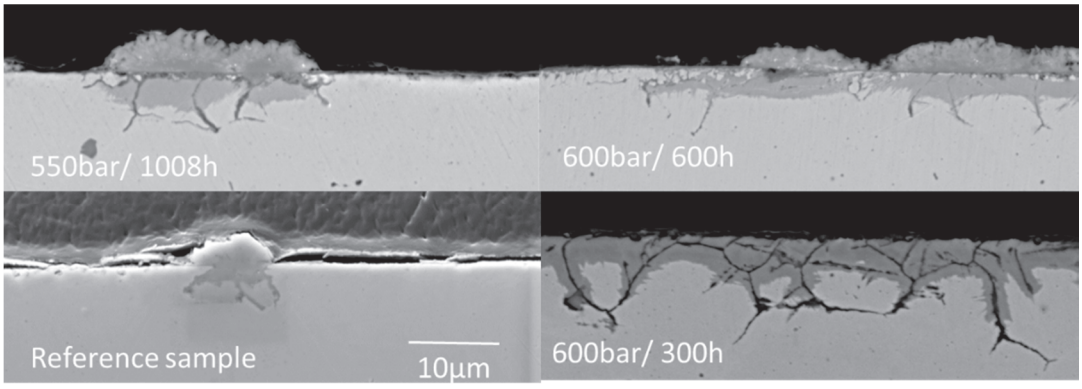

Fig. 3.1.12
Cross sections of the samples after exposure at 550°C to PbBi with an oxygen concentration of 10^{-6}wt%.

3.1.5 GESA Beam Dynamics Simulations

The quality and stability of the pulsed electron beam is crucial for optimization of the GESA treatment of metal targets. In order to tune beam parameters and control the beam homogeneity and stability in a reliable way, sound understanding of all related plasma physics processes and their effects on the beam is necessary. This includes the interactions between charged particles, electromagnetic fields, and structural materials. In the reporting period, the commercially available PIC code MAGIC by ATK, USA, was used to investigate the behavior of the pulsed electron beam generated by GESA-SOFIE, the newly built diagnostic GESA.

To setup the simulation, the geometry of the GESA facility is configured by conductor and dielectric parts, grids, and magnetic coils. Different electric potentials of the various conducting structures are introduced via ports. These are open boundaries of the simulation volume, at which the input electric field is specified. In order to mimic the real experiment as closely as possible, only one port was used in the simulation of GESA-SOFIE to apply a certain cathode potential against the grounded anode. This port corresponds to the high-voltage Marx generator used in the experiment. The potential of the other conducting parts, in particular the grid potential, are controlled by several resistors as done in the experiment. In order to achieve a small internal resistance of the generator (respective port) as chosen in the experiment, the geometry of the port was adjusted accordingly. Note that in the simulation ports are impedance matched by default, thus their internal resistance is directly linked with their geometry.

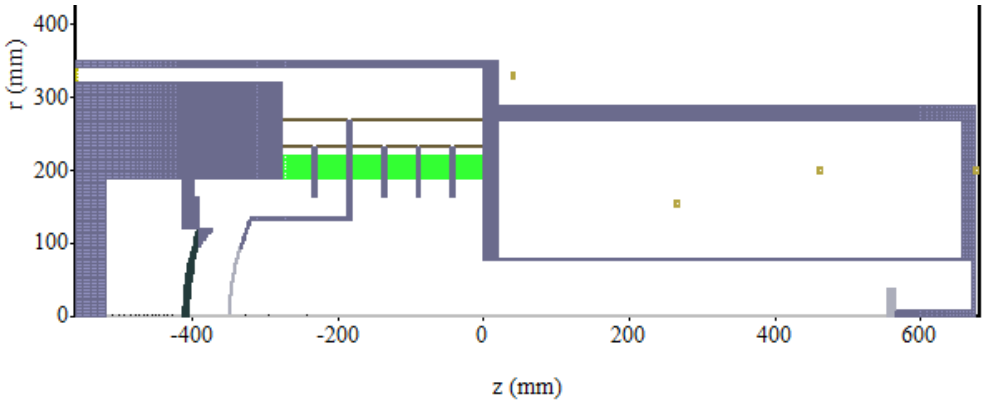

Fig. 3.1.13
GESA-SOFIE configuration used for electron beam simulations with MAGIC.

In order to generate charged particles, a selection of various emission commands is available. The algorithm for explosive emission, the type of emission taking place at the GESA cathode, is based on a phenomenological approach. The main drawback of this approach is that the physics of the emitting plasma (e.g. its expansion) is not considered. The simulations of GESA-SOFIE performed in the reporting period included explosive electron emission at the cathode as well as ion emission at the target. In the experiment, ions may be generated by secondary emission, by desorption and ionization of surface contaminants, or by evaporation and ionization of target material. Whichever the most relevant ion generation process is, emission will never exceed the space charge limit. Therefore, ions (protons) were introduced into the simulation volume by the explosive emission routine to investigate their maximum possible effect. In contrast to earlier simulations where the grid was generated by the FOIL command, the controlling grid was now composed of individual conductor parts. This allows ions to penetrate into the gap between cathode and grid.

As soon as the protons reach the cathode (after about 280 ns, ion current about 0.3 A), electron emission increases slightly from 128 A to 131 A in the specific case shown here with cathode potential 120 kV and grid potential 80 kV. The proton density radial distribution in the cathode – grid gap is not homogeneous. Due to their larger mass compared to electrons, ions do not follow the magnetic field as closely. As a result, the ions reach the cathode only on a central spot, see figure below. This spot has a radius of about 3 cm after 500 ns and of about 5 cm after 700 ns. Note that the cathode has a radius of 10 cm. Thus, only in the central region partial electron space charge neutralization occurs, followed by an increase in electron emission and electron space charge, here of about 10 %. The outer region is unaffected by the ions. The 10 % increase of electron density in the central region is consistent with the observed current increase. In summary, protons generated at the target have only minor influence on the current density of GESA-SOFIE.

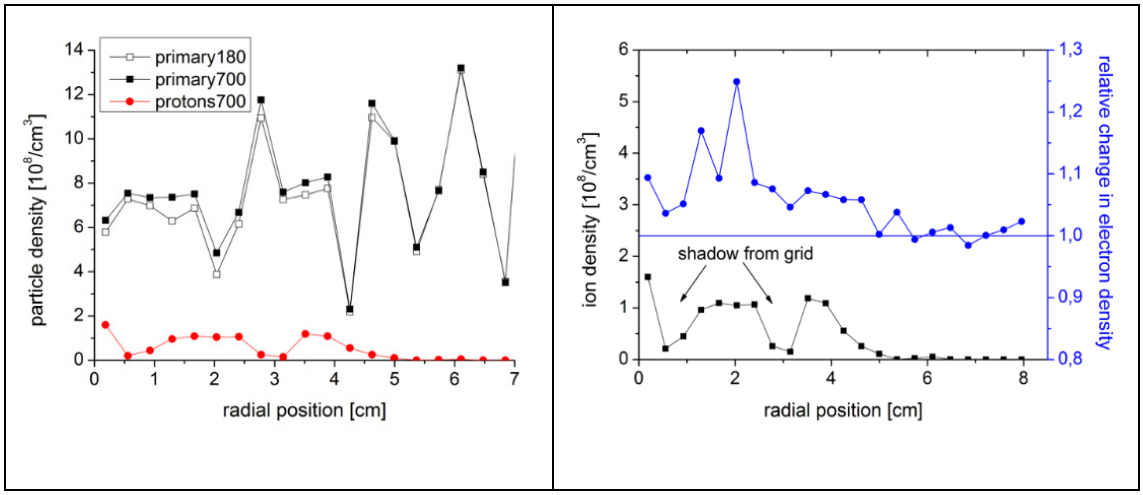

Fig. 3.1.14
Left: Electron and proton density close to the cathode surface after 180 ns (prior to the arrival of protons, open symbols) and after 700 ns (closed symbols). Right: Data of electron density from left graph shown as relative change (data after 700 ns normalized to data after 180 ns), compared with proton density.

Apart from setting up, understanding and controlling the simulation itself, MAGIC simulations were mainly used to optimize the geometry of GESA-SOFIE. First, the influence of the magnetic field configurations and its strength on the beam performance were tested. In the figure below, the electron beam is shown for standard magnetic field configuration but with various strengths. Green dots are primary electrons, the blue ones are scattered at the grid, and the red ones are backscattered from the target. B0 denotes the default magnetic field strength used in the experiments. Due to a subtle misalignment of magnetic and electric field in the gap between cathode and grid, which cannot be avoided completely in the experiments, the beam electrons experience a drift motion and start to gyrate along the magnetic field lines. The collective gyration leads to a pulsation of the beam envelope. An increase in the electric field (potential drop) between cathode and grid leads to an enhancement of the beam pulsation, see figure. The higher the magnetic field strength is, however, the smaller is the radius of gyration and the beam pulsation amplitude. For the magnetic field strength used in the experiments (B0), beam pulsation is negligible.

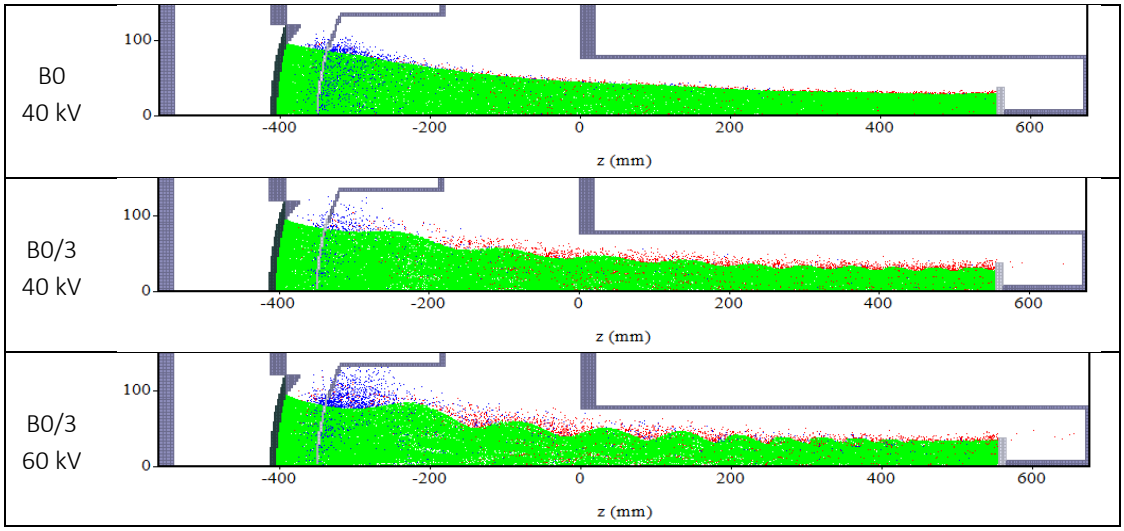

Fig. 3.1.15
Beam shape of GESA-SOFIE for various magnetic field strengths and potential drops between cathode and grid.

In another set of numerical experiments, the curvatures of cathode and grid were modified. A planar cathode geometry is necessary for in-situ diagnostics of the emission process. In the figure below the planar cathode is tested with and without Pierce electrode. In the absence of the Pierce electrode, the beam expands in the cathode-grid gap, followed by a more pronounced focusing of the beam after passing the grid. The high space charge in the focus point leads to the formation of a virtual cathode between grid and anode. To avoid the virtual cathode formation, a cone shaped electrode is introduced as an extension of the second gradient ring between grid and anode, see figure below. With this new geometry, no virtual cathode is formed, even without Pierce electrode.

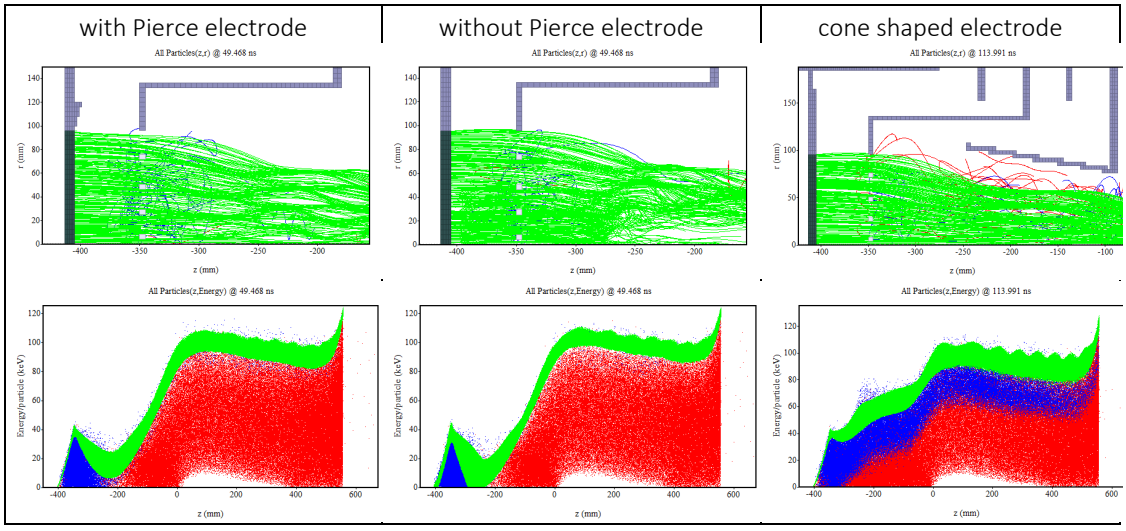

Fig. 3.1.16
Trajectories and kinetic energy of primary electrons (green), electrons scattered at the grid (blue), and electrons backscattered from the target (red) for three different electrode configurations of GESA-SOFIE.

3.1.6 Optimization of FeCrAl to be used as corrosion barrier in liquid metals

Alumina-forming Fe-Cr-Al-based alloys are high temperature structural materials, which are well known for their resistance against environment attack in the temperature range of 900-1400°C.

Nowadays, bulk alloys and modified surface layers belonging to the Fe-Cr-Al alloy system are under scientific evaluation as potential structural materials and functional surface layers in energy-related high temperature applications.

Our previous results, concerning the morphology, composition, structure and thickness of the oxide scales, grown on Fe-Cr-Al-based bulk alloys and modified surface layers during exposure to oxygen-containing molten lead (10^{-6} wt.% oxygen and 400-600°C), allowed us to draw the alumina stability domain and also to define the criterion of the Al/Cr ratio for the formation of a highly protective alumina layer (ec. 1).

$$C_{Al} = 15.3 - 0.81\,(C_{Cr}) + 0.0156\,(C_{Cr})^2 \text{ [wt.\%]} \quad (1)$$

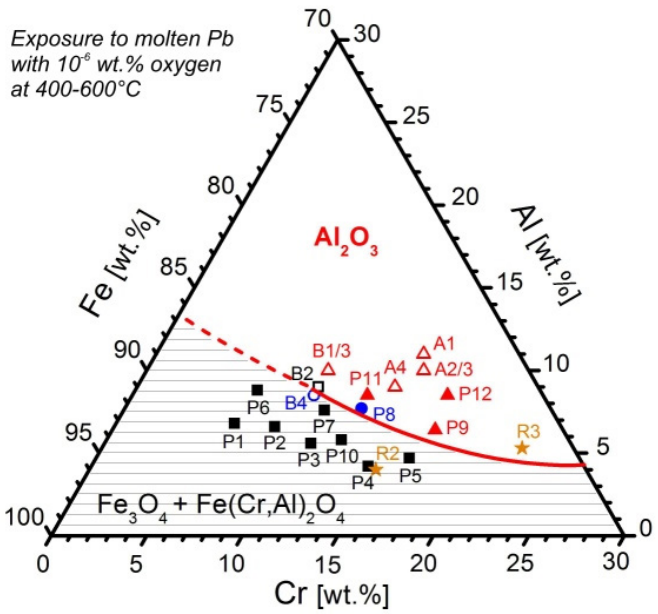

Fig. 3.1.17
Oxide "map" for the oxidation of Fe-Cr-Al-based bulk alloys and modified surface layers exposed to molten lead containing 10^{-6} wt.% oxygen in the temperature range 400-600 °C (■): alloy sample forming Fe-based oxide scale; (□): modified surface layer sample forming Fe-based oxide scale; (▲): alloy sample forming alumina scale; (Δ): modified surface layer sample forming alumina scale; (●): alloy sample forming both Fe-based oxide and alumina scale; (O): modified surface layer sample forming both Fe-based oxide and alumina scale; (★): other alumina-forming alloys of type Fe-Cr-Al-RE.

During 2015, an experimental campaign was performed in order to evaluate the influence of the addition of small quantities of reactive elements (Y, Zr, Hf and Mo) on the structural stability and the adhesion to the alloy substrate of the thermally grown alumina scale. Starting from the base-composition Fe-16Cr-XAl (X = 4, 6, 8 wt%) with the addition of 0.5 wt.% of the reactive elements, 14 model alloys were produced by arc melting from pure elements.

The investigation of the samples is still underway; preliminary results, obtained by scanning electron microscopy on the samples exposed for 3500h at 500, 550 and 600°C to molten lead with 10^{-6} wt.% oxygen, have shown that all samples were protected by an oxide scale, either being alumina or aluminium containing spinel-type oxide. The analysis of the composition, structure and thickness of the oxide scales will be performed by EDX and XRD characterization methods.

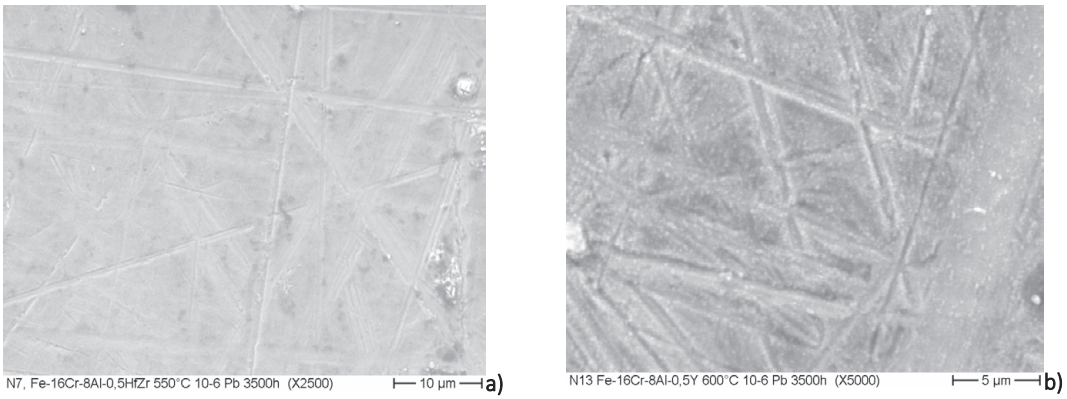

Fig. 3.1.18
SEM images showing the morphology of the protective oxide scale, thermally grown on Fe-16Cr-8Al-0,5 (ZrHf) – (a) and on Fe-16Cr-8Al-0,5Y – (b)

The corrosion resistance of the alloys containing Zr, Mo and Y, as reactive elements, exposed to high temperature steam was evaluated in cooperation with a research team from KIT-IAM. Samples made from alloys containing Y and Zr were protected by an alumina scale up to 1400°C, while samples containing Mo as reactive elements shown large area with exfoliated alumina scale.

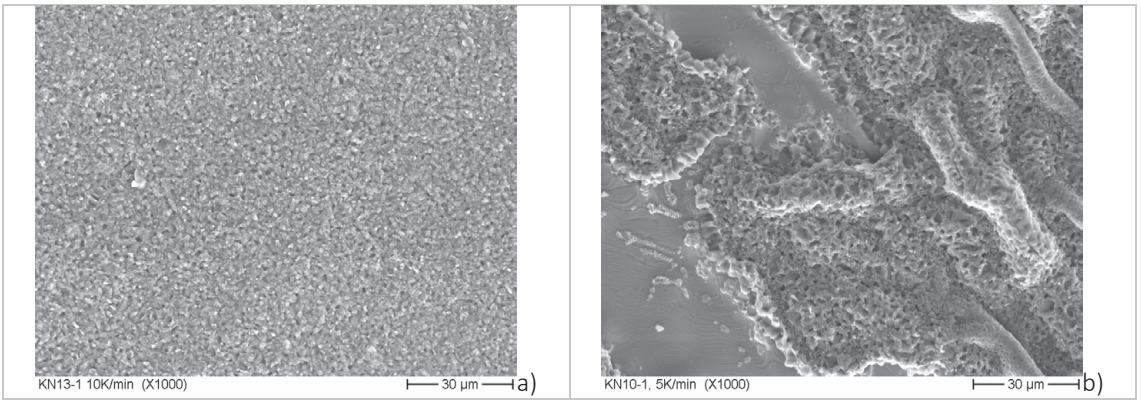

Fig. 3.1.19
Oxide scale morphologies observed (SEM) on Fe-16Cr-8Al-0,5Y (a) and Fe-16Cr-8Al-0,5Mo (b) heated in steam from 500°C with the heating rate of 10K/min and 5K/min, respectively, to 1400°C with one hour holding time.

3.1.7 V-Al-C MAXPHASE

A class of layered ternary carbides and nitrides, known as “MAX phases”, has attracted the attention due to its unique combination of properties: light weight, machinability, relatively high fracture toughness, good thermal and electrical conductivities, thermal shock resistance and high-temperature corrosion resistance.

Following the technological steps, previously defined by our group, batches of V2AlC ternary carbides powder were synthesized from elements. From this powder, disk-shaped samples with > 95 % in volume Max-phase were obtained by pressureless sintering. The minor phases were V5Al8 and VC, as shown in the X-ray diffraction pattern in Figure below.

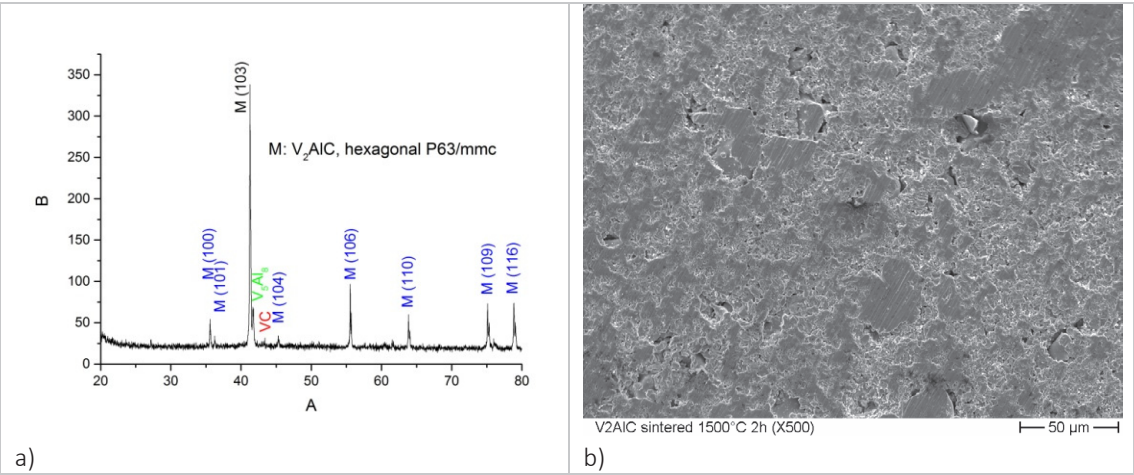

Fig. 3.1.20
1 X-ray diffraction pattern (a) and surface morphology (b) of the sintered ternary carbide sample with V_2AlC Max-phase.

Isothermal steam oxidation tests were performed in KIT-IAM using a commercial thermal balance (NETZSCH STA-409) with a vertical tube furnace (balance under the furnace), coupled with a state-of-the-art mass spectrometer Balzers GAM300. All specimens were heated to the desired temperature in high purity Ar atmosphere with a gas flow rate of 3 l/h Ar . The temperature was hold for 10 min and then the atmosphere was changed to 3 l/h Ar and 3 g/h H_2O and held for 15 hours. Finally, the furnace was cooled down to room temperature also in high purity Ar atmosphere with a gas flow rate of 3 l/h Ar.

SEM evaluation revealed the oxidation of both V and Al samples at the surface. After exposure to steam at 800°C, islands of Al_2O_3 (dark spots) embedded in VO_2 were observed. At 1000°C only few spots with alumina were observed, while at 1200°C, VO_2 covered the entire sample.

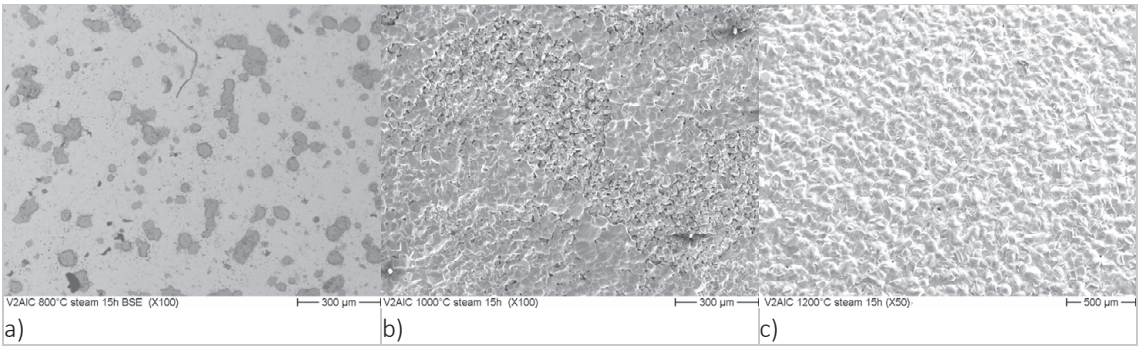

Fig. 3.1.21
Morphologies of the thermally grown scales on ternary carbide samples with V_2AlC Max-phase exposed at 800° (a), 1000°C (b) and 1200°C (c)

The structure and thickness of the oxide scales grown on the samples with V_2AlC Max-phase are under evaluation.

Currently, liquid metal corrosion experiments are being performed at 500°C and 600°C in molten lead (Pb) containing 10^{-6} wt% oxygen.

Involved Staff:

DP W. An, Dr. R. Fetzer, A. Neukirch, Dr. A. Heinzel, M. Hochberg, Dr. A. Jianu, DI (Fh) F. Lang, Prof. G. Müller, Dr. G. Schumacher (Gast), A. Sivkovich, **Dr. A. Weisenburger**, DI (Fh) F. Zimmermann

4. HGF Programm: Rationelle Energieumwandlung und Nutzung (EMR)

4.1 Dielectric Characterization, Concepts and Results

4.1.1 Dual mode resonator

Microwave heating offers numerous advantages in material processing over conventional heating. These advantages include volumetric heating, higher energy efficiency, shorter processing time and theoretically no temperature limit. This motivated the development of various microwave systems and processes. For a successful system and process design the detailed knowledge of the dielectric properties of materials is mandatory. In this connection an in-situ measurement setup for dielectric and calorimetric characterization of materials has been developed based on a dual-mode cavity. Two orthogonal modes, TE_{111} and TM_{010}, are used for simultaneous dielectric characterization and heating of the material under test. The cavity is designed for the dielectric characterization of materials close to 2.45 GHz. In addition, a qualitative calorimetric analysis of exothermic and endothermic reactions is envisaged.

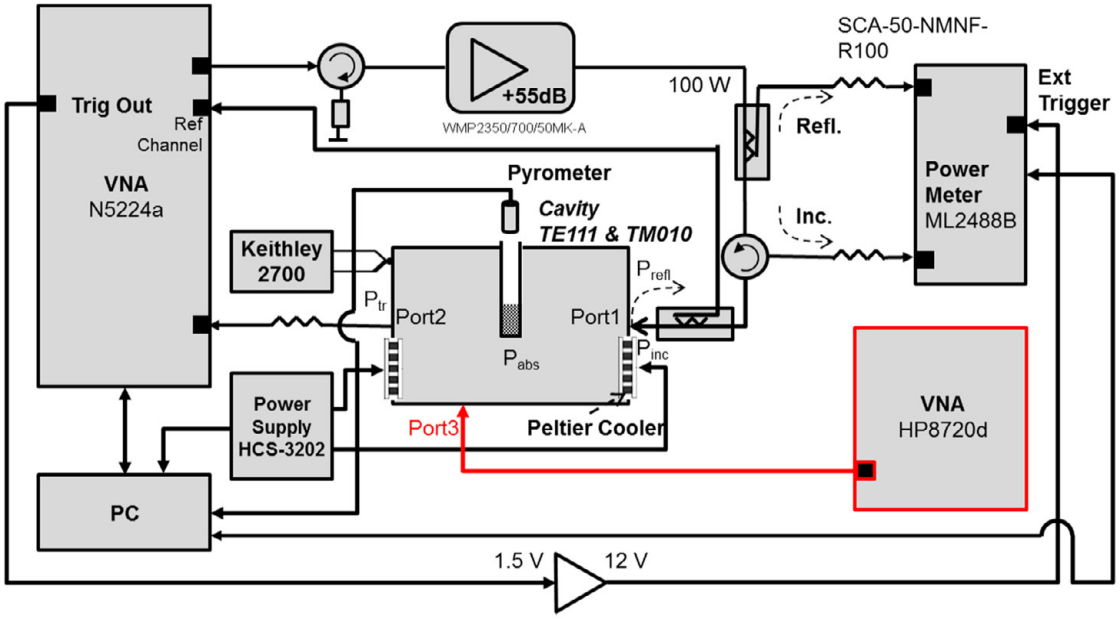

Fig. 4.1.1
Block diagram of the designed system

The block diagram of the measurement system is shown in Fig. 4.1.1. A key element of the measurement system is the tunable power amplifier WMP2350/700/50MK-A from G-Way Microwave which provides amplification by min. 50 dB with 100 W maximum output power. A vector network analyzer (VNA) Agilent N5224A is used for both, the measurement of the transmission coefficient for the TE_{111} mode and as input power source for the amplifier. A second VNA (HP8720d) is used for measuring the reflection coefficient at port 3 for the TM_{010} mode.

By use of a directional coupler and a circulator incident and the reflected power can be measured individually with an Anritsu ML2488B power meter. For the temperature measurement the pyrometer type CellaTemp PA10AF1 is used. The pyrometer signal is used for temperature control along any pre-set temperature profile with the help of a PID control algorithm. The output signal of the PID controller is converted into a frequency span for the VNA to achieve a smooth power control. The smaller the frequency span the larger the heating rate of the sample and vice versa.

For the finding of dielectric constant and loss factor from the measured frequency shift (f_{ref}-f_s) and the measured change in the Q-factor ($1/Q_s$-$1/Q_{ref}$) the inversed task has to be solved numerically. However, to increase the accuracy and the speed of this procedure we employ a neural network. For that purpose the MATLAB Neural Network Toolbox trained with the Bayesian algorithm was used. The training of the neural network is performed with the help of 3D full wave simulations in CST Microwave Studio for the range of the expected dielectric properties.

Presently, the neural network is trained with a database from only 200 combinations of (ε', ε'') for the range $1.5 < \varepsilon' < 40$ and $10^{-4} < \varepsilon'' < 1$. So far obtained results coincide very well with literature data. By further improving the topology of the neural network and by extended training the accuracy will be further improved.

4.1.2 Error Analysis for various cavity modes in a wide materials parameter range

Investigation of limits and accuracy of the cavity perturbation method for dielectric measurements is important, in particular for measurements of materials having either very low or very high permittivities. The cavity perturbation method is based on the evaluation of the central frequency (f_0) and Q-factor of the resonance (S_{21}) peak. The minimal errors for f_0 come from instrumental errors of the VNA: $\sigma_f = (f_{max}-f_{min})/2N$. Where N is the number of points and f_{max}-f_{min} is the VNA frequency span which is usually taken about 2 times broader than the full width at half maximum (FWHM) of the peak, to provide the confident measurements of Q-factor, that is $\sigma_f = f_0/QN$. And for the resonance at 2.45 GHz and N=1600 (number of points used in experiment) one has $\sigma_f = 1.53$ MHz/Q. For experimental 100<Q<11500 the error interval is $0.13 < \sigma_f < 15.3$ kHz. Accordingly for Q factor one has $\sigma_Q = 2Q/N = 1.25 \times 10^{-3} \times Q$, and $0.1 < \sigma_Q < 15$. However, due to deviations in the cavity conductivity and size due to natural temperature fluctuations in the lab as well as due to deviations in size and position of the sample in the cavity the experimental errors in f_0 and Q may be several times higher. In Fig. 4.1.2 the sensitivity curves for a TE_{104} WR340 waveguide cavity are presented in the parameter range $1.5<\varepsilon'<300$ and $10^{-4}<\tan\delta<3$. Errors in ε' become significant for $\varepsilon'>70$ and $\tan\delta>0.2$ (see Fig. 4.1.2) but errors in $\tan\delta$ (and in ε'') are maximal for low loss materials (alumina, PTFE) with $\tan\delta<0.001$ and for very high loss materials with $\tan\delta>1$ where the effect of field screening play the role (see Fig. 4.1.3).

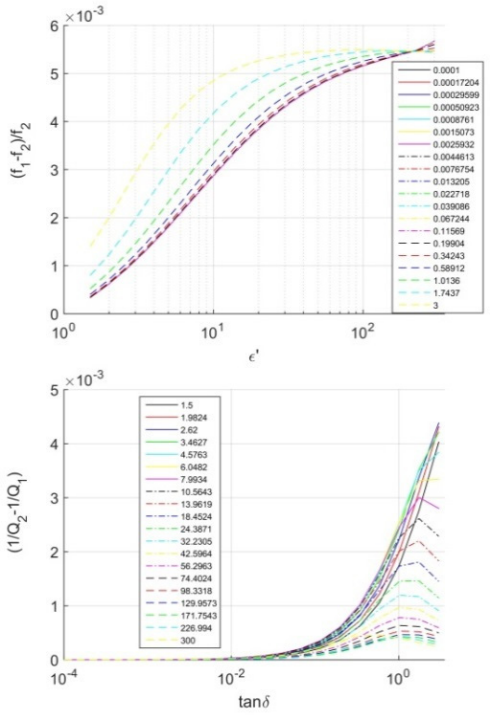

Fig. 4.1.2
Sensitivity curves for perturbation method. The relative frequency shift versus ε′ (top) and Q factor deviation versus tanδ (bottom) for different ε′ values.

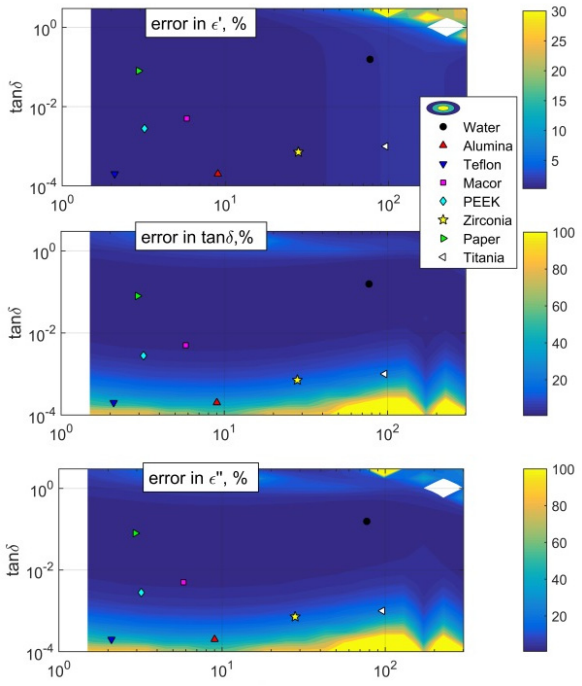

Fig. 4.1.3
Relative errors in dielectric constant, loss tangent and loss factor at minimal (instrumental) uncertainties in f0 and Q (15 kHz and 15).

4.2 Design Studies for filter structures

The Hephaistos oven used for continuous processes has two rectangular entry and exit tunnels of dimensions 83 cm in width and 30 to 40 cm in height (see Fig. 4.1.2 left). Currently, microwave leakage in the environment during system operation is mitigated with metallic wires fixed both at the entry and exit of the rectangular channels. The use of a microwave filter could decrease the microwave leakage and improve the overall efficiency of the oven by reflecting back the microwave energy into the hexagonal cavity. An important design challenge of the filter is the number of modes that are able to propagate due to the large dimensions of the tunnels. The possible propagating modes were calculated for an empty rectangular wave guide. Depending on the permittivity and geometry of the load, the filter behavior will change drastically. Nevertheless, a significant part of the microwave radiation will still be absorbed by the moving load, and so it is reasonable to assume that the filter still decreases the radiation leakage. As a starting point, a corrugated structure with half wave length periodicity was investigated.

The first possible propagating TE and TM mode were calculated for a rectangular wave guide of dimensions 83 cm in width and 10 cm in height with an operating frequency of 2.45 GHz.

The propagating modes are the ones with a cutoff frequency below 2.45 GHz for this specific geometry. The possible transverse electric modes are TE_{i0} for i=1 to 13, and TE_{i1} for i = 0 to 10 , which are 24 TE modes. For the transverse magnetic mode, only TM_{i1} for i = 1 to 10 can exist. The corresponding half

wavelength in propagation direction for each mode could be obtained by calculating the propagation constant of each mode.

Because of the limited length of the channel (78cm), only few spatial periods could be chosen. A proposed design used for the simulation is shown in Fig. 4.2.1. Ideally, more spatial periods should be added to increase the performance of the filter.

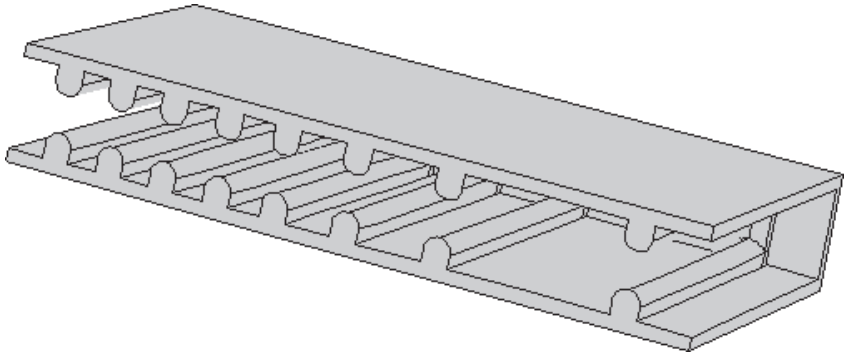

Fig. 4.2.1
Filter geometry, the depth of each slit is 30 mm the radius is 15 mm.

The ratio of the reflected power over the incident power (S_{11}) is shown in Fig. 4.2.2. Almost all the modes can be strongly attenuated. It is planned to build this filter and make some electric field measurement for different configurations. The figures presented here are the first results and this work is still an ongoing project.

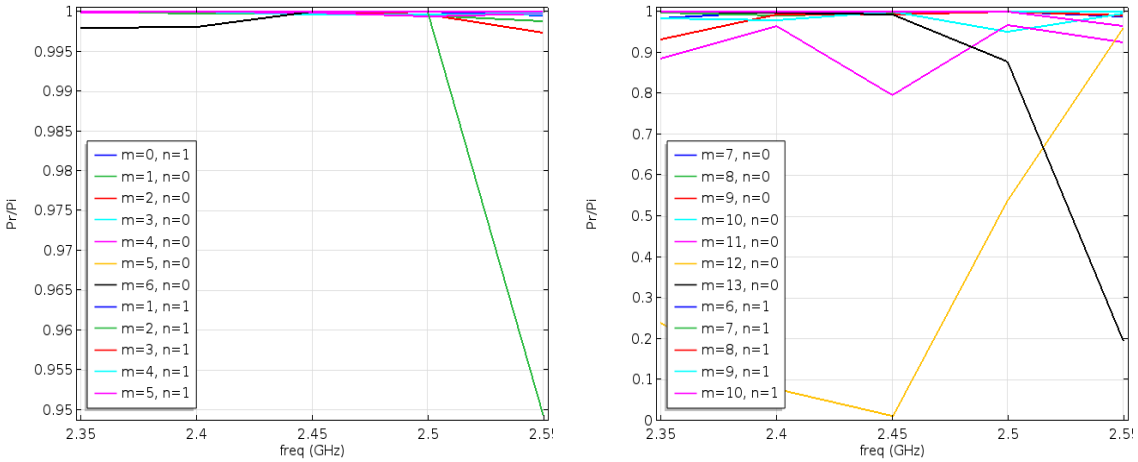

Fig. 4.2.2
Estimated S_{11} for the TE_{mn} modes for a channel height of 4cm, almost all the modes are filtered.

4.3 Collaboration Projects

4.3.1 FLAME

The FLAME project investigated the application of microwave heating for curing carbon fiber reinforced composites. Microwaves are able to penetrate into the material hence the resin is directly heated from inside the volume. The advantages are, that compared to conventional heating, microwaves need not to rely on slow heat conduction which opens the potential to accelerate the process and also to save energy, as only the material itself is heated and not the whole oven. The patented HEPHAISTOS technology, which is licensed to Vötsch Industrietechnik GmbH has been further enhanced with respect to curing of filament winding forms and continuous-flow operation. The new Hybrid HEPHAISTOS system, which combines microwave with convection heating, was prepared for operation at the KIT, cf. Fig. 4.3.1.

Fig. 4.3.1
Hybrid HEPHAISTOS system. Top: with conveyor belt for continuous-flow operation.

Besides this, the small portable HEPHAISTOS CA1 also received a retrofit. It got the new antennas which already proved in the new CA3 system but with an integrated launcher and without isolators due to constraints in space. The CA3 was enhanced with a dedicated microcontroller driven electronic that finally allows the low-ripple power supplies to be run in PWM mode reliably an frees the PC based LabVIEW software from this real-time critical task.

Producing filament winding forms with HEPHAISTOS

The fabrication of high-precision filament winding parts (see Fig. 4.3.2) for flywheel applications requires a precise process control with homogeneous temperature distribution and continuous rotation of the part around its axis during the curing for levelling out the gravity's influence on the resin distribution. For this purpose a dedicated rotational lead-through has been developed for HEPHAISTOS. It is mounted at one of the ovens door and allows placing the motor for driving the axis outside, cf. Fig. 4.3.2. This lead-through is equipped with a special choke for avoiding microwave leakage through the bearing. A patent application was submitted.

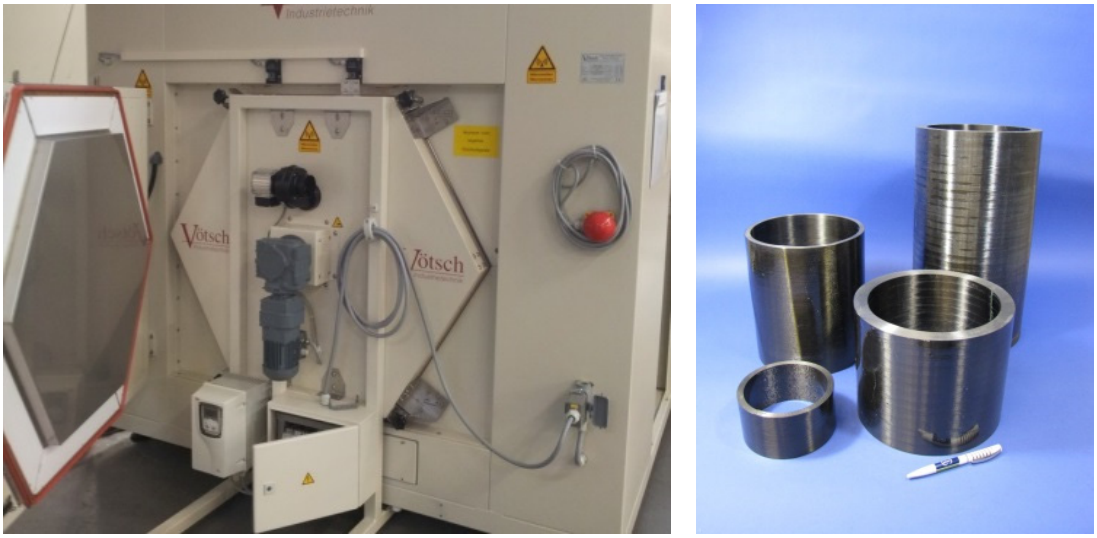

Fig. 4.3.2
HEPHAISTOS with front door replaced by rotational feed-through.

Further development and test of the multiple-input multiple-output (MIMO) control system of HEPHAISTOS. Besides the model predictive control (MPC) method, two additional adaptive and intelligent MIMO control methods have been developed and implemented in HEPHAISTOS ovens, which are the neural network control (NNC) and reinforcement learning control (RLC) methods. NNC is able to automatically estimate and control the multi-source microwave heating process, without the prior modeling procedure. RLC can directly control based on the thermal pictures, instead of separately measured temperature values, which guarantees that no hot spots and cold spots will occur on the heated object. These two MIMO control methods (NNC, RLC) have been verified in practical experiments and the corresponding results comparison with respect to the conventional proportional-integral-differential (PID) control is shown in the following (Fig 4.3.3 and 4.3.4). This comparison proves that the temperature homogeneity of the heated object can be significantly improved using our adaptive and intelligent power control system.

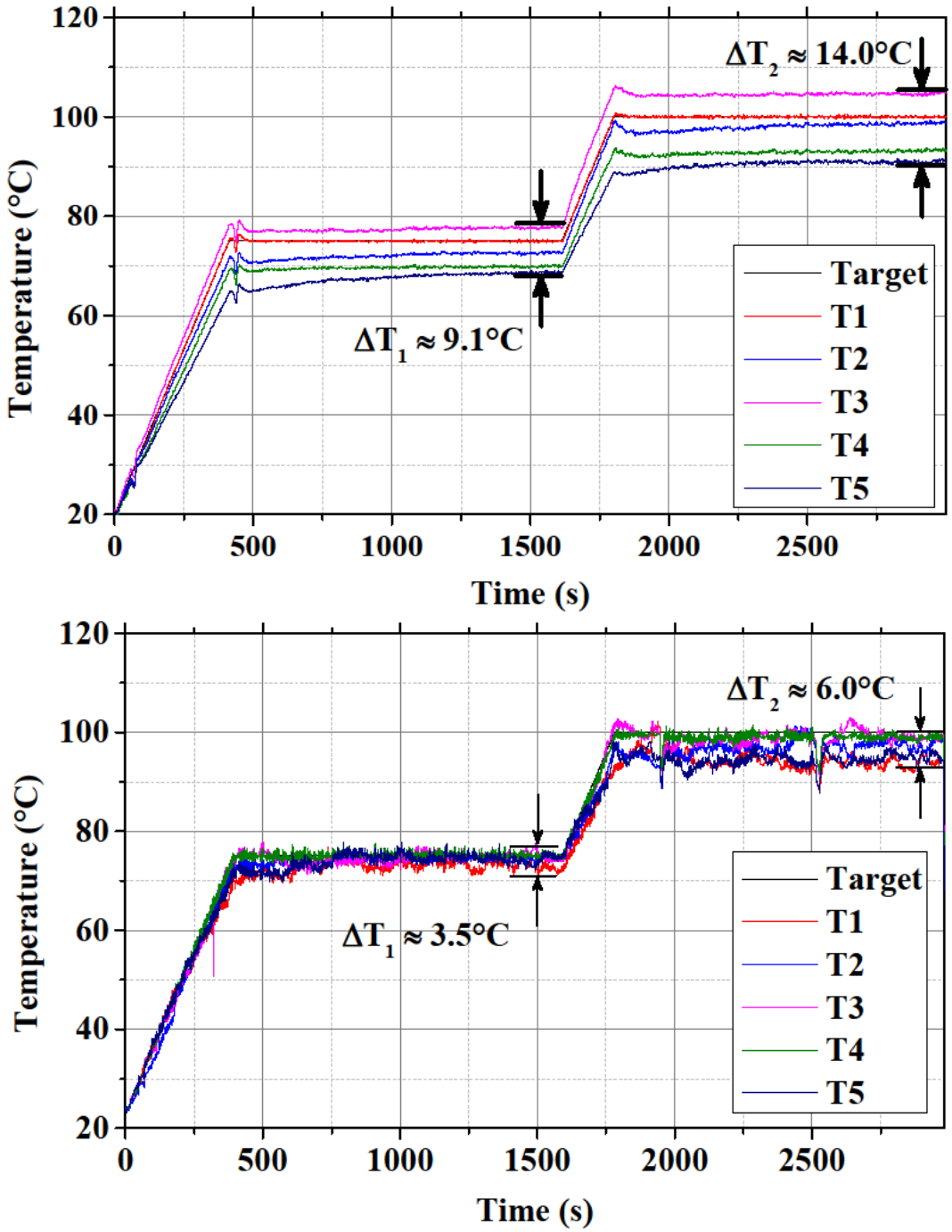

Fig. 4.3.3
Performance comparison between the conventional PID controller (top) and our innovative NNC controllers (bottom).

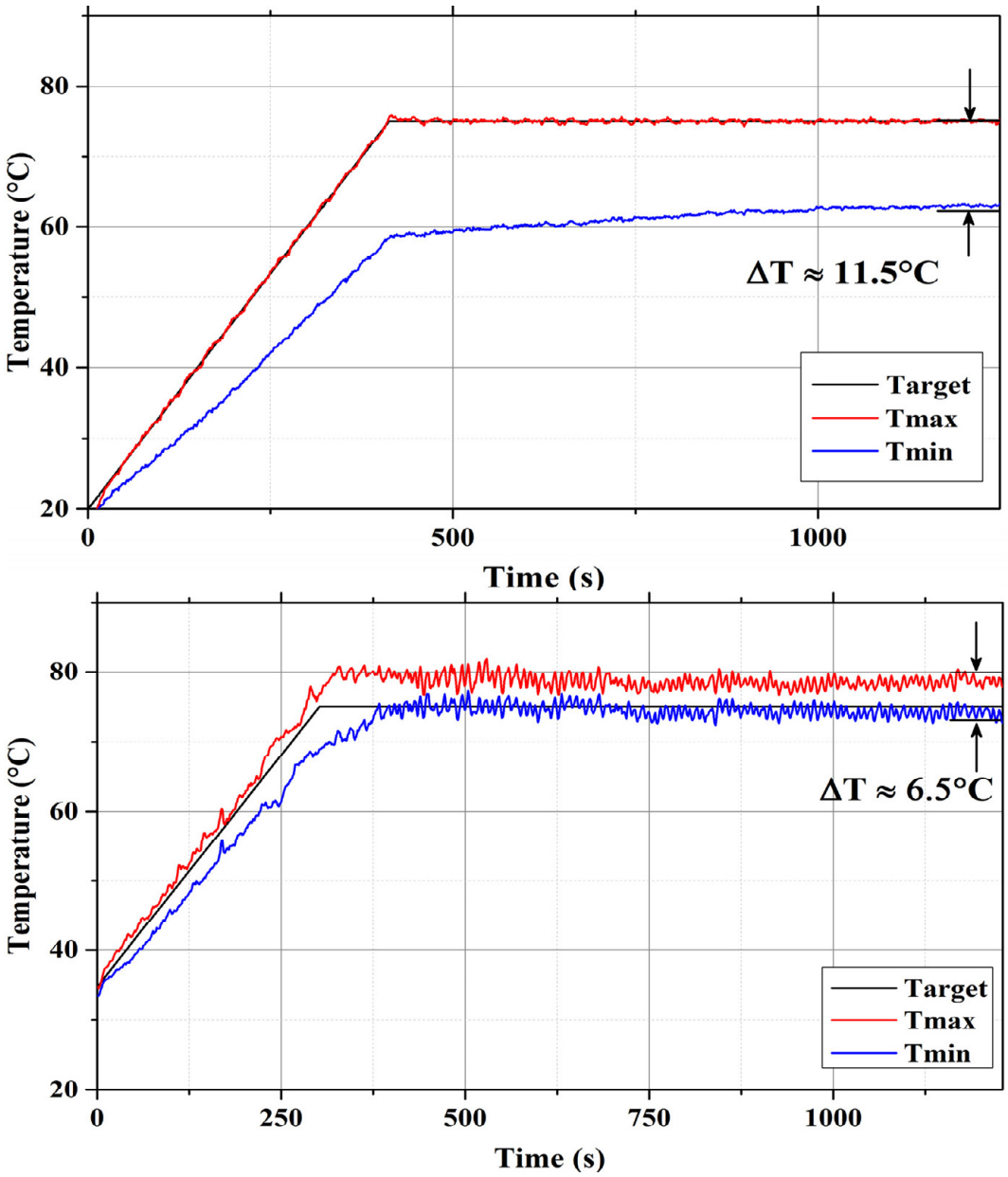

Fig. 4.3.4
Performance comparison between the conventional PID controller (top) and our innovative RLC (bottom) regarding the maximum and the minimum temperatures of the entire temperature distribution.

The LabVIEW control environment of HEPHAISTOS has been fully upgraded and modified, in order to fulfill the requirements from the hardware upgrade, regarding the power supplies, fieldbus protocols and control strategies.

All this efforts in control optimization culminated in a successfully Ph.D. dissertation entitled “Adaptive and Intelligent Temperature Control of Microwave Heating Systems with Multiple Sources”.

Microwave assisted pultrusion

Another promising field of microwave application is the pultrusion. This is a process for producing semi-finished elongated parts with constant profile cross section. For this, resin-impregnated fiber strands or fabrics are pulled through a shaping die. To cure the resin heat needs to be applied. In the conventional case simply the die is heated and the heat propagates into the material by heat conduction. By using microwave this process can be accelerated, as the microwaves penetrate into the material and heat it directly from inside. The difficulty here is that the die has to be made from a microwave transparent material while providing strong mechanical capabilities like ceramics.

A proper applicator was designed and built together with the company Maus. The first series of experiments focused on producing a simple circular rod with a diameter of 9 mm. For the shaping die a simple alumina ceramic tube was used. The inner surface of the tube, i.e. the interface between the ceramic and the fiber strands, has to be as smooth as technically possible to avoid sticking of resin or damage to the fibers. After several iterations of optimization and lots of experiments at ITV Denkendorf, up to 50 m at a stretch were pulled successfully in a good quality with a speed of 25 cm/min.

In the next step a much more sophisticated applicator with a U-profile as cross section was realized. This involved a much more complicated and very precise ceramic tool for the die that consisted of two separate parts that had to exactly fit together. Otherwise a gap could have occurred that caused unwanted accumulations of resin. With this tool a few meters were pulled successfully until the ceramic cracked. For stable operation further system and process optimization will be required. Fig. 4.3.5 show samples of the pultruded rod and U-profile.

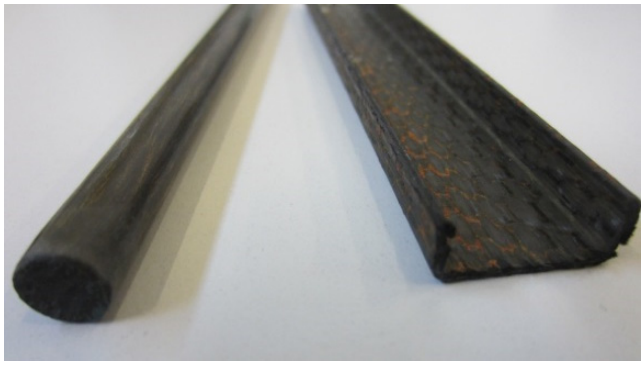

Fig. 4.3.5
FRP profiles successfully produced by microwave assisted pultrusion.

4.3.2 Multiphysics investigations on microwave assisted selective bonding

Multiphysics simulations of the process of microwave assisted bonding of synthetic leather to a plastic substrate were performed in the frame of the ZIM project “Development of selective microwave assisted gluing of textile leather to plastic base plates” („Entwicklung eines thermisch-selektiven Verklebens von textile Stoffen mit Formkörper mittels Mikrowellentechnik“). The simulations are performed for a HEPHAISTOS (VHM 100/100) microwave oven. The modelling of microwave assisted bonding is subdivided in two steps: i) solution of the electromagnetic problem for the HEPHAISTOS oven geometry with CST Microwave Studio® (see Fig. 4.3.6), ii) solution of the heat transfer problem with COMSOL Multiphysics®. In our previous studies the dielectric properties of adherends and adhesive were already measured and used as input data for electromagnetic model (see Fig. 4.3.6).

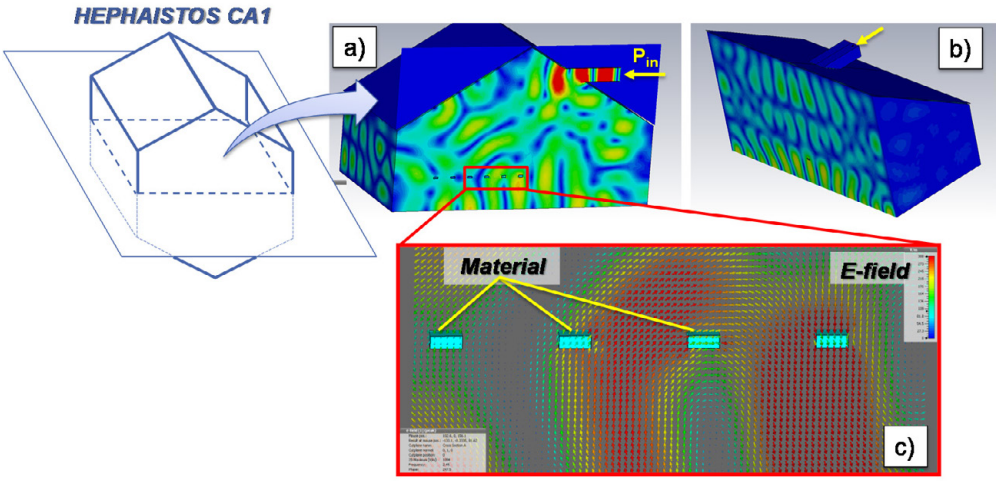

Fig. 4.3.6
Electromagnetic simulations for HEPHAISTOS CA1 oven. (a)-(b) Electric field pattern in the upper half of oven shown in two cross-sections. (c) Field pattern near material samples.

The results of modelling of heat transfer in the substrate-glue-coating sandwich structure are shown in Fig. 4.3.6. The 2.5D axially symmetrical model was limited to a cylinder whose axis is perpendicular to the leather and substrate surfaces and a single glue domain is positioned in-between substrate and coating. For optimized absorbed microwave power density in the glue (Q_{Glue}=23 MW/m^3) and boundary condition at the leather surface (convection coefficient h=70 W/K/m2) the glue temperature reaches 120 °C and the leather surface temperature is ~85 °C after 14 sec of heating (see Fig. 4.3.7).

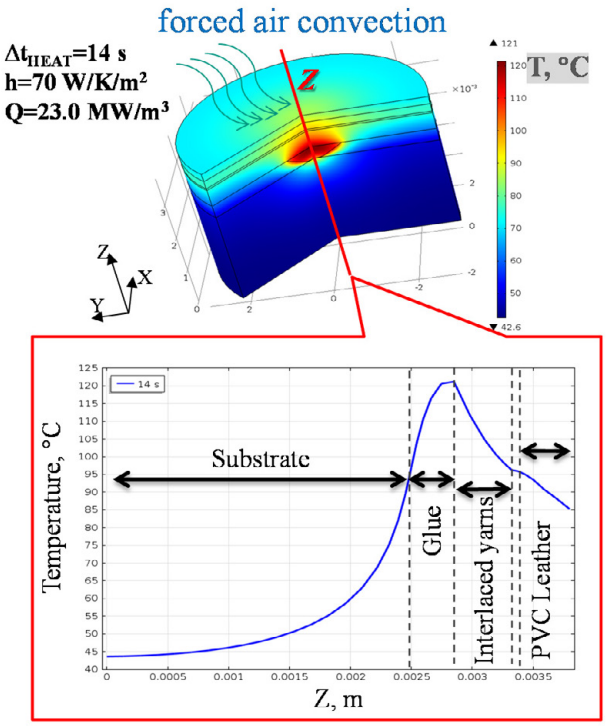

Fig. 4.3.7
Temperature distribution in the modeled substrate-glue-coating sandwich structure.

4.3.3 SYMBIOPTIMA

Within the H2020-SPIRE-2015 program the project SYMBIOPTIMA started in September 2015. The aim of this project is to improve European process industry efficiency by developing a cross-sectorial energy & resource management platform for intra- and inter-cluster streams in a symbiotic industrial cluster. In the frame of this project the disruptive increase of cross-sectorial re-use for particularly impacting waste streams is taken in to account, proposing an advanced WASTE2RESOURCE initiative for PET.

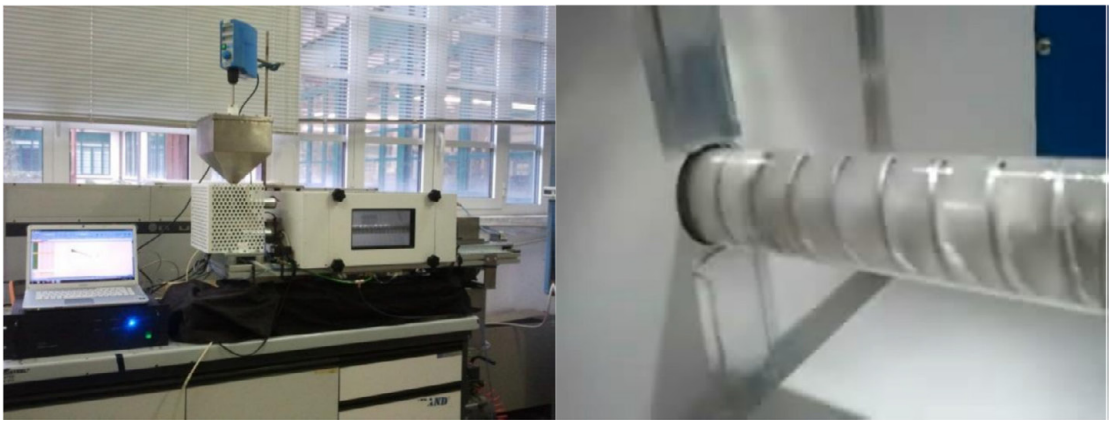

Fig. 4.3.8
Lab scale microwave applicator from grɛn.

The KIT task in this project is to support the development of an industrial scale microwave reactor for the recycling of PET plastic waste with a capacity of 16.5 kg/h. The recycling process consists in a depolymerisation of the PET molecules into monomers. This is done by the use of catalysts and microwave heating up to the process temperature in the range from 160 °C to 170 °C, what will require as pressure-resistant reactor for pressures up to 6 bar.

In the first step for detailed investigation of the de-polymerization process of PET a test set for dielectric characterization of pressurized chemical reactions has been designed. This system should enable the in-situ dielectric characterization of solvothermal chemical reactions for a broad range of dielectric properties ($10<\varepsilon'<30$, $0.2<\tan\delta<1{,}7$) and in the temperature range from 20 °C up to 200 °C, what will require a pressure resistance up to 20 bar. The results of the measurements will contribute to a well optimized design of an industrial- scale microwave applicator and may be helpful for the further improvement of the reaction parameters (temperature, pressure etc.).

4.3.4 Biomass to Fuel

In the context of biomass conversion to fuel, theoretical and practical feasibility studies performed for the application of microwave technology in this field. The motivation using microwave is a powerful volumetric heating source that results in evaporation of residual moisture content and increase of the permeability by developing high pressure water vapor within the biomass. The increase of permeability will allow improving subsequent thermochemical conversion processes. As a preliminary work, an applicator design was developed for lab scale experimental investigations and the dielectric characterization of wood with changing moisture content was done. Finally a Multiphysics model was developed that allows estimating the power requirements for a continuous processing of wood chips with a given mass flow, moisture content and target temperature. A porous model has also been developed with the COMSOL Multiphysics

software using an electro-thermal model including the phase change. This coupled model computes the power density, temperature and water content distribution during microwave heating for a fixed or moving biomass material configuration. The thermal properties are expressed both for a closed model (constant density) and open model where vapor leaves the system (variable density).

Tests have also been performed and first results have shown a significant increase of the wood permeability with a short time irradiation in a high power density microwave field. (See Fig. 4.3.9):

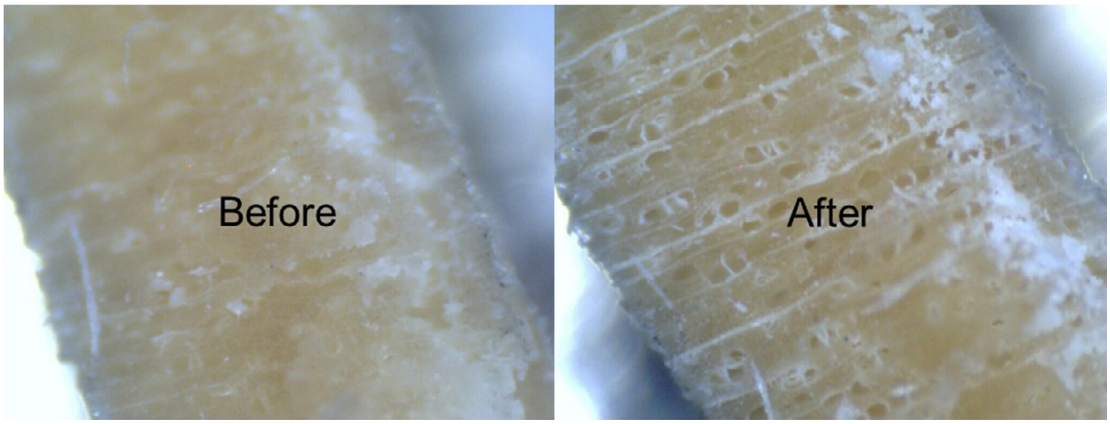

Fig. 4.3.9
Before and after microwave treatment, image comparison (500 W for about 1s)

Involved Staff:

K. Ayhan, Frau J. Dossinger, Prof. J. Jelonnek, Dr. T. Kayser, S. Layer, Dr. B. Lepers, Dr. G. Link, V. Nuss, D. Prastiyanto, V. Ramopoulos, T. Seitz, S. Soldatov, Y. Sun, Frau S. Wadle

HGF Program: FUSION

Journal Publications

F. Albajar, G. Aiello, S. Alberti, F. Arnold, K. Avramidis, M. Bader, R. Batista, R. Bertizzolo, T. Bonicelli, F. Braunmüller, C. Brescan, A. Bruschi, B. von Burg, K. Camino, G. Carannante, V. Casarin, A. Castillo, F. Cauvard, C. Cavalieri, M. Cavinato, R. Chavan, J. Chelis, F. Cismondi, D. Combescure, C. Darbos, D. Farina, D. Fasel, L. Figni, M. Gagliardi, F. Gandini, G. Gantenbein, T. Gassmann, R. Gessner, T.P. Goodman, V. Gracia, G. Grossetti, C. Heemskerk, M. Henderson, V. Hermann, J.P. Hogge, S. Illy, Z. Ioannidis, J. Jelonnek, J. Jin, W. Kasparek, J. Koning, A.S. Krause, J.D. Landis, G. Latsas, F. Li, F. Mazzocchi, A. Meier, A. Moro, R. Lousiainen, D. Purohit, S. Nowak, T. Omori, J. Van Oosterhout, J.Pacheco, I. Pagonakis, P. Platania, E. Poli, A.K. Preis, D. Ronden, Y. Rozier, T. Rzesnicki, G. Saibene, F. Sanchez, F. Sartori, O. Sauter, T. Scherer, C. Schlatter, S. Schreck, A. Serikov, U. Siravo, C. Sozzi, P. Spaeh, A. Spichiger, D. Strauss, K. Takahashi, M. Thumm, J. Tigelis, A. Vaccaro, J. Vomvoridis, M.Q. Tran, B. Weinhorst, (2015), Status of EU's contribution to the ITER EC system, *EPJ Web of Conferences*. (Online). 87, pp. 04004/1-6. Available: www.epj-conferences.org/articles/epjconf/abs/2015/06/epjconf_ec2015_04004/.

J. Jin, G. Gantenbein, J. Jelonnek, T. Rzesnicki, M. Thumm, (2015), Development of mode conversion waveguides at KIT, *EPJ Web of Conferences*. (Online). 87, pp. 04003/1-5. Available: www.epj-conferences.org/articles/epjconf/abs/2015/06/epjconf_ec2015_04004/.

J. Stober, F. Sommer, C. Angioni, A. Bock, E. Fable, F. Leuterer, F. Monaco, S. Müller, M. Müncih, B. Petzold, E. Poli, M. Schubert, H. Schütz, D. Wagner, H. Zohm, W. Kasparek, B. Plaum, A. Meier, Th. Scherer, D. Strauß, J. Jelonnek, M. Thumm, A. Litvak, G.G. Denisov, A.V. Chirkov, E.M. Tai, L.G. Popov, V.O. Nichiporenko, V.E. Myasnikov, E.A. Soluyanov, V. Malygin, (2015), High power ECRH and ECCD in moderately collisional ASDEX upgrade H-modes and status of EC system upgrade, *EPJ Web of Conferences*. (Online). 87, pp. 02004/1-6. Available: www.epj-conferences.org/articles/epjconf/abs/2015/06/epjconf_ec2015_04004/.

K.A. Avramidis, Z.C. Ioannidis, S. Kern, A. Samartsev, I.Gr. Pagonakis, I.G. Tigelis, J. Jelonnek, (2015), A comparative study on the modeling of dynamic after-cavity interaction in gyrotrons, *Physics of Plasmas*, Vol. 22, pp. 053106/1-12.

J. Franck, K. Avramidis, G. Gantenbein, S. Illy, J. Jin, M. Thumm, J. Jelonnek, (2015), A generic mode selection strategy for high-order mode gyrotrons operating at multiple frequencies, *Nuclear Fusion*, Vol. 55, pp. 013005/1-6.

I.G. Pagonakis, F. Albajar, S. Alberti, K. Avramidis, T. Bonicelli, F. Braunmueller, A. Bruschi, J. Chelis, F. Cismondi, G. Gantenbein, V. Hermann, K. Hesch, J.P. Hogge, J. Jelonnek, J. Jin, S. Illy, Z.C. Ioannidis, T. Kobarg, G.P. Latsas, F. Legrand, M. Lontano, B. Piosczyk, Y. Rozier, T. Rzesnicki, A. Samartsev, C. Schlatter, M. Thumm, I.G. Tigelis, M.Q. Tran, J. Weggen, J.L. Vomvoridis, (2015), Status of the development of the EU 170 GHz/1 MW/CW gyrotron, *Fusion Engineering and Design*, Vol. 96-97, pp. 149-154.

A. Samartsev, K.A. Avramidis, G. Gantenbein, G. Dammertz, M. Thumm, J. Jelonnek, (2015), Efficient frequency step-tunable megawatt-class D-band gyrotron, *IEEE Transactions on Electron Devices*, Vol. 62, pp. 2327-2332.

A. Schlaich, C. Wu, I. Pagonakis, K. Avramidis, S. Illy, G. Gantenbein, J. Jelonnek, M. Thumm, (2015), Frequency-based investigation of charge neutralization processes and thermal cavity expansion in gyrotrons, *Journal of Infrared Millimeter and Terahertz Waves*, Vol. 36, pp. 797-818.

A. Schlaich, G. Gantenbein, S. Illy, J. Jelonnek, M. Thumm, (2015), Observation of discrete hopping in MW-class gyrotrons during long-pulse operation, *IEEE Transactions on Electron Devices*, Vol. 62, pp. 3049-3055.

M. Schmid, J. Franck, P. Kalaria, K.A. Avramidis, G. Gantenbein, S. Illy, J. Jelonnek, I.G. Pagonakis, T. Rzesnicki, M. Thumm, (2015), Gyrotron development at KIT: FULGOR test facility and gyrotron concepts for DEMO, *Fusion Engineering and Design*, Vol. 96-97, pp. 589-592.

C. Wu, K.A. Avramidis, M. Thumm, J. Jelonnek, (2015), An improved broadband boundary condition for the RF field in gyroron interaction modeling, *IEEE Transactions on Microwave Theory and Techniques*, Vol. 63, pp. 2459-2467.

M. Thumm, J. Franck, P.C. Kalaria, K.A. Avramidis, G. Gantenbein, S. Illy, I.G. Pagonakis, M. Schmid, C. Wu, J. Zhang, J. Jelonnek, (2015), Towards a 0.24-THz, 1-to-2-MW-class gyrotron for DEMO, *The International Journal of Terahertz Science & Technology*, Vol. 8, pp. 85-100.

A.V. Arkhipov, N.V. Dvoretskaya, O.I. Louksha, G.G. Sominski, G.Gantenbein, A. Samartsev, (2015), Using scattered X-ray radiation for diagnostic of electron energy distribution in gyrotrons, Technical Physics Letters, Vol. 4a, pp. 60-64.

G. Arnoux, J. Coenen, B. Bazylev, Y. Corre, G.F. Matthews, I. Balboa, M. Clever, R. Dejarnac, S. Devaux, T. Eich, E. Gauthier, L. Frassinetti, J. Horacek, S. Jachmich, D. Kinna, S. Marsen, Ph. Mertens, R.A. Pitts, M. Rack, G. Sergienko, B. Sieglin, M. Stamp, V. Thompson, JET EFDA Contributors, (2015), Thermal analysis of an exposed tungsten edge in the JET divertor, Journal of Nuclear Materials, Vol. 463, pp. 415-419.

A.V. Arzhannikov, M.K.A. Thumm, A.V. Burdakov, V.S. Burmasov, N.S. Ginzburg, I.A. Ivanov, P.V. Kalinin, A.A. Kasatov, V.V. Kurkuchekov, S.A. Kuznetsov, M.A. Makarov, K.I. Mekler, N.Yu. Peskov, S.V. Polosatkin, S.S. Popov, V.V. Postupaev, A.F. Rovenskikh, A.S. Sergeev, S.I. Sinitsky, V.F. Sklyarov, V.D. Stephanov, L.N. Vyacheslovov, V.Yu. Zaslavsky, (2015), Two ways for high-power generation of subterahertz radiation by usage of strong relativistic electron beams, IEEE Transactions of Terahertz Science and Technology, Vol. 5, pp. 478-485.

I.G. Chelis, K.A. Avramidis, J.L. Vomvoridis, (2015), Resonant modes for disk-loaded cylindrical structures with open boundaries, IEEE Transactions on Microwave Theory and Techniques, Vol. 63, pp. 1781-1790.

J.W. Coenen, G. Arnoux, B. Bazylev, G.F. Matthews, A. Autricque, I. Balboa, M. Clever, R. Dejarnac, I. Coffey, Y. Corre, S. Devaux, L. Frassinetti, E. Gauthier, J. Horacek, S. Jachmich, M. Komm, M. Knaup, K. Krieger, S. Marsen, A. Meigs, Ph. Mertens, R.A. Pitts, T. Puetterich, M. Rack, M. Stamp, G. Sergienko, P. Tamain, V. Thompson, JET EFDA Contributors, (2015), ELM-induced transient tungston melting in the JET divertor, Nuclear Fusion, Vol. 55, pp. 02301/1-22.

J.W. Coenen, G. Arnoux, B. Bazylev, G.F. Matthews, S. Jachmich, I. Balboy, M. Clever, R. Dejarnac, I. Coffey, Y. Corre, S. Devaux, L. Frassinetti, E. Gauthir, J. Horacek, M. Knaup, M. Komm, K. Krieger, S. Marsen, G. Meigs, P. Tamain, V. Thompson, JET-EFDA Contributors, (2015), ELM induced tungsten melting and its impact on tokamak operation, Journal of Nuclear Materials, Vol. 463, pp. 78-84.

R.K. Dhakad, G.S. Baghel, M.V. Kartikeyan, M.K. Thumm, (2015), Output system for a 170-GHz/1.5-MW continuous wave gyrotron operatin in the TE28,12 mode, IEEE Transactions on Plasma Science, Vol. 43, pp. 391-397.

R. Fetzer, Y. Igitkhanov, B. Bazylev, (2015), Efficiency of water cooland for DEMO divertor, Fusion Engineering and Design, Vol. 98-99, pp. 1290-1293.

T. Franke, E. Barbato, G. Bosia, A. Cardinali, S. Ceccuzzi, R. Cesario, D. Van Eester, G. Federici, G. Gantenbein, W. Helou, J. Hillairet, I. Jenkins, Ye.O. Kazakov, R. Kemp, E. Lerche, F. Mirizzi, J.M. Noterdaeme, E. Poli, L. Porte, G.L. Ravera, E. Surrey, G. Tardini, M.Q. Trans, C. Tsironis, A.A. Tuccillo, R. Wenninger, H. Zohm, EFDA PPP&T Team, (2015), Technological and physics assessments on heating and current drive systems for DEMO, Fusion Engineering and Design, Vol. 96-97, pp. 468-472.

Y.J. Huang, K.R. Chu, M. Thumm, (2015), Self-consistent modeling of terahertz waveguide and covity with frequendy-dependent conductivity, Physics of Plasmas, Vol. 22, pp. 013108/1-10.

Yu. Igitkhanov, R. Fetzer, L. Boccaccini, B. Bazylev, (2015), Thermo-mechanical analysis of the DEMO FW module, Physica Scripta, Vol. 90, pp. 105601/1-4.

Z.C. Ioannidis, K.A. Avramidis, I.G. Tigelis, (2015), Open-ended coaxial cavities with corrugated inner and outer walls, Journal of Infrared Millimeter and Terahertz Waves, Vol. 36, pp. 461-473.

N.S. Klimov, A.B. Putrik, J. Linke, R.A. Pitts, A.M. Zhitlukhin, I.B. Kuprianov, A.V. Spitsyn, O.V. Ogorodnikova, V.L. Podkovyrov, A.D. Muzichenko, B.V. Ivanov, Ya.V. Sergeecheva, I.G. Lesina, D.V. Kovalenko, V.A. Barsuk, N.A. Danilina, B.N. Bazylev, R.N. Giniyatulin, (2015), Plasma facing materials performance under ITER-relevant mitigated disruptions photonic heat loads, Journal of Nuclear Materialos, Vol. 463, pp. 61-65.

V.A. Makhlaj, I.E. Garkusha, N.N. Aksenov, B. Bazylev, O.V. Byrka, V.V. Chebotarev, I. Landman, S.S. Herashchenko, V.V. Staltsov, (2015), Damage of target edges in brush-like geometry in the course of ELM-like plasma pulses in QSPA Kh-50, Journal of Nuclear Materials, Vol. 463, pp. 210-214.

S. Pestchanyi, R. Koslowski, C. Reux, M. Lehnen, JET EFDA Contributors, (2015), Simulation of MGI efficiency for plasma energy conversion into Ar radiation in JET and implications for ITER, Fusion Engineering and Design, Vol. 96-97, pp. 685-689.

S. Pestchanyi, B. Bazylev, I. Landman, (2015), Simulation of W diaphragm efficiency for mitigation of RE beam in ITER, Journal of Nuclear Materials, Vol. 463, pp. 170-173.

R.A. Pitts, B. Bazylev, J. Linke, I. Landman, M. Lehnen, D. Loesser, Th. Loewenhoff, M. Merola, R. Roccella, G. Saibene, M. Smith, V.S. Udintsev, (2015), Final case for a stainless steel diagnostic first wall on ITER, Journal of Nuclear Materials, Vol. 463, pp.748-752.

C. Reux, V. Plyusnin, B. Alper, D. Alves, B. Bazylev, E. Belonohy, S. Brezinsek, J. Decker, S. Devaux, P. De Vries, A. Fil, S. Gerasimov, I. Lupelli, S. Jachmich, E.M. Khilkevitch, V. Kiptily, R. Koslowski, U. Kruezi, M. Lehnen, A. Manzanares, J. Mlynar, E. Nardon, E. Nilsson, V. Riccardo, F. Saint-Laurent, E.E. Shevelev, C. Sozzi, JET EFDA Contributors, (2015), Runaway beam studies during disruptions at JET-ILW, Journal of Nuclear Materials, Vol. 643, pp.143-149.

C. Reux, V. Plyusnin, B. Alper, D. Alves, B. Bazylev, E. Belonohy, A. Boboc, S. Brezinsek, I. Coffey, J. Decker, P. Drewelow, S. Devaux, P.C. De Vries, A. Fil, S. Gerasimov, L. Giacomelli, S. Jachmich, E.M. Khilkevitch, V. Kiptily, R. Koslowski, U. Kruezi, M. Lehnen, I. Lupelli, P.J. Lomas, A. Manzanares, A. Martin de Aguilera, G.F. Matthews, H. Mlynaem, E. Nardon, E. Nilsson, C. Perez von Thun, V. Riccardo, F. Saint-Lautent, A.E. Shevelev, G. Sips, C. Sozzi, JET Contributors, (2015), Runaway electron beam generation and mitigation during disruptions at JET-ILW, Nuclear Fusion, Vol. 55, pp. 093013/1-17.

A. Roy Choudhury, S. Kern, M. Thumm, (2015), Study of dynamic after cavity interaction in gyrotrons. Part I: Adiabatic approximation, IEEE Transactions on Electron Devices, Vol. 62, pp. 184-191.

A. Roy Choudhury, A. D'Andrea, M. Thumm, (2015), Study of dynamic after cavity interaction in gyrotrons. Part II: Influence of a nonuniform magnetic field, IEEE Transactions on Electron Devices, Vol. 62, pp.192-199.

L. Savoldi, C. Bertani, G. Cau, F. Cismondi, G. Gantenbein, S. Illy, G. Monni, R. Zanino, (2015), Numerical investigation of collector cooling for a 1 MW ITER gyrotron operated with vertical sweeping, Fusion Engineering and Design, Vol.100, pp. 112-119.

L. Savoldi, C. Bertani, G. Cau, F. Cismondi, G. Gantenbein, S. Illy, G. Monni, Y. Rozier, R. Zanino, (2015), Towards the optimization of the thermal-hydraulic performance of gyrotron collectors, Fusion Engineering and Design, Vol.100, pp. 120-132.

D. Wagner, W. Bongers, W. Kaparek, F. Leuterer, F. Monaco, M. Münich, H. Schütz, J. Stober, M. Thumm, H. Van den Brand, (2015), A multifrequency notch filter for millimeter wave plasma diagnostic based on photonoc bandgaps on corrugated circular waveguide, *EPJ Web of Conferences*. (Online). 87, pp. 04012/1-4. Available: www.epj-conferences.org/articles/epjconf/abs/2015/06/epjconf_ec2015_04004/.

J. Zhang; S. Illy, I. Gr Pagonakis, K.A. Avramidis, M. Thumm, J. Jelonnek, (2015), Influence of emitter surface roughness on high power fusion gyrotron operation, Nuclear Fusion, Vol. 56 (2), pp. 026002/1-7.

Scientific Reports

J. Jelonnek, (Hrsg.) Annual Report 2014 / Institute for Pulsed Power and Microwave Technology = Jahresbericht 2014 / Institut für Hochleistungsimpuls- und Mikrowellentechnik. (KIT Scientific Reports; 7707), 2015, KIT Scientific Publishing, Karlsruhe.

M. Thumm, State-of-the-Art of High Power Gyro-Devices and Free Electron Masers. Update 2014. (KIT Scientific Reports; 7693), 2015, KIT Scientific Publishing, Karlsruhe.

HGF Program: EE

Journal Publications

T. Kotnik, W. Frey, M. Sack, S. Haberl Meglic, M. Peterka, D. Miklavcic, (2015), Electroporation-based applications in biotechnology, Trends in Biotechnology, Vol. 33 (8), pp. 480-488.

A. Silve, I. Leray, M. Leguebe, C. Poignard, L.M. Mir, (2015), Cell membrane permeabilization by 12-ns electric pulses: Not a purely dielectric, but a charge-dependent phenomenon. Bioelectrochemistry, Vol. 106, pp. 369-378.

L.H. Wegner, (2015), A thermodynamic analysis of the feasibility of water secretion into xylem vessels against a water potential gradient, Functional Plant Biology, Vol. 42, 828-835.

L.H. Wegner, W. Frey, A. Silve (2015), Electroporation of DC-3F cells in a dual process, Biophysical Journal, Vol. 108, pp. 1660-1671.

A. Silve, S. Rocke, W. Frey, (2015), Image processing for non-ratiometric measurement of membrane voltage using fluorescent reporters and pulsed laser illumination, Bioelectrochemistry, Vol. 103, pp. 39-43, 2015.

L.H. Wegner, (2015), The conductance of celluar membranes at supra-physiological voltages, Bioelectrochemistry, Vol. 103, pp. 34-38, 2015.

Chapters in Books

L.H. Wegner, Interplay of water and nutrient transport: A whole-plant perspective, Lüttge, U. [Hrsg.] Progress in Botany : Vol.76 Cham : Springer, 2015, pp. 109-141.

G. Müller, G. Schumacher, A. Heinzel, A. Jianu, A. Weisenburger, Corrosion protection in lead and lead-bismuth eutectic at elevated temperatures, Handbook on Lead-bismuth Eutectic Alloy and Lead Properties, Materials Compatibility, Thermal-hydraulics and Technologies 2015 Edition Issy-les-Moulineaux : OECD Nuclear Energy Agency, 2015, 617-646.

F.J. Martin-Munoz, A. Heinzel, A. Weisenburger, G. Müller, S. Gavrilov, K. Lambrinou, Compatibility of structural materials with lead-bismuth eutectic and lead: Standardisation of data, corrosion mechanism and rate Handbook on Lead-bismuth Eutectic Alloy and Lead Properties, Materials Compatibility, Thermal-hydraulics and Technologies 2015 Edition Issy-les-Moulineaux : OECD Nuclear Energy Agency, 2015, pp. 431-486.

HGF Program: NUSAFE

Journal Publications

T. Geißler, M. Plevan, A. Abanades, A. Heinzel, K. Mehravaran, R.K. Rathnam, C. Rubbia, D. Salmieri, L. Stoppel, S. Stückrad, A. Weisenburger, H. Wenninger, T. Wetzel, (2015), Experimental investigation and thermo-chemical modeling of methane pyrolysis in a liquid metal bubble column reactor with a packed bed, Int. Journal of Hydrogen Energy, Vol. 40, pp. 14134-14146.

HGF Program: EMR

Journal Publications

B. Lepers, T. Seitz, G. Link, J. Jelonnek, M. Zink, (2015), Development of a 10 KW microwave applicator for thermal cracking of lignite briquettes, Frontiers in Heat and Mass Transfer, Vol. 6 (20), pp.1-6.

S. Takayama, G. Link, M. Sato, J. Jelonnek, (2015), Possibility for iron production using high-power millimeter waves, *IEEE Transactions on Plasma Science*, Vol. 43, pp. 3517-3521.

A. Krämer-Flecken, S. Soldatov, Y. Xu, H. Arnichand, S. Hacquin, R. Sabot, TEXTOR Team, (2015), Long-range correlation properties of quasi-coherent modes at TEXTOR. New Journal of Physics, Vol. 17, pp. 073007/1-17.

M.M. Mahmoud, M. Thumm, Crystallization of lithium disilicate glass using high frequency microwave processing, Journal of the European Ceramic Society, Vol. pp. 2915-2922, 2015.

M.M. Mahmoud, G. Link, M. Thumm, The role of the native oxide shell on the microwave sintering of copper metal powder compacts, Journal of Alloys and Compounds, Vol. 627, pp. 231-237, 2015.

Scientific Reports

G. Link, T. Kayser, F. Köster, R. Weiß, S. Betz, R. Wiesehöfer, T. Sames, N. Boulkertous, D. Teufl, S. Zaremba, F. Heidbrink, M. Maus, R. Ghomeshi, S. Küppers, M. Milwich, Faserverbund-Leichtbau mit automatisierter Mikrowellenprozesstechnik hoher Energieeffizienz (FLAME): Schlussbericht des BMBF-Verbundprojektes, KIT Scientific Report 7701, 2015.

Appendix

Equipment, Teaching Activities and Staff

IHM is equipped with a workstation cluster and a large number of experimental installations: KEA, KEA-ZAR, three GESA machines, eight COSTA devices, one abrasion and one erosion teststand, two gyrotron test facilities with one common power supply and microwave-tight measurement chamber, one compact technology gyrotron (30 GHz, 15 kW, continuous wave (CW)), several 2.45 GHz applicators of the HEPHAISTOS series, one 0,915 GHz, 60 kW magnetron system, one 5.8 GHz, 3 kW klystron installation and a low power microwave laboratory with several vectorial network analysers.

The project FULGOR, targeting for a renewal of the KIT gyrotron teststand is progressing. In 2013, an agreement on the project structure including the involvement of the KIT project and quality management has been achieved. The final start of the procurement of the equipment was in 2014.

Prof. John Jelonnek has continued to teach the lecture course entitled “High Power Microwave Technologies (Hochleistungsmikrowellentechnik)” for Master students at KIT. Prof. Georg Müller has continued to teach the lecture on “Pulsed Power Technologies and Applications” at KIT. Dr. Gerd Gantenbein has been teaching the part “heating and current drive” of the lecture “Fusionstechnologie B” by Prof. R. Stieglitz, IFRT. Dr.-Ing. Martin Sack hold the lecture course “Elektronische Systeme und EMV” at KIT.

At the turn of the year 2015/2016 the total staff with regular positions amounted to 37 (16 academic staff members, 12 engineers and 9 technical staff member and others).

In addition 13 academic staff members and 3 technical staff members (and others) were financed by acquired third party budget.

In course of 2015, 2 guest scientists, 10 PhD students (1 of KIT-Campus South, 4 of KIT-Campus North, 4 Scholarship, 1 in cooperation with IPP Greifswald), 4 DHBW student, 1 trainee in physics laboratory and 4 trainees in the mechanical and electronics workshops worked in the IHM. 4 Master students have been hosted at IHM (3 of ETIT faculty, 1 of University of Bordeaux, France) and 5 Bachelor student has been at IHM during 2015.

Strategical Events, Scientific Honors and Awards

Dr. Aude Silve received the "1st World Congress on Electroporation and Pulsed Electric Fields in Biology, Medicine and Food and Environmental Technologies, Portoroz, SLO, September 6-10, 2015".

Michael Betz received a prize of ITG 2015 for the dissertation.

Prof. Georg Müller was assigned as a Member of Editorial Board of the new journal ´Matter and Radiation at Extreme´ (MRE).

Longlasting Co-operations with Industries, Universities and Research Institutes

- Basics of the interaction between electrical fields and cells (Bioelectrics) in the frame of the International Bioelectrics Consortium with Old Dominion University Norfolk, USA; Kumamoto University, Japan; University of Missouri Columbia, USA; Institute Gustave-Roussy and University of Paris XI, Villejuif, France; University of Toulouse, Toulouse, France, Leibniz Institute for Plasma Science and Technology, Greifswald, Germany.

- Desinfection of hospital wastewater by pulsed electric field treatment in cooperation with University of Mainz and Eisenmann AG.

- Integration of the electroporation process for sugar production with SÜDZUCKER AG.

- Development of protection against corrosion in liquid metal cooled reactor systems in the following EU-Projectes: LEADER, GETMAT, MATTER, SEARCH (Partner: CEA, ENEA, SCK-CEN, CIEMAT).

- Development of large area pulsed electron beam devices in collaboration with the Efremov Institute, St. Petersburg, Russia.

- Experiments on liquid Pb and PbBi-cooling of reactor systems with the Institute for Physics and Power Engineering (IPPE), Obninsk, Russia.

- Development, installation and test of the complete 10 MW, 140 GHz ECRH Systems for continuous wave operation at the stellarator Wendelstein W7-X in collaboration with the Max-Planck-Institute for Plasmaphysics (IPP) Greifswald and the Institute of Interfacial Process Engineering and Plasma Technology (Institut für Grenzflächenverfahrenstechnik und Plasmatechnologie, IGVP) of the University of Stuttgart.

- Development of the European ITER Gyrotrons in the frame of the European GYrotron Consortium (EGYC) and coordinated by Fusion for Energy (F4E). The other members of the Consortium are CRPP, EPFL Lausanne, Switzerland, CNR Milano, Italy, ENEA, Frascati, Italy, HELLAS-Assoc. EURATOM (NTUA/NKUA Athens), Greece. The industrial partner is the microwave tube company Thales Electron Devices (TED) in Paris, France.

- Development of new diagnostic systems for improvement of electron guns for gyrotrons and cavity interaction calculations in collaboration with the St. Petersburg Polytechical University, Russia and the University of Latvia, Latvia.

- Basic investigations of plasma-wall interaction in fusion reactors in collaboration with the State Research Center of Russian Federation Troitsk Institute for Innovation and Fusion Research (TRINITI), Troitsk, Russia and the Institute of Plasma Physics, Kharkov, Ukraine.

- Development of Microwave Systems of the HEPHAISTOS Series for materials processing with microwaves with the Company Vötsch Industrietechnik GmbH, Reiskirchen.

The Institute for Pulsed Power and Microwave Technology (Institut für Hochleistungsimpuls- und Mikrowellentechnik (IHM)) is doing research in the areas of pulsed power and high power microwave technologies. Both, research and development of high power sources as well as related applications are in the focus. Applications for pulsed power technologies are ranging from material processing to bioelectrics. High power microwave technologies are focusing on RF sources (gyrotrons) for electron cyclotron resonance heating of magnetically confined plasmas and on applications for material processing at microwave frequencies.

The IHM is doing research, development, academic education, and, in collaboration with the KIT Division IMA and industrial partners, the technology transfer. The IHM is focusing on the long term research goals of the German Helmholtz Association (HGF). During POF3, the ongoing program oriented research period of HGF (2015 – 2020), research projects are running within following four HGF programs: “Energy Efficiency, Materials and Resources (EMR)”; “Nuclear Fusion (FUSION)”, “Nuclear Waste Management, Safety and Radiation Research (NUSAFE)” and “Renewable Energies (EE)”.

During 2015, R&D work has been done in the following areas: fundamental theoretical and experimental research on the generation of intense electron beams, strong electromagnetic fields and their interaction with biomass, materials and plasmas; application of those methods in the areas of energy production through controlled thermonuclear fusion in magnetically confined plasmas, in material processing and in energy technology.

ISSN 1869-9669